SYNTHESIS ZNO TRANSPARENT CONDUCTIVE OXIDE BY ELECTROSPRAY DEPOSITION

BY

SUREEPORN (POLLAOR) CHOTHIRAWAT

A THESIS
SUBMITTED TO THE FACULTY OF

ALFRED UNIVERSITY

IN PARTIAL FULFILLMENT OF THE REQUIREMENTS
FOR THE DEGREE OF

MASTER OF SCIENCE

IN

CERAMIC ENGINEERING

ALFRED, NEW YORK

JUNE, 2015

SYNTHESIS ZNO TRANSPARENT CONDUCTIVE OXIDE
BY ELECTROSPRAY DEPOSITION

BY

SUREEPORN (POLLAOR) CHOTHIRAWAT

B.S. CHULALONGKORN UNIVERSITY (2004)

SIGNATURE OF AUTHOR_____

APPROVED BY_____

YIQUAN WU, ADVISOR

_____

S.K. SUNDARAM, ADVISORY COMMITTEE

_____

NATHAN P. MELLOT, ADVISORY COMMITTEE

_____

DAWEI LIU, ADVISORY COMMITTEE

_____

CHAIR, ORAL THESIS DEFENSE

ACCEPTED BY _____

DOREEN D. EDWARDS, DEAN
KAZUO INAMORI SCHOOL OF ENGINEERING

ACKNOWLEDGMENTS

I would like to thank my advisor, Dr. Yiquan Wu, for supporting and encouraging me to become excellent and independent researcher. Moreover, he motivated and inspired me to love exploring tirelessly during my study at Alfred University. To Dr. Dawei Liu, Dr. Nathan P Mellot and Dr. S.K. Sundaram for being my thesis committee members and for being ready to support me any time. I greatly appreciated that Dr. Doreen Edwards for being supportive and for answering me all emails. To Dr. William M Carty for reminding me the struggle time in Alfred. To Dr. Scott Misture and Dr. Cormack who made complex concepts much easier and provided me a new perspective of learning. To Tom Steere who made my tough semester more relaxed and made less is more in reality. To Dr. Walter Schulze for being friendly and helping me to solve the problem with me very closely. Most importantly, I would like to express my appreciation to all technicians and specialists for being my mentors in every step of thesis progress. To Gerald L Wynick who made me not afraid to smile in difficult time. To Mr. Swavek Zdzieszynski who never waited to solve my silly problems. To Thiebaud James who never smiled to my face but I knew you always do behind me. To Fran who kept acknowledging me all stuff without any complaint. I also would like to thank my lab partners, Yin Liu who made me alert and was willing to help me any time, Yiyu Li for academic stuff and XRD and Yan Yang who nurtured me and talk girl's stuff with me freely. To Dimple Prahan and Alice Li for being optimistic in many issues during the tough time as well as David Tseng for your unconditional assistance. Thank to Victor Colorado, Ruifeng Ouayang and Chokchai Yatongchai for giving me friendship. To Wirat Lerdprom for helping in any circumstance and making me felt at home when living in Alfred.

To Mr. Apirak and my steve Jobs-Aphiwat Chothirawat to encourage me to move forward without any concern while studying abroad. To Ms. Juntanal Limranangkul, Mr. Chalermchai Chirasakayakul and SCG ceramic-cement for being support and keeping encouraged me for further studies. Last but not least, to my dad and mom-Mr. Sommai Pollaor and Ms. Apai Chaiwinyos for educational support and inspiration. As well as Mr. Anusorn and Ms. Supharat Pollaor to make me realize how important of brotherhood and sisterhood are.

TABLE OF CONTENTS

Page

LIST OF TABLES

Page

LIST OF FIGURES

Page

ABSTRACT

The objective of this thesis was to synthesize ZnO-based transparent oxide (TCO) thin film by using an economically-versatile fabrication technique called electrospray deposition (ESD). A co-doping approach was employed to enhance optoelectronic properties of undoped ZnO, which is a non-toxic and abundant material for flat display panels and energy-harvesting applications.

Firstly, ESD process parameters were investigated in order to optimize the quality of thin film, namely, deionized water content in precursor, applied voltage, deposition temperature, flow rate, deposit distance, and deposit time. Regression plots revealed the tendency of individual process parameter towards % film coverage area. In addition, the factorial design of the experiment was performed to determine significant process parameters (P-value < 0.05), which showed a strong influence to film quality at R^2 of 87.61%.

Secondly, 0-3%wt of Aluminum (Al) concentration were co-doped with 3%wt of Lithium (Li). The aim was to synthesize p-type ZnO-based TCO by a co-doping approach. Li (acceptor) and Al (donor) at different ratios of acceptor-to-donor (A/D) were investigated effects on defect diffusion mechanism, film's crystallinity, microstructure, and topography by X-ray diffraction (XRD), Scanning Electron Microscopy (SEM) and Atomic Force Microscopy (AFM). Hall effect measurement and UV-Visible spectrometer studies were carried out to evaluate optoelectronic properties of as-annealed film. The lowest resistivity of 2.51×10^{-3} Ohm·cm of p-type ZnO-based TCO was obtained without optical properties degradation by employing A/D of 2:1 due to the scattering effect of ionized defect and was minimized by A-D-A defect cluster.

Lastly, 3%wt of gallium (donor) and 3%wt of lithium (acceptor) were co-doped with 0-3%wt of Aluminum concentration in order to compare effects of co-dopant types on defect diffusion mechanism. A small variation of lattice distortion as %Al increased, which suggested that dopant solubility was improved by substitutional mechanism. As a result, the film's crystallinity and microstructure were improved due to the minimization of disturbing stress and enhanced diffusibility. Consequently, UV-Visible spectrometer and 4-point probe measurement showed that optoelectronic properties of the film improved in co-doped samples.

INTRODUCTION

"Logic brings you from A to B, but imagination takes you everywhere"
-Albert Einstein

The development of transparent conductive oxide (TCO) has been performed to serve the advancement in functional display panels and energy-harvesting applications for a decade. The ultimate goal is to enhance desired properties with minimal resource and production cost in order to serve the technological demands in flat panel displays (FPDs) and energy-efficient windows. Indium Tin Oxide (ITO) has been primarily used as transparent electrodes in these applications due to their excellent properties [1]. Unfortunately, a scarcity has occurred due to rapid growth in demand and sensitivity to Hydrogen plasma atmosphere, the scarcity of its use has attracted extensive research to the search for substitute materials [2]. ZnO which is non-toxic, abundant shows promise in finding applications in TCO due to its intrinsic properties, namely, n-type semiconductor, transparency in the visible range and durability in extreme atmosphere [2]. These advantages make ZnO an attractive prospect to replace a metallic-based TCO [3]. However, intrinsic properties of ZnO-based TCO are relatively inferior to metallic materials due to oxygen desorption and the chemisorption processes at the surface [4]. Typically, heat treatment and doping processes are able to enhance the optoelectronic properties in a semiconductor [5]. Either by improving crystallinity or by alloying with dopants to the lattice, the desired properties could improved in order to find applications in frontier technology [4].

Therefore, the simultaneous incorporation of two types of dopants or co-doping mechanisms was employed to enhance the optoelectronic properties of ZnO-based film in these studies. However, the critical issue is the solubility of dopant into host lattice, which is strongly dependent on mismatches of atomic size and electronegativity needed solving [6,7]. Previous literature reported difficulties in controlling the micro-elemental distribution due to the low solubility of dopant resulting in properties degradation in practice [5,8]. *Yamamoto.T et al.* proposed the mechanism to increase the solubility and a diffusion resulting in the ionic charge distribution increased [9]. By using donor as the reactive at the ratio of Acceptor-to-Donor (A/D) = 2:1, the attractive force of the A-D-A cluster between both types of dopant can shift the energy

levels of donor and acceptor close to a conduction and a valence bands, respectively. After tailoring electronic structures, the electrical properties improved [10].

In addition, dopant solubility will be described in terms of crystallographic studies and thus correlate to optoelectronic properties of as-annealed ZnO-based TCO films. Acceptor or p-type dopant has potential to improve dopant solubility by forming a substitutional defect due to the similarity of atomic radius and extremely low formation energy. Therefore, a less distorted crystal structure reflected by a small variation in lattice parameters would be expected when doping p-type [11], especially Lithium, which is easy to diffuse into ZnO lattice. The ZnO lattice reported to be doped at high concentration (up to 30%) [12]. However, Li^+ is stable and acts as both substitutional acceptor (Li'_{Zn}) and interstitial donor (Li_i) in ZnO [13]. Therefore, it preferably forms a defect complex such as ($Li'_{Zn} - Li_i$) or transforms by a dissociative (Frank-Turnbull) mechanism. Both mechanisms inactivate electronic behavior of defect or hole. In addition, there are many difficulties in attaining p-type ZnO, namely a self-compensation by native defects and a preference for forming a deep-level acceptor [14]. Interestingly, the co-doping with trivalent dopants was reported to delocalize deep-level acceptor in N-doped ZnO [15].

Specifically, two n-type dopants, Al^{3+} and Ga^{3+} which have been used extensively to improve electrical properties by providing free electrons into host lattice [6] show promising potential to be co-doped with Li^+. However, a highly reactive Al^{3+} leads to oxidization during the film's growth resulting in oxygen vacancies ($V_{\ddot{O}}$) and decreased electrical conductivity at %Al >1.6%wt [16]. On the other hand, Gallium (Ga^{3+}) is less reactive [17] and has the comparable size of Ga^{3+} and Zn^{2+} which show contradiction in the solubility limit and defect types. These limitations indicate that it would be challenging to increase performance of ZnO-based TCO by using only one dopant. Therefore, it is noteworthy herein to report the co-doping mechanism in these combinations of dopants in order to enhance optoelectronic properties of ZnO-based TCO in these studies.

Moreover, the economically-versatile thin film fabrication process called electrospray deposition (ESD) will be equipped to prepare a high quality film in ambient condition. This technique shows a high potential in preparing a wide-range of particle size and materials as well as large-scaled applications. By optimizing the crucial process parameters, namely an applied voltage, a deposit distance, a deposit flow rate, a deposit time, a deposition temperature and physical/chemical properties of the precursors, homogeneous and highly-dense films can be

obtained. Thanks to a high electrical field, a mono-dispersed with controllable jet size of charged droplets can be deposited with very high deposition rate [18]. Compared to radio frequency sputtering, chemical vapor deposition (CVD), pulse laser deposition (PLD), and spray pyrolysis, ESD is a far more flexible process without requiring any sophisticated apparatuses. Unless this technique had been developed for a decade, a quantitative study of each process parameter affecting the quality of as-prepared film has been rarely reported in statistical approach. Therefore, the factorial design of the experiment will be adopted in this work to determine significance of each process parameter towards the % film covering area of as-annealed film preparing by electrospray deposition.

LITERATURE REVIEW

A. Tranparent conductive oxide (TCO)

Transparent Conductive film has possessed a wide range of applications and has been developed for a long time in both electronic and optical industries. The evolution of this technology started from metallic materials, such as Gold (Au) and Silver (Ag) [19], then was converted to semiconducting material and oxide materials such as Indium Thin Oxide (ITO). All attempts aimed to overcome the shortcomings, which related to durability in extreme weather such as hydrogen plasma condition [20-22]. In addition, the limitations of resource inquiries and the cost of production have changed the trend of development to insulating materials such as ceramic oxide [21,23]. However, the inferiority of ceramic-based TCO has led to extensive research for a decade to improve the performance as high as metallic-based TCO. Alloying with dopant provides a great opportunity to find an application in any frontier industry, such as near-UV emitting diodes, UV-detectors and transparent thin-film transistors (TTFTs) [22]. Further examples are more applications in the automotive field, such as the ice-free low-E coated windshield, heat reflective coatings on solar collectors and incandescent bulbs [24]. One would say that the novel functionalities may be integrated into the materials by making use of a variety of elements and crystal structures [22]. Below Figure 1 shows the TCO layer for energy applications.

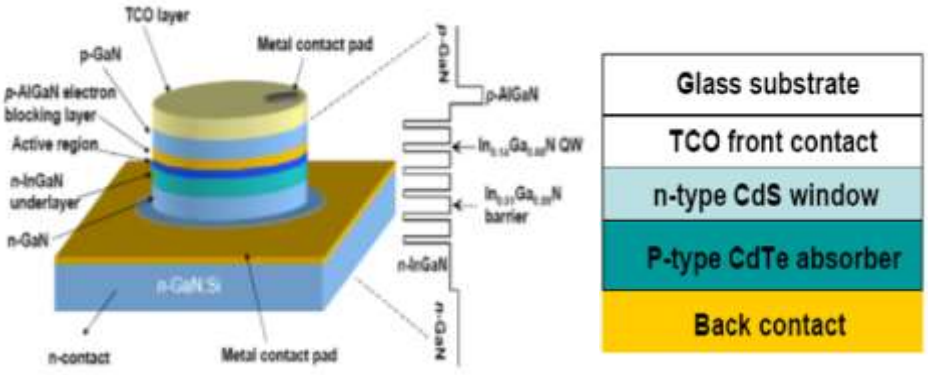

Figure 1. The schematic picture of TCO for energy application [25].

Basic requirements for transparent conductive oxide (TCO) are electrical resistivity as low as 10^{-4}-10^{-3} Ω-cm, a carrier concentration > 10^{20} cm^{-3}, an optical band-gap energy > 3.0 eV

and transmittance in visible range > 80% [26-30]. Both In_2O_3 and SnO_2 are promising candidates due to they possess a band-gap energy (E_g) > 3.0 eV with free carrier density above 10 [19-20] cm^{-3} and mobility higher than 1 $cm^2V^{-1}s^{-1}$ resulting in an electrical conductivity as high as $10^4\ \Omega^{-1}cm^{-1}$ [31]. Owing to its intrinsic electronic defects and wide band-gaps energy of Wurtzite structure, ZnO also shows a high potential to fulfill aforementioned requirements. Previous reports revealed that ZnO with dopant shows promising in replacing metallic-based TCO. For example, Aluminum (Al)-doped Zinc Oxide (AZO) has been intensively studied and can be classified as n-typed semiconductor. Copper (Cu)-doped ZnO has the same magnitude of electrical conductivity as TCO for circuit applications, such as passive matrix LED, see-through solar cell, and electrochromic windows. The schematic figure in Fig.2 demonstrates the component of electrochromic smart windows and its mechanism.

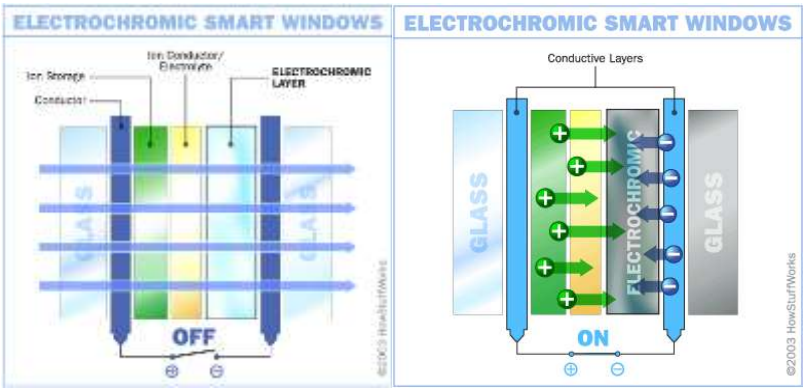

Figure 2. Electrochromic window and its schematic work [32].

The quality of the transparent conductive film (TCF) depends on a thin film fabrication technique and the material's characteristics. The major problem is the polycrystalline structure which contains vast amounts of point defects, grain boundaries and preferred-oriented crystallization and acts as scattering centers, as shown in Fig.3 [22]. In order to attain a high quality, an epitaxial or single crystalline film is favorable which requires a sophisticated apparatus to synthesize. Unless the ceramic is polycrystalline and mostly opaque, it is capable of fabricating thin layers and provides translucency or transparency, which can then be applied for optoelectronic application. However, such a thin layer still needs to be coated on single, fully dense or amorphous materials like glass substrate [33]. Therefore, it is necessary to keep in mind

that substrate types also have an effect on TCO that needs to be considered in thin film fabrication processes. Glass, sapphire and polymeric substrate (i.e. PET, PC and PPA) are commonly used to prepare thin film depending on application condition and the nature of substrate [26]. Among these materials, glass is the most versatile substrate for transparent electronic devices and building materials due to its price, smoothness, potential to implement in mass production [31] and availability. Interestingly, glass is capable of blocking infrared incidents (>2,000 nm) and converting them to generate heat in return, which is suitable for optical applications.

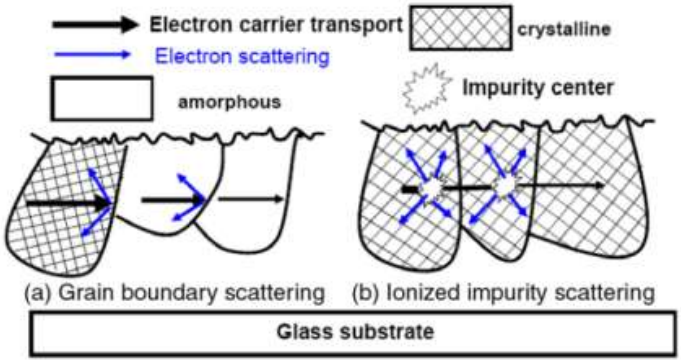

Figure 3. A schematic pictures of scattering on (a) grain boundary and (b) ionized impurity scattering [25].

In addition, the fabrication method plays a vital role to the quality of TCO. In vapor-phased deposition methods, which is commonly used in large-scaled application, there are many difficulties in controlling deposit conditions and composition [22]. For example, the conventional vapor-phased epitaxial (VPE), [26,34] direct current (DC) or radio frequency (RF) magnetron sputtering, chemical vapor deposition (CVD), pulsed-laser deposition (PLD), Molecular Beam Epitaxy (MBE) [27,35,36]. Other fabrication methods such as sol-gel, spray pyrolysis, reactive evaporation, electron beam evaporation, chemical bath deposition (CBD), metal organic chemical vapor deposition (MOCVD), Atomic Layer Deposition (ALD) and spin coating are also equipped to fabricate thin layers [21,29,30,37-40].

B. Zinc oxide

Zinc oxide (ZnO) has been extensively applied in many fields of application due to its intrinsic properties. For example, its excellent thermal shock resistivity of ZnO can enhance a densification process of ceramics over a range of sintering temperatures [33]. Therefore, it has been used as an active flux in the Chinese whiteware industry. In addition, ZnO can be used as an additive for rubber and plastic industries, as a catalyst in pharmaceuticals, cosmetics (sun cream) products and as coating materials for paper. Moreover, ZnO has been used in Ni- or Mn-Zinc ferrite, as an ingredient in phosphors, Surface Acoustic Wave (SAW) filters and transparent electrodes. Moreover, ZnO can easily find an application in piezoelectric and optoelectronic fields [41]. For example, varistors, transparent high-power electronics, piezoelectric transducer, UV and chemical gas sensor, [42,43] solar cell and Light Emitting Diode (LED) [41].

ZnO exhibits three different crystal structures: Wurtzite (hexagonal), Rock salt (cubic), and Zinc blended (cubic) shown in Fig.4. It is typically stable in the Wurtzite structure, while the rock salt structure exhibits at high pressure. The closed-packed (0001) plane is made up by two sub-planes. Each sub-plane consists of the cationic (Zn) and the anionic (O) species. This asymmetry structure leads ZnO to exhibit piezoelectric properties [37,44] due to the polarity of the c-axis between the Zn-terminated and O-terminated planes exhibits vastly different characteristics [45]. Additionally, the large portion of the open-spaced Wurtzite structure compared to rock salt one, Wurtzite ZnO properties can be improved by a doping approach in the heavily-doped condition [46].

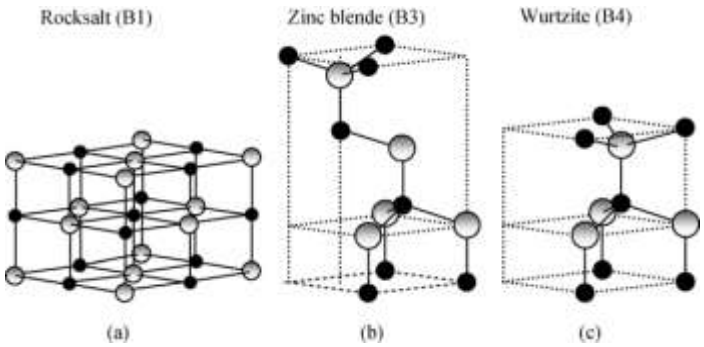

**Shaded gray and black spheres denote Zn and O atoms, respectively*.

Figure 4. A variety of ZnO crystal structure: (a) cubic rocksalt (B1), (b) cubic zinc blende (B3), and (c) hexagonal Wurtzite (B4) [45].

From an electronic point of view, ZnO intrinsically belongs to n-type semiconductors, but interesting research re-emerged in optoelectronic application since p-type property was discovered [18]. In addition, the low work function of ZnO paves the bright way to fabrication at low temperature use for making transparent electrodes in OLED [26]. In addition, a wide band-gaps energy (E_g) and transparency in the visible range make ZnO become a promising candidate for optoelectronic applications [18]. The Wurtzite structure of ZnO has a direct band-gaps energy of 3.37-3.40 eV [38,47] at which the inter-band transition occurs (the Brillouin zone center, k=0) [47]. Three degenerating energy levels in between the band-gaps at valence band also provide the chance to tailor electronic band structure by extrinsic impurities or doping mechanisms as shown in Fig.5. Either shallow-level or deep-level defects can be generated with respect to a magnitude of ionizing energy which induce both beneficial and deleterious effects on electrical properties. For example, divalent Cadmium (Cd^{2+}) ion was reported to induce band-gaps narrowing, whereas Mg^{2+} enlarged one due to band filling or Burstein-Moss effects [43].

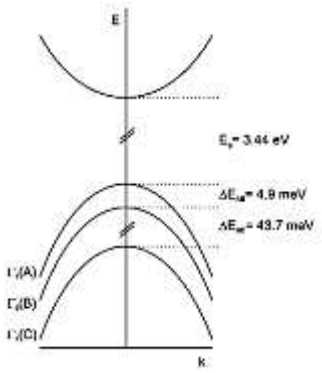

Figure 5. A spin-orbit splitting diagram of three sub-bands of ZnO valence band [47].

Regarding the aforementioned optical and electrical intrinsic properties, ZnO has been categorized into the class of transparent conductive oxide (TCO) likewise, Indium oxide (In_2O_3) and Tin oxide (Sn_2O_3). Interestingly, ZnO-based TCO has been reported that either amorphous or crystalline structures can be utilized as TCO materials [48]. Recently, fundamental and applied research on ZnO experienced a renaissance to develop Zinc oxide for blue and UV laser. However, for energy application, ZnO-based thin film still gets the attention for solar cells (windows) due to cost competitiveness and it's non-toxic for large-scale production as well as

thermal its chemical stability in harsh conditions [20,35,37,38,49]. By improving ZnO film properties, this material possesses a high potential for photovoltaic in renewable energy research[18].

The basic physical properties and parameter of ZnO are described in the table below [22].

Table I. Summary of Physical Properties of Bulk ZnO

Basic physical properties and parameter of ZnO	**Description**
o Molecular mass	81.389 amu.
o Specific gravity at room temperature (RT)	5.642 gm/cc.
o Crystal structure and point group	$P6_3mc$, 6 mm. Wurtzite
o Lattice constant at 300 K (nm)	a = 0.32495, c = 0.52069 c/a = 1.602 (1.633 for ideal hexagonal structure)
o Bulk hardness	u = 0.3825 – 0.345 [43]
o Melting point	5 GPa
o Electron effective mass, m_e	2250K (1975 ℃) [43]
o Hole effective mass, m_h	0.24 [43] - 0.28 m_e
o Electron mobility at 300K	0.59 [43] - 1.80 m_e
o Hole mobility at 300K	200 [43] - 205 $cm^2.v^{-1}.s^{-1}$
o Band-gap (Eg)	5-50 [43] or 180 $cm^2.v^{-1}.s^{-1}$
o Specific heat	3.37 eV – 3.40 eV (direct) [43]
o Thermal conductivity	0.125
o Thermal electric constant at 573K	0.006 cal/cm-K
o Piezoelectric constant	1200 mV/K
o Bond enthalpy	1.2 C/m^2
o Work function	159 ± 0.4 per kJ mol^{-1}
o Specific dielectric constant	4.25 eV
o Extinction binding energy	8.656

o Shear modulus	60 meV
o Reflective index	45.5 GPa
o Electron affinity	2.008 – 2.029 [43]
o Energy of Cohesion	4.2 eV
o Band-gap temperature coefficient	1.89 eV
o Saturation electron drift velocity	2.9×10^{-4} ($eV.K^{-1}$)
o Index of refraction	107 cmS^{-1}
o Density at 300K	(1 micron) / (0.45 micron)
o Linear expansion coefficient	5.606 $g.cm^{-3}$
o Intrinsic carrier concentration	$a_0 = 6.5 \times 10^{-6}$, $c_0 = 3.0 \times 10^{-6}$ per °C $<10^6$ per cm^3 [43]

C. ZnO defect chemistry

In general, types of defects in semiconductors can be divided into three groups, namely, intrinsic or native defects (vacancies and interstitial), extrinsic defects (dopants) and extended defects (grain boundary, dislocation and stacking fault). Not only two first type point defects are vital, the interaction between them and extended defects also play the role of semiconductor properties by reducing formation energy which affects defect mobility [50] and diffusion in growth processes [51].

Unless ZnO has been studied for a decade, the mechanism of defect and combination in very rich defect chemistry of ZnO lead to continually inquire more understanding in order to maximize the ZnO performance in many applications, especially for thin film which has a very small surface-to-volume ratio and defects have strong influence to their surface properties [46]. Both experimental and theoretical studies have been performed to indicate main point defect species of ZnO and the characteristics of their properties. Owing to two different occupancy sites combining between a hexagonal-closed packed structure half-filled with Zn in a tetrahedral site, and the open-spaced in octahedral sites, ZnO is ready to be filled with defects [46]. However, ZnO shows asymmetric doping behavior, meaning that ZnO can easily exhibit n-type semiconductor, but is difficult to generate p-type one. This behavior is also observed in ZnS and $CuGeSe_2$, which only shows n-type and p-type semiconductor, respectively [52]. Therefore, it would be challenge to

develop p-type ZnO-based materials. Moreover, a reproducibility, a self-compensation, a preference of deep-level defect, and a low solubility of dopant also raise difficulties to achieve p-type semiconductor [43].

In general, the defect chemistry in ZnO can be divided into two types of defects as described in the following:

1. Native or Intrinsic defect

Intrinsic defects can consist of a missing atom (vacancy) or an occupying atom in interstitial site (or interstitialcy). They are abundant in lattice and strongly dependent on dopant concentration and thermal vibration. Both defects dictate the magnitude of diffusion or migration in the lattice [53]. The growth condition and formation energy play crucial roles in determining the defect types [54]. *S.B. Zhang et al.* reported that interstitial Zn ($Zn_i^{\cdot\cdot}$), a shallow-level donor forms easily in Zn-rich atmosphere, whereas either Zn-rich or O-rich condition, low formation enthalpy, leads to form large amounts of n-type intrinsic defects, namely anti-site O (Zn_O^x), interstitial Zn ($Zn_i^{\cdot\cdot}$), oxygen vacancy (V_o), oxygen interstitial (O_i'') and Zinc vacancy (V_{Zn}'') [52], which is in agreement with first principle calculation studies [14] and hybrid QM/MM studied by *A.A. Sokol* group [54].

In addition, ZnO exhibits n-type semiconductors due to defect formation energy, owing to a high formation enthalpy of defects, namely interstitial oxygen (O_i'') and Zinc vacancy (V_{Zn}''), it is these defects, which are n-type compensating defects or electron killers that are rarely observed. Consequently, ZnO with donor-type defect species brings n-type semiconductor behavior that causes difficulties in creating p-type ZnO [52,55]. Moreover, the formation energy of donor-type defect is very low and is likely to decrease with carrier concentration increases [56]. From a thermodynamic point of view, *Oba et al.* revealed that the formation energy of defects are strongly dependent upon atomic chemical potential that can be tailored by changing condition from O-rich to Zn-rich.

From an electronic point of view, there are three major ZnO intrinsic defects that play a role in ionic conductivity. They can be categorized by defect charges, namely donor, acceptor, and neutral defect. The first group consists of Zinc interstitial ($Zn_i^{\cdot\cdot}$) and Oxygen vacancy ($V_{\ddot{O}}$). The second group comprises of Zinc vacancy (V_{Zn}''), Oxygen interstitial (O_i''). Lastly, the substitution process induces Oxygen anti-site (O_{Zn}^x) and Zinc anti-site (Zn_O^x) which show

neutrality in ionic conductivity. Among these types of defects, the donor-type defects ($Zn_i^{\cdot}$ and $V_{\ddot{O}}$) play the most important roles in electrical conductivity, which can be quantified by the Hall effect measurement [56].

The below diagram in Fig.6 shows ionization energy of defects ranging from 0.05-2.8 eV;

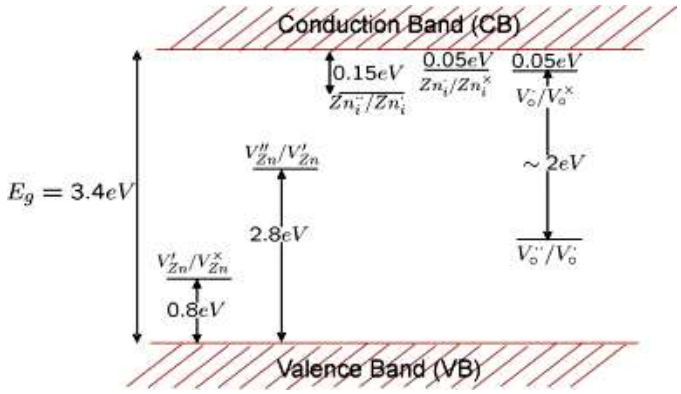

Figure 6. The energy-level diagram of native defects in ZnO [46].

According to the energy-level diagram, there are two defect reactions contributing to intrinsic defect of ZnO listed in following table; [46]

Table II. The Defect Chemistry in ZnO

Defect reaction	Further ionization	Equilibrium constant
1. Frenkel defect from Zn	$Zn_i^x \leftrightarrow Zn_i^{\cdot} + e'$	K = $2N_C\,(-0.05/kT)$
	$Zn_i \leftrightarrow Zn_i^{\cdot\cdot} + e'$	K = $21/N_C\,(-0.15/kT)$
2. Schottky defect from O	$V_O^x \leftrightarrow V_{\dot{O}} + e'$	K = $2N_C\,(-0.05/kT)$
	$V_{\dot{O}} \leftrightarrow V_{\ddot{O}} + e'$	K = $21/N_C\,(-2.0/kT)$
	$V_{Zn}^x \leftrightarrow V_{Zn}' + h^{\cdot}$	K = $2N_C\,(-0.8/kT)$
	$V_{Zn}' \leftrightarrow V_{Zn}'' + h^{\cdot}$	K = $21/N_C\,(-2.8/kT)$

Where N_C is defect concentration and T is temperature.

According to equilibrium constant equation, the ionization energies are strongly dependent on relative defect concentration (N_C) and annealing conditions (temperature and atmosphere) [46]. The most of donor defects were formed at 500 °C, as previously reported [43].

In addition, growth conditions with different partial pressures induce a native defect to form the following [57]:

- In Zn-rich condition, the Zn (g) will be captured and generate an oxygen vacancy ($V_{\ddot{O}}$);

$$Zn\,(g) \;\rightarrow\; Zn_{Zn}^{x} + V_{\ddot{O}}$$

- In O-rich condition, Zn can alter to be gas phase, $Zn\,(g)$;

$$Zn_{Zn}^{x} \xrightarrow{\text{ZnO}} Zn\,(g) + V_{Zn}''$$

- Then the charge neutrality condition takes place;

$$V_{Zn}'' + 2h^{\cdot} \rightarrow V_{Zn}^{x}$$

However, the ionized donor defect on the surface can be easily oxidized by chemisorption reaction which can be degraded TCO properties as following equations [58];

$$\begin{aligned}
Zn_i^{\cdot\cdot} &\leftrightarrow Zn_i^{\cdot} + e^- \\
Zn_i^{\cdot} &\leftrightarrow Zn_i^{\cdot\cdot} + e^- \\
V_O'' &\leftrightarrow V_O' + e^- \\
V_O' &\leftrightarrow V_O^{x} + e^- \\
O_2 + e^- &\leftrightarrow O_2^- \textit{ (ads)} \text{ at } T< 150^{\circ}C
\end{aligned}$$

The resultant negative oxygen (O_2^-) reduces carrier mobility which decreases electrical conductivity of ZnO thin film. Furthermore, the desorption reaction decreases the amount of negative oxygen ions if there exists a hole (h^+) by following reactions which raise difficulties to obtain p-type ZnO [41];

$$O_2^- (ads) + h^+ \rightarrow O_2$$

There are various methods and hypotheses of defect formation that have been performed to investigate native defects of ZnO in both calculation and experimental studies. First-principle method based on plane-wave pseudo-potential [52,56,59] and density function theory (DFT) [51] have been commonly used to study. Whereas, many experimental-based methods, namely, electron paramagnetic resonance (EPR), cathodoluminescence (CL), deep-level transient spectroscopy, positron annihilation spectroscopy and perturbed angular correlation spectroscopy have also been used. However, resonance studies may not be reliable enough by nature to investigate when periodic structure change by point defects [54] resulting in a controversy in the research and is still debated [56].

A.A Sokol et al. reported the localized state of point defects of ZnO by using hybrid quantum mechanical/molecular mechanical (QM/MM) systems. They claimed that both scales of studies were needed to be adopted in point defect studies due to point defect is a periodically long-range effect, but the electronic state of point defect is atomistic scaled [54].

2. Extrinsic defect or impurity

An extrinsic defect can be recognized as solute and impure depending on the intention. It can substitute or reside in an interstitial site of lattice in accordance with atomic size and electronegativity [7]. Small radii species prefer being interstitial whereas larger ones love to replace host atoms. Typically, the interstitialcy is unlikely to be bound and possesses high energy [53]. Excessive charge from heterovalent species are adopted and raise the complicated issue in defect formation because a compensation mechanism is required to keep charge of the neutrality condition [53]. Another issue of defect introduction is the solubility of the impurity center in host lattice. The homogeneity and random well dispersion of defect are favorable. The high solubility can be reached in case of similar atomic radii (15%), structure, electronegativity and valence state [60]. Many studies revealed that the greater the difference of ionic radius, the more lattice stress will be introduced, which leads to lattice deformation [61]. Consequently, the adverse effect can be generated to reduce desired properties of materials.

Thanks to the open structure of hexagonal closed pack of Wurztite with 50% occupied with Zn-atom, both native defects and impurities can be accommodated in host lattice, which

would be benefit to enhance electrical, optical and magnetic properties [46,53]. The impurity can be divided into two groups, namely, donor (n-type) and acceptor (p-type) [53]. Fundamentally, dopants improve electronic properties by increasing effective carrier concentration to shift Fermi level energy close to a conductive band. Moreover, point defects and ionized species also increase charge carriers. Consequently, the total carrier concentration is modified by the performance of doped materials. However, the latter group of carrier has strong effects on the mobility by scattering effect [62] which needs taking into an account in order to optimize final properties [48]. The comprehensive knowledge of extrinsic defects will be discussed in the following section.

D. Dopants and co-doping mechanism

Generally, there are three main factors affecting the electrical and optical properties of TCO namely, growth condition (type of substrate, temperature and atmosphere), thickness of thin film and doping mechanisms (type and concentration) [26]. In this work, the doping concept will be focused due to dopants or extrinsic impurities is more stable than intrinsic ones and provide the chance to customize electrical properties of undoped ZnO [44]. Both types of dopant straightforwardly increases the number of effective charge carriers (concentration) and electrical conductivity in accordance with following equation [26]:

$$n_0\, p_0 \;=\; n_i^2 \qquad (1)$$

Where n_0 and p_0 are conductive electron and hole concentration respectively. n_i is effective carrier concentraion of ZnO.

Unless dopants can benefit electrical properties, it also induces free carrier absorption and high plasma resonance reflectivity, which reduce optical transmittance of the film as well as carrier mobility in heavy-doped conditions. In addition, the effect of carrier concentration on optical band-gaps follows the concept of Mott criterion (Metal-insulator transition) meaning that the Burstein-Moss effect and band-gaps narrowing mechanism can be observed in the doped sample with respect to the carrier concentration [26]. Therefore it is necessary to optimize both ends of effect when employing a doping scheme.

There are two dominant extrinsic defects or dopants that can be described as the following:

1. **N-type dopant**

This group of dopant possesses a highly conductive effect when being doped in ZnO-based-TCO. It frees electrons into the lattice to increase the number of electrons in the conductive band [6,63]. Group III, trivalent metal, is a single-electron donor, whereas Ge and Si are multi-electron donors [40]. Trivalent dopants are preferable due to how they can increase thermal and chemical stabilities in harsh conditions [23]. Moreover, they are abundant and innoxiousness making fabrication processes much safer and cheaper. The most promising dopants of group III for ZnO-based TCO are B^{3+}, Al^{3+}, Ga^{3+} and In^{3+}. [39]

Aluminum (Al^{3+}) has become the most interesting in the development of ZnO-based TCO among group III dopants due to chemical stability, price and environmentally-benign matter. [29,36] It has a very high reactivity which leads to oxidation during the film growth process [64]. *Min-Chul Jun et al.* reported that below 0.5% of Al^{3+} content, no stress was observed in Wurtzite structure [21]. *H.Kim et al.* reported that 0.5%Al-doped ZnO fabricated by PLD at low temperatures showed the lowest resistivity of $2.5x10^{-4}$ Ω-cm and %Transmittance more than 90% in visible range on glass substrate with 300 nm in thickness [49]. A large size difference between Al^{3+} (0.53 Å) and Zn^{2+} (0.72 Å) introduces high stress-strain effect on the lattice. Consequently, the degenerated issue causes reduction of lateral surface expansion and restricts grain growth process resulting in crystallite size and crystallinity decrease as well as pore population increases [34,65]. Substantiate studies have been reported the effect of grain size of AZO on electrical performance and suggested that the greater average grain size, the lesser electrical resistivity because the effect of the grain boundary was diminished [66].

At Al > 1.6%wt., defect cluster was energetically-favorable and formed with O^{2-} resulting in oxygen vacancy ($V_{\ddot{O}}$) and conductivity decreased reported by *Shou-Yi Kuo* [16] and *Zi Qiang et.al* [67] which were in agreement with the Density Of State (DOS) studies by *Yamamoto* because highly-doped ZnO preferred to localize and stably formed a substitutional defect ($Al_{Zn}^{\cdot}$) [68]. More recent studies by *Doo-Soo Kim et al.* reported that Al-doped ZnO in O-rich atmosphere by Magnetron sputtering process, an interstitial defect (Al_i) energetically bound with O^{2-} and formed AlO_6 defect cluster as seen in Fig.7. This second phase shifted X-ray diffraction peak to higher

2θ and provided a smoother surface, but decreased carrier concentration in return [35]. Therefore, Al can be doped just in a certain amount. Another drawback of doping Al^{3+} is carrier mobility reduction when Al concentration increased reported by *J. Mass et al.* [69] because Al^{3+} is too small to substitute, so Al interstitial (Al_i''') will be free inside the ZnO lattice and eventually act as a scattering center which reduces electrical conductivity. In addition, the first-principle study by *Steiauf et.al* and *J.T-Thienprasert et.al* indicated that the defect complex between Zinc vacancy and Al substitutional defect ($V_{Zn}'' - Al_{Zn}$) could be formed and increases migration barrier of the vacancy-impurity exchange process. Consequently, the carrier concentration and mobility can be reduced [70,71].

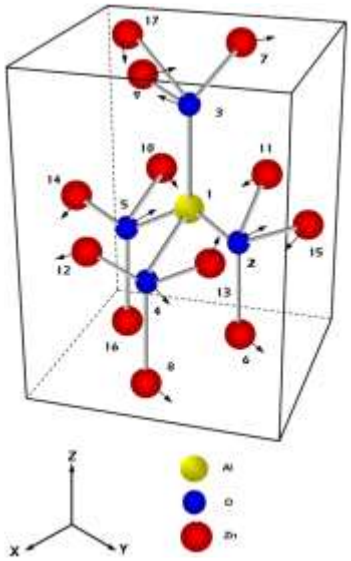

Figure 7. A schematic diagram shows vicinity of Al^{3+} in the Wurtzite structure [6].

Unless Al-doped ZnO has limitation, there are a myriad of interesting researches that are still trying to enhance the performance of AZO as high as Indium-doped Tin Oxide (ITO) in order to reduce cost and abide by the environmentally-friendly theme. Therefore, Al-doped ZnO can grow in various deposition methods such as atomic layer deposition (ALD), sol-gel or chemical vapor deposition (CVD) and provide desired results of carrier density ranging from 10^{18} -10^{21} cm^{-3} and 10^{-2} to 10^{-4} Ω-cm of electrical resistivity [63]. By using reactive pulse magnetron sputtering AZO with Hall mobility of 46 cm^2/V-s, the electrical resistivity of 2.26x10^{-4} Ω-cm and free electron density of 6.0 x10^{20} cm^{-3} can be obtained [72]. Additionally, Al^{3+} induces

the Burstein–Moss effect resulting in band-gaps widening and blue-shifted absorption edge in the ZnO nanostructures due to carrier density increases which can be detected by UV peaks and Photoluminescent (PL) spectra [61]. Furthermore, in heavy-doped condition of Al, it can induce more absorption of near-infrared (NIR) incident to improve optical performance in a visible range of ZnO-based TCO. [73]

Gallium (Ga^{3+}) is another highly potential dopant for ZnO among group III elements because it provides the lowest electrical resistivity without optical properties degradation. However, Ga^{3+} is less reactive than Al^{3+}, so Ga-doped ZnO (GZO) becomes more resistant to oxidization compared to Al-doped ZnO [39,64]. *Ghosh et al.* reported that the lowest resistivity of GZO on polymer substrate was about 2.8×10^{-4} Ω-cm with 1100 nm thickness (Sheet resistance 2.5 Ω/□) with Hall carrier mobility of 18 cm^2/Vs. and carrier concentration of 1.3×10^{21} cm^{-3} can be achieved and exhibited by the solar efficiency conversion up to 9.52% [32]. The *ab* initio studies suggested that Ga^{3+} induced shallow-level donor can reduce Madelung energy as twice times as Al^{3+} does when substituted on Zn-site (Ga_{Zn}). This makes gallium (Ga^{3+}) able to stabilize and improve a charge distribution in lattice reported by *Yamamoto* [68]. Moreover, *S.W Shin et al.* reported that the Mg-Ga co-doped ZnO by RF sputtering deposition showed the widest optical band-gaps energy of 3.91 eV with lowest electrical resistivity of 5.3×10^{-3} Ω-cm. This performance attracts interest in many optical applications. [39]

Thanks to comparable atomic radii of Ga^{3+} (0.69 Å) to Zn^{2+} (0.72 Å), lesser effects on lattice distortion than Al-doped ZnO is expected [21]. Consequently, GZO can provide the lowest resistivity associated with a high transmittance in a visible region [64]. The smaller change in bond length between Ga–O and Zn–O minimizes the deformation of the ZnO lattice allowing highly-doped gallium concentrations into ZnO lattice [74] and increases solubility due to the small size mismatch [75]. However, some controversial studies reported that the comparable size of Ga limits solubility of Ga in ZnO structure that prohibits heavy-doped concentration as well as the type of defect would be formed [73,76]. In addition, *J. Zhu et al.* reported that the electronic environment of Ga (electron density) can also affect lattice distortion due to attraction and repulsion forces [77].

2. **P-type dopant**

Lithium (Li) is amphotheric dopant or has bistabililty because it can show both n-type (DX) and p-type (AX) behaviors. A smaller radii of Li^+ compared to Zn^{2+} induces the mobile interstitial donor-like defect (Li_i) to create, whereas the lowest formation energy of anti-site defect (Li'_{Zn}) leads to form an acceptor one. Therefore, both Li-related defects can exist in both deep and shallow-levels of defect which depend on the type of defect that would be formed [78]. Group Ia dopants do not have a d-orbital to raise acceptor levels up as group Ib dopants (Cu, Ag, Au) do so, a substitute defect of Li (Li'_{Zn}) is a deep-level acceptor which raises difficulties to dominate the electrical conductivity by a hole carrier[79]. Therefore, it would be difficult to achieve p-type ZnO by doping Group I dopants.

Li induces various types of defects to form namely, Li'_{zn}, Li'''_O, $Li'_{zn} - Li_i$and $Li'_{zn} - H^{\cdot}$. Owing to comparable size and extremely low substitute defect ionization energy (Li'_{zn}=0.09 eV, Li_i =1.58 eV), Li^+ prefers forming a substitutional defect with Zn^{2+} rather than a interstitial one reported by *Tsai et al.* [12]. Consequently, the small distortion of Wurtzite structure is expected [75]. However, the transformation called Frank-Turnbull or dissociative mechanisms of Li-related defect raise stability issues [80] which can degrade p-type characteristic of ZnO by raising the interstitial defect (Li_i) as the following equation [81,82]:

$$Li'_{zn} \rightarrow \ Li_i \ + \ V''_{Zn} \qquad (2)$$

This mechanism changes anti-site defect (Li'_{zn}) to an interstitial one (Li_i) and Zinc vacancy (V''_{Zn}). Not only an increase in c-axis of lattice parameter can be observed, but a change in semiconducting behavior from acceptor (p-type) to donor (n-type) can be found as well. Especially, in high Lithium doping concentration which is grown in O-rich condition. Consequently, an abnormal shift in 2θ can be observed [81]. Li can be occupied up to 30% at a Zn-site, so it is a highly soluble dopant. Such a heavily doped condition, Li_i will preferentially form Li_2O resulting in lattice distortion due to a Li-O bond length change but this phenomenon benefits to observe the ferroelectric properties.

Unless the instability of the defect type of Li can be observed, Lithium (Li^+) is the most promising candidate for p-type ZnO among other in group *Ia* dopant [80,83]. Some studies reported that Li can improve crystallinity by mitigating distributing stress in the crystallization process [81].

Previous research revealed attempts to produce Li-doped ZnO with various deposition techniques. *Yow-Jon Lin et al.* and *Zaharescu et al.* fabricated ZnO:Li on glass substrate at low Li content by a sol-gel method [81,83]. However, most of the results failed into n-type behavior due to the aforementioned mechanism. *Rauch et al.* studied 0-12% Li doped in ZnO single crystal and revealed that p-type of ZnO:Li can be obtained at ~1%of Li due to a shallow-level acceptor was formed [78]. *Zeng et al.* and *Lu et al.* fabricated Li-doped ZnO film by DC reactive magnetron sputtering and PLD, respectively and achieved p-type LZO with hole concentration of 1.40-6.04 $x10^{17}$ cm^{-3} and hole mobility of 2.65 $cm^2/V\text{-}S$[82]. Some revealed that p-type ZnO:Li can be achieved by adopting a co-doping scheme. For example, (Li,Mg) [81] and (Li,Ni) co-doped ZnO [83] showed transformation of n-type to p-type due to oxygen vacancy was compensated.

3. **Co-doping method**

A simultaneous incorporation of two-kind dopants or co-doping mechanism provides a potential opportunity to increase the properties of materials [84]. For example, Al–In co-doped ZnO thin films showed a higher conductivity than Al single-doped ZnO (AZO). The humid durability enhanced by Al–Ga co-doped ZnO thin films [19] with a higher carrier density, a lower resistivity and a wider band-gap than that of Al-doped ZnO. In addition, the nc-Si solar cell coated with Al-Ga co-doped ZnO transparent thin film electrode. It exhibited a higher conversion efficiency than was previously reported [73]. Typically, an asymmetry doping behavior of ZnO provides us effortless opportunities to obtain n-type ZnO due to vast amounts of intrinsic defects namely, an interstitial Zn ($Zn_i^{\cdot\cdot}$) and an oxygen vacancy ($V_{\ddot{O}}$). In contrast, p-type semiconductor fabrication needs a much higher effort to overcome. *Yamamoto et al.* summarized the key factors of the co-doping scheme to achieve p-type semiconductor in wide band-gaps materials, such as ZnO, GaN and ZnS. By forming a acceptor-donor defect cluster (A-D-A) at an optimal ratio of acceptor-to-donor (A/D) of 2:1, a p-type ZnO semiconductor can be obtained by following mechanisms [15]:

1. The incorporation of trivalent dopants delocalizes deep-level acceptor after acceptor-type dopant is added by co-doping process.
2. The attractive force in the acceptor-donor-acceptor (A-D-A) defect cluster overcomes the repulsive force which improves p-type dopant solubility into lattice compared to mono p-type dopant.

3. The defect cluster tailors an electronic structure by shifting the donor energy level close to conduction band (CB) and lowering the acceptor energy level downward to valence band as seen in Fig.8.

In addition, these mechanisms contribute to improve the electrical performance of the wide-band-gaps materials as following [132];

1. The donor-acceptor defect cluster increases the lattice stability by decreasing Madelung or lattice energy. Consequently, the lattice becomes more stable and well-charged distribution.
2. The trimmer-like and non-random configuration of a donor-acceptor defect cluster (A-D-A) reduces the ionization energy of defect by impurity. Therefore, the population of ionic and electronic defects increase [15].
3. The donor-acceptor defect complex enhances a carrier's mobility by reducing the short-range dipole-like scattering mechanism resulting in electrical resistivity decreases [132].

The crucial factor required to improve a dopants solubility, which was reported in an achievement of p-type semiconductor, is a high affinity between acceptor and donor, or "reactive codopant". In order to strengthen the defect cluster of co-dopants, the cohesive energy of both types of dopants would be higher than that of a dopant and host ions, which may lead to reduce solubility of a dopant in host. However, the binding or cohesive energy which is a strong dependent on atomic radii and dielectric constant of the medium can be estimated through the following equations [68]:

$$E_B = \frac{q^4 m_{e(h)}}{2\varepsilon^2 \hbar^2} \quad (3)$$

Also Bohr's radius can be derived by;

$$a_{d(a)} = \frac{\varepsilon \hbar^2}{m_{e(h)} q^2} \quad (4)$$

Therefore, E_B can be expressed in term of Bohr's radius as following;

$$E_B = \frac{1}{a_{d(a)}} x \frac{q^2}{2\varepsilon} \quad (5)$$

Where E_B is binding energy, q is electron charge (1.602x10^{-19} Coulomb), $m_{e(h)}$ is effective mass of electron or hole, ε is dielectric constant, ħ *is reduced Plank's constant (1.054x10^{-34} J-s) and $a_{d(a)}$ is Borh's radius of donor or acceptor.*

According to the above equations, large band-gaps materials which have low dielectric constant (ε) would be expected to encounter the low binding energy between host and impurity [15]. Therefore, a large Bohr's radius or atomic radii dopants would be the main concept to increase a dopants solubilty by a co-doping scheme.

The schematic Figure below shows a energy diagram of doping and co-doping mechanisms proposed by *Yamamoto et al*.

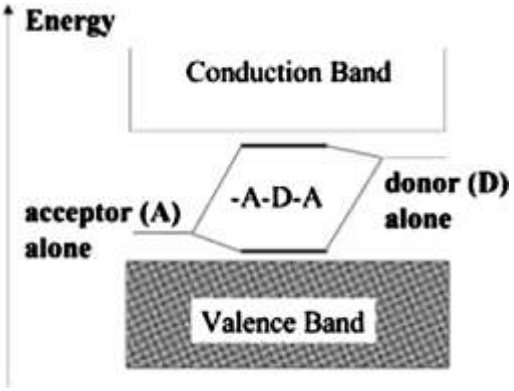

Figure 8. A Schematic energy diagram of doping and co-doping mechanism [75].

Implementing a co-doping concept, a solubility and a diffusion [85] of dopant was enhanced resulting in an electrical performance improvement [75][132]. *Joseph et al.* successfully fabricated p-type ZnO by employing co-doping of Ga-N to ZnO film from PLD combined with a plasma gas source technique. Nitrogen (N) was used as a swallow-level acceptor whereas Gallium (Ga^{3+}) was used as the donor. In O-rich atmosphere, the oxygen vacancy ($V_{\ddot{O}}$) was suppressed resulting

in introduced p-type dopant formed holes to dominate the electrical conductivity [84]. However, the low solubility of N in ZnO lattice due to small radii was the main issue to limit increases of hole concentration and the electrical conductivity [75].

In addition, previous work also reported that the electrical conductivity of co-doped ZnO-based TCO was reduced because the mobility decreased by scattering of the defect cluster and grain boundary [72]. However, the most recent study revealed that a 2% Boron and 6% Fluorine co-doped ZnO fabricated by electrospray deposition attained the lowest resistivity of 1.01×10^{-4} Ω-cm with high optical transmittance of 98% and high carrier concentration of 3.40×10^{21} cm^{-3}. However, Fluorine (F) is still classified as a moderate toxic material and it may cause difficulty to operation in the large scale [2]. In addition, Fluorine would substitute with Oxygen ($F_{\dot{O}}$) to form an acceptor-type defect [26] resulting in a compensating effect and a reduction of effective charge carriers would be observed. Moreover, the specific temperature required to fabricate F-doped ZnO [19].

E. Electrospray deposition (ESD)

Electrospray deposition (ESD) is the method of how electrical-atomized liquid precursor is deposited on the target substrate governed by a remarkably "soft" electrical force [86]. Atomization of liquid by electric force has held three crucial advantages among other techniques namely, mono-dispersed droplet, highly-charged surface and controllable droplet size without coagulation [18]. There are four steps to fabricate the thin layer by this method [87]. To begin, a high voltage is applied to generate an electric field between a precursor-containing capillary and the collector. Second, the charged liquid is pushed through the capillary after overcoming surface tension and splits into the droplet [88]. Then a charged droplet is sprayed from the tip of the nozzle. Lastly, the fine droplet is collected onto the heated substrate by accommodating the applied electric field [86,87,89]. The strong electric field induces meniscus to form and elongates liquid to form a conical-shaped jet of charged droplets [88,90]. Consequently, charged droplets transform the macromolecule of liquid into the gas phase [91]. There are two forces playing crucial roles in forming liquid jet namely, the bulk force on jet and the normal-tangential stress at liquid surface. The bulk force consists of four types called electrodynamic, gravitational, inertia and drag forces. The latter group is strongly related to interactions between local impact and liquid demonstrated by stress tensors between pressure, liquid viscosity and inner-phase surface etc. [88]. The

morphology and microstructure of as-deposited film can be tailored by the chemical reaction of liquid precursor [89] and process parameters [92]. Electrospray deposition (ESD) can spin-off to other techniques such as electrostatic spray assisted vapor deposition (ESAVD), [37,92] or electrostatic spray pyrolysis (ESP) and the pressurized spray deposition [93]. *C.H. Chen et al.* combined the sol-gel with ESD to fabricate SiO_2-doped TiO_2 film in order to reduce the possibility of cracking after deposition and named it after the process called Electrostatic sol-spray deposition (ESSD) in 1999 [60]. Most recently, the mechanism is launched to electrohydrodynamic (EHD) jetting technology in high resolution printing by using viscous fluid [90].

Electrospray deposition or electrodynamic atomization fabrication method is the economically-versatile technique can generate the deposition rate up to 80-90% without requiring high performance apparatuses [18] . *Choy et al.* suggested that this technique is also simple and flexible to control morphology of as-prepared film [94]. In addition, the method has been considered a non-toxic, environmental-friendly and flexible-to-scale up technique to fabricate film on any size of substrate [91,93,94-97]. Many modes of spray such as cone-jet, multi jet, dripping, oscillating-jet, precession and spindle; can be obtained by modifying process parameters summarized by *A. Rezvanpour et al., C. Ghanshyam et al.* and *A. Jaworek* [88,95,98]. The difference in size and charge of droplet distribution, velocity and spray shape determines the mode of spray [98]. This versatility paves the bright way for electrospray deposition to find the applications in various fields of industries such as solar cell, fuel cell, battery cell, micro- to nano-electronic devices as well as biotechnology applications [88].

Initially, electrospray deposition (ESD) was used to produce thin layers of radioactive material. Recently, it is used for thin film deposition in nanotechnology and nano-scaled electronics application. This technique has a high potential to prepare a wide range of particle sizes and materials from single component of ceramic, polymer to composite [91,93] as well as very low concentration precursor [99]. By accompanying facilities, ESD can be applied to synthesis nanoparticle, encapsulated particle as well as 3-D sample by ESD forming and writing (maskless) processes [88]. The typical processing parameters are applied voltage, deposit distance, flow rate of the liquid, deposition temperature and time and the nozzle diameter [96,98]. Additionally, the precursor properties also have an influence on the quality of the film namely; electrical conductivity, viscosity, relative permittivity, surface tension and density [95]. *A.*

Rezvanpour et al. reported that the droplet size can be mainly controlled by the precursor properties, flow rate and applied voltage [95]. The most typical and stable cone-jet mode has zero hydrostatic pressure inside the liquid [100]. Therefore, the droplet size can be expressed as below [88]:

$$d = f(Q, \rho, \varepsilon_0, \sigma, \gamma) \qquad (6)$$

Where d is diameter of cone jet (m), Q is flow rate (m^3/s), ρ is density of solution (Kg/m^3), σ is conductivity of liquid (S/m), γ is surface tension (N/m), α is constant and ε_0 is permittivity of vacuum (F/m or $A^2s^4kg^{-1}m^{-3}$).

The differences in magnitude of each parameter were previously reported ranging from 0-1/3. However, *C. Ghanshyam et al.* revealed that droplet size and the diameter of a droplet charge were strongly dependent on liquid properties and flow rate as following equations; [98]

$$d_j = \alpha \left(\frac{Q^3 \rho \varepsilon_0}{\pi^4 \sigma \gamma} \right)^{1/6} \qquad (7)$$

Where d_j is diameter of cone jet (m), Q is flow rate (m^3/s), ρ is density of solution (Kg/m^3), σ is conductivity of liquid (S/m), γ is surface tension (N/m), α is constant of 2.9, d_d is diameter of charged droplet (m), ε_0 is permittivity of vacuum (F/m or $A^2s^4kg^{-1}m^{-3}$) and $d_d = 1.89 d_j$.

In the cone-jet mode of fabrication, viscosity of precursor has less impact on droplet size and can be overlooked. However, it is worth noting that the higher viscosity requires higher energy to disintegrate the solution into the droplet, and other modes of spray or morphology can be found [88]. The typical issues of this method are narrow diameter, [101] required an oxidizing-insensitive materials,[102] less uniform of as-deposited film due to electric field fluctuation [90] as well as the altogether effect of each parameters [88].

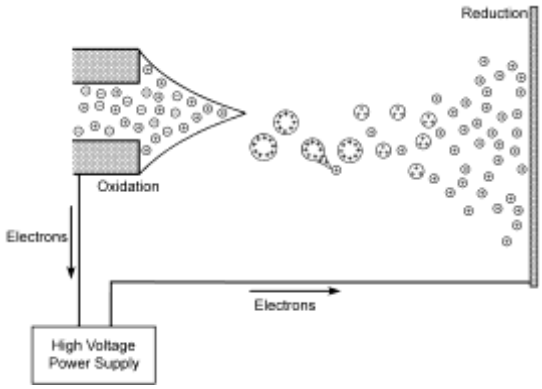

Figure 9. A Schematic of electrospray deposition process [86].

A. Rezvanpour et al. and *C. Ghanshyam et al.* [95,98] studied the effects of each process parameter on the enhancement of quality on as-prepared film. The related mechanisms are: transportation of droplet, evaporation of precursor, spreading-discharge behavior as well as the decomposition on substrate mechanism [98]. Many scholars have investigated the processing parameters affecting the as-deposited film. For example, *Cloupeau et al*. described and explained the different electrospray patterns in terms of the electric potentials, the liquid physical properties, the liquid flow rate and the setup geometry of system. *Fernandez et al*. studied the electric current and the cone-jet droplet size dependence on various setup parameters [18]. *A. Jaworek et al.* studied a stability map accounting for the voltage and the flow rate that contribute an enormous effect to broaden further experiments.

The influence of each process parameter can be described as following:

Applied voltage has a strong influence on the shape of a droplet and a discharge mechanism resulting in a morphology variation. The spherical shape of a droplet can be transformed or elongated into fiber one by increasing electrical voltage [103] and the conical-shaped droplet will alter from single-jet mode to the multiple-jet deposition when applied voltage increases. Moreover, the corona discharge effect, which is dependent on polarity limits using positive voltage to obtain the stable cone jet because positive voltage generates a less disturbing effect than a negative one, can be generated. [101] The droplet starts forming when the critical voltage is reached as following estimation expression [100]:

$$V_{min} \sim \left[\frac{\gamma D}{\varepsilon_0}\right]^{1/2} \quad (8)$$

Where V_{min} is minimum voltage, γ is the surface tension, D is diameter of the nozzle tip and ε_0 is the electric permittivity of the free space.

Macky et al. [86] and other works [104,105] revealed that the factor called "the critical electric field" or the "Taylor limit of field" that induced instability in charged droplets and strongly influenced droplet size or radius, *r*. This relationship was defined in the below equation by *Geoffrey Ingram Taylor et al.* in 1964:

$$E_C^0 = \left[\frac{c}{8\pi^{1/2}}\right] x \left[\frac{2\sigma}{\varepsilon_0 r}\right]^{1/2} \quad (9)$$

Where E_C^0 is the applied electric field, ε_0 is the electric permittivity of the free space, c is the constant value = 1.625 from the previous investigation. [104-106]

In 1994 *Taylor* gave the first explanation and theoretical description of the conical shape at the capillary exit by investigating the hydrostatic balance between electrical and surface tension forces. This cone has been commonly known as the "Taylor cone" [18].

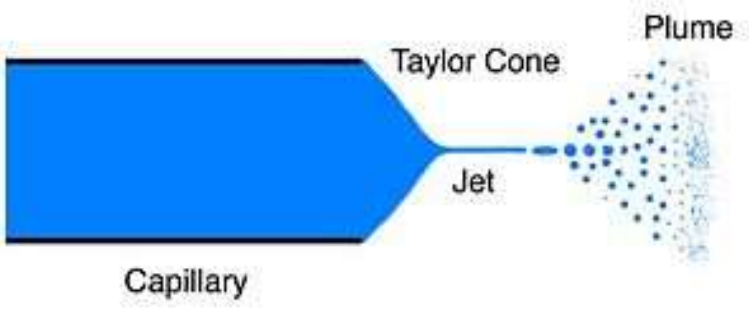

Figure 10. Taylor cone [37].

Apart from kinetic aspect, the applied voltage plays a vital role in droplet production processes in small distances between nozzle and the collector resulting in large and flat droplets with high yield, [91,98,107] whereas the evaporation rate dominates this mechanism at a further distance [98]. Therefore, the greater deposition distance induces to ring, or donut-shaped droplets with high porosity according to a higher protuberance at longer times of flight [107]. In addition, the applied voltage can be employed to regulate the amount of liquid. Consequently, the thickness of as-deposited film increases when the electric field increases. However, too strong of an applied voltage induces secondary finer droplets and turbulence resulting in low quality of as-prepared film [98]. *Ali et al.* revealed the variation of spray modes (dripping to multi jet mode) at different applied voltage and flow rate in ZnO_2 film for memory cell application [97].

Deposition distance was studied in terms of time in flight by *C. Ghanshyam et al*. They found that less time of flight can be observed in a strong electric field which directly affects the decomposition or evaporation rate of a precursor on heated substrate because droplet velocity increases [98]. *Fukuda et al.* suggested that the charge per volume decreased with distance increased [101]. The relationship between time of flight and other parameters can be estimated by the following equation [98]:

$$t \approx \frac{3\pi d\eta L}{qE} \qquad (10)$$

Where t is time of flight(s),d is droplet diameter (m), η is kinematic viscosity (m^2/s), L is distance between nozzle and substrate (m), q is charge (C) and E is applied voltage (V/m).

Flow rate *A.Jaworek et al.* reported that the stable cone-jet mode can be reached at minimum flow rate according to Barrero and Loscertales approximation as below [88]:

$$Q_{min} \approx \frac{\sigma\varepsilon_0\varepsilon_r}{\rho\gamma} \qquad (11)$$

Where Q_{min} is minimal flow rate, $\sigma, \varepsilon_0, \varepsilon_r$ are liquid conductivity, permittivity of vacuum and relative permittivity respectively. ρ is density of liquid and γ is surface tension.

Zargham et.al studied the effect of flow rate on Nylon 6 nanofibers in the electrospinning process. They found that the electric force had a strong influence on the stability of Taylor's cone as well as morphology of as-deposited fiber when a slow flow rate was applied. Whereas the gravitational force had an effect when a high flow rate was employed due to droplet mass increased resulting in an instable jet and an incomplete evaporation process occurred [108]. *Chen et.al* studied the effect on the flow rate on morphology of as-deposited $LiMn_2O_4$film. They showed the correlation between flow rate and the pore size (d) of reticulated structures, which agreed with scaling law as following:

$$d \propto (Q/K)^{1/3} \qquad (12)$$

Where d is pore size, Q is flow rate and K *is conductivity of solution*

Deposition temperature has a strong effect on the texture of the film. The roughness and morphology of as-sprayed film are varied by evaporation or boiling processes of precursor during deposition. Too high deposition temperature leads to collecting small and dried droplets on the surface resulting in rough film [93] and grain structure [98] because the number of discrete or scatter particles increase [92,109]. However, too low deposition temperature allows the precursor to be boiled on substrate resulting in a non-homogeneous texture because of an incomplete evaporation process. [110] In contrast, a dense surface can be obtained from low temperatures because precursors with slow evaporation rates keeps the liquid phase to stay connected after deposition. In order to get the crack-free film, the deposition temperature should not be higher than 50°C of the boiling temperature of the precursor determined by DTA [92,93]. Therefore, the deposition temperature and evaporation of precursor needs to be simultaneously optimized. In addition, the temperature range should be varied in a narrow range to maintain a high quality of the film [111]. *Jing Du et al.* revealed that increasing deposition temperature can improve a crystallinity of TiO_2 film for gas sensor applications [94].

Suspension properties are required to consider, as well as process parameters, because they play a mutually crucial role in raising difficulties in practice [88]. All parameters affect the charged droplet behavior in electrospray deposition with respect to the theoretical model of charge transport [112]. *A. M. Gañán-Calvo et al.* derived the scaling laws by investigating current, charge and the size of a droplet in two ranges of viscosity and conductivity of liquid precursor.

They concluded that the conductive and viscous solution was difficult to form into a cone-jet droplet because tangenial stress can effectively diffuse across the jet radius when induced by an electrical field. Whereas the low viscosity with conductive solution generates high velocity of droplet because the surface boundary layer is much smaller than a jet radius resulting in a cone jet mode of deposition [112].

In order to maintain a total charge per unit volume in accordance with Rayleigh limit, [100] the suspension properties: conductivity, surface tension and density are required to consider in the ESD process. *Lord Rayleigh (1882)* [18,113] estimated the maximum charge that liquid could carry by predicting the natural quadrupolar oscillation of a droplet in a field-free environment. The charged droplet became unstable when the charge was out of this limit as a result of the Coulombic fission or "Rayleigh charge limit" [86]. The charge density at this limit can be defined in the equation below [101].

$$q_R = 2\pi(16\gamma\varepsilon_0 r^3)^{1/2} \qquad (13)$$

Where γ, ε_0 and r are liquid surface tension (N/m), permittivity of vacuum (F/m or $A^2s^4kg^{-1}m^{-3}$) and droplet radius (m), respectively. q_R is Rayleigh limit charge (Coulomb).

At $q \geq q_R$, the liquid would be rejected into fine droplet jets. Therefore, the relationship between droplet size and Rayleigh charge limit ($\frac{q_R}{m}$) can be described as following the equation by assuming that the droplet shape is spherical;

$$\frac{q_R}{m} = \frac{q_R}{\frac{4}{3}\pi r^3 \rho} = \frac{6}{\rho}\left[\frac{\gamma\varepsilon_0}{r^3}\right]^{1/2} \qquad (14)$$

Where ρ is density of solution (kg/m^3), γ is surface tension (N/m), r is droplet radius (m), q_R is Rayleigh charge limit (Coulomb), m is mass or droplet (kg) and ε_0 is permittivity of vacuum (F/m or $A^2s^4kg^{-1}m^{-3}$).

Additionally, the conductivity of the suspension also has an effect on the charged droplet size as in the following equation [100]:

$$d = (^{Q\varepsilon}/_{\mathrm{K}})^{1/3} \qquad (15)$$

Where Q is flow rate, ε *is permittivity of solution and* K *is conductivity of solution*

Yonghee Kim et al. reported the effect conductivity of a solution by varying DMSO content in PEDOT:PSS precursor for transparent electrodes. As the conductivity increased, the droplet size dramatically reduced and improved homogeneity of as-prepared film from pancake-boundary droplets to finer ones [102] because charge density per volume changed in accordance with the above equation. In the cone-jet mode of spray, *Fukuda et al.* [101] reported that the narrowly-dispersed size distribution and uniformity were required in order to avoid defects and cracks on as-deposited film. A small droplet size (<1 micron) provides a smooth surface of thin film in multilayer applications because a high droplet charge per volume was achieved. The droplet diameter (d) in cone-jet mode can be expressed as the following [101]:

$$d \propto \frac{Q\varepsilon_0 \rho}{\gamma K} \qquad (16)$$

Where $Q, \varepsilon_0, \rho, \gamma$ *and K are liquid flow rate, dielectric constant of vacuum, density, surface tension and conductivity respectively.*

However, previous literatures also reported the relationships between droplet size and conductivity of precursor for cone-jet mode of spraying as following [114]:

a. *de la Mola and Loscertales*

$$d = \alpha\left(\frac{Q\varepsilon_0\varepsilon_r}{\gamma_l}\right)^{1/3} \qquad (17)$$

b. *Hartman et.al*

$$d = \alpha\left(\frac{Q^3\varepsilon_0\varepsilon_r}{\sigma_l\gamma_l}\right)^{1/6} \qquad (18)$$

c. *Gañán-Calvo*

$$d = \alpha \left(\frac{Q^3 \varepsilon_0 \rho_l}{\pi^4 \sigma_l \gamma_l}\right)^{1/6} \qquad (19)$$

Where α = 2.9, Q is liquid flow rate, ε_0 and ε_r are dielectric constant of vacuum and liquid, ρ is density, γ and σ are surface tension and conductivity of liquid respectively

These three expressions were proposed in different deposition configurations. For *de la Mola and Loscertale,* Equation 17 is desired for a large conductivity precursor, which is a jet diameter much smaller than the capillary tube. In contrast, equation 18 by *Hartman et.al* is required no secondary droplet jet to be observed or taken into account. However, *Gañán-Calvo* proposed Equation 19 by taking overall process parameters into consideration.

In addition, *Fukuda et al.* [101] also studied the effect of high dielectric constant, molecular weight, surface tension and density of non-polar solvent toward charge density per volume. They found that the large diameter of the jet cone was generated by coulomb repulsive force in a perpendicular direction of the capillary plane. A higher charge density per volume by using liquid precursor with large dielectric constant provided the high quality of coating.

Owing to the various modes of spray, electrospray deposition processes can be applied in many fields of application, functionalities and morphologies. All process parameters and suspension properties have a straightforward effect on a microstructure of as-deposited film. The typical microstructure of thin film fabricated by ESD can be divided into two main groups: dense structure and porous one.

Firstly, dense structure can be achieved when the process is well defined by the accumulation of mono-sized distribution of droplet. The longer deposition time of small particle with suitable evaporation rate generates a highly-dense film [92]. *Ali et al.* revealed the variation of flow rate and applied voltage toward a mode of spray in ZrO_2 film for memory cell application. [97] Crack-free and dense structure were generated by a small amount of residual organics when film was deposited at high temperature [60]. As-prepared film with dense structure is desired for many applications, such as transparent conductive film for display panels, windows for solar cell

and so on.

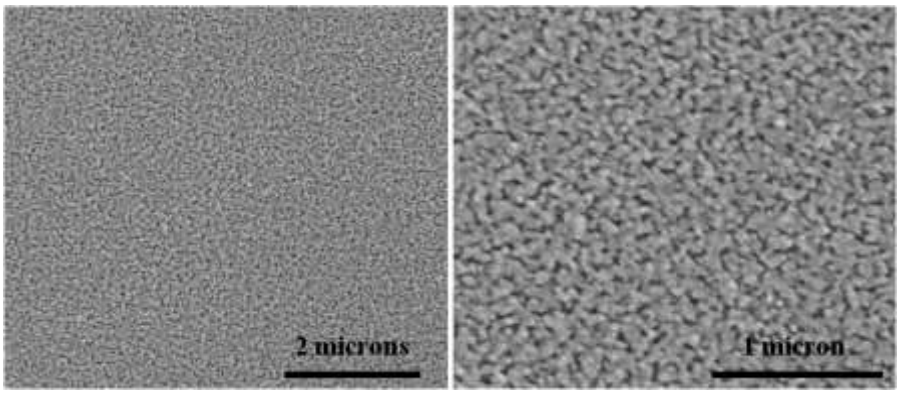

Figure 11. The SEM image of dense structure of ZnO film on glass substrate.

Secondly, porous structure have been widely investigated in many applications such as catalysis, fuel cell and gas sensor. Such a function has been favorably prepared by ESD process because porous structures with narrow pore size distribution can be achieved [110,115]. The typical porous structure is a reticulated or 3D-cross linked structure, so this structure basically has high mechanical strength with chemical stability reported on $LiCoO_2$ film by *Chen, C. H et al* [110]. *I Uematsu et al.* that the reticulated structure of protein film can be obtained by ESD. The smaller pore size was achieved at a high concentration of protein [87]. Another type of porous structure was investigated by *Jing Du et al.* on $CrTiO_3$ (CTO) for gas sensor application. They revealed the morphology evolution of the film at different concentrations and effects of additives toward sensitivity [96]. *Princivalle, A et al.* reported that the simultaneous boiling behavior leads reticulated or porous structures to form [109]. However, *Chen et al.* suggested that the reticulated structure can be altered to dense film when flow rate decreased because the diameter of a droplet was reduced which was in agreement with the proportional flow rate to a droplet diameter at a magnitude of 1/3 as mentioned before [115]. On the other hand, *Nguyen, T. and Djurado, E.* suggested that the dense sturcture of ZrO_2 film can be transformed to porous or fraclike structure by increasing the electric field because of an internal stress inceased, [116] especially at a high deposit temperature, the structure with high porosity is subjected to form because Coulombic force dominates the structural forming process [110].

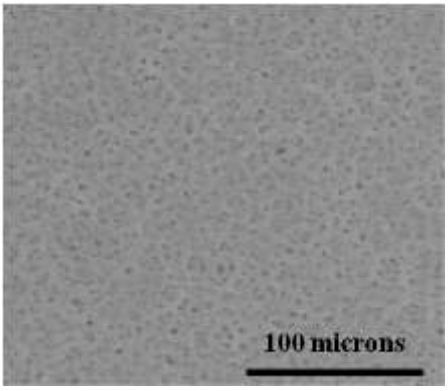

Figure 12. The SEM image of reticulated structure of 3%Li-doped ZnO on glass.

F. Optoelectronic properties

A. Optical properties

The transparency of the materials is the key to consider in any application especially for display panel applications. Most ceramic materials are dielectric, opaque or translucent in visible range because the scattering of light resulting from discontinuity in reflective index, grain boundary, porosity and optical anisotropic properties of material. Therefore, fully dense and single phases are required for ceramic in optical application. [33]

The main obstacle to hide the ceramic polycrystalline reaching high transparency is the scattering process as shown in Fig.3. The magnitude of the scattering event can be expressed by Rayleigh's equation [33]:

$$\frac{I_\theta}{I_0} \propto \frac{1+\cos^2\theta}{x^2} r^2 \left(\frac{r}{\lambda}\right)^4 \left(\frac{n_p - n_m}{n_m}\right)^2 \qquad (20)$$

Where I_θ is light scaterred through and angle θ by a dispersion of particle radius r and reflevctive index n_p in the matrix of reflective index n_m by intensity of incident light I_0 at distance x and λ is the wavelength of the scattered light ($r<\lambda$)

If the particle size is smaller that λ, the scattering event will have less influence on the transmittance of incident light. Consequently, the high transparency will be obtained. However,

in polycrystalline materials, the scattered event can be generated from birefringence of the two phases locating close to each other resulting in a greater difference of $n_p - n_m$ according to the aforementioned equation.

In addition, the minimum required energy to excite an electron from valence band to conduction band called optical band-gaps energy is another significant optical property. There are two band-gap shifting mechanisms related to holes in valence bands and the electron in the conduction band: band-gap widening (Burstein-Moss effect) and band-gap narrowing (BGN) [117]. The previous studies by *Joeng et al.* and *V. Srikant et al.* revealed that the lattice stress in the growth process caused an optical band-gaps shifting mechanism. Three possibilities to generate stress in the heat treatment process consist of a coefficient of thermal expansion (CTE) mismatched, a lattice constant mismatched and an imperfection of thin film during deposition at interface region [118,119].

From an electronic point of view, the PL spectra shifting suggested that the electronic structure had changed due to lattice strain. However, *R. Ghosh et al* observed the opposite tendency on the effect of substrate on strain. By deposition the ZnO film on different types of substrate, the lattice strain induced by mismatching between film and substrate. The compressive condition band-gaps widening due to a repulsive force between O p^2 and Zn s^4 increased and vice versa [32].

Additionally, the doping mechanism can also tailor electronic structures in ionic materials. The many-body interaction causes self-energy shifting when a dopant is introduced. The displacement of charge induces polarization resulting in a charge carrier movement in host lattice. The effective charge carriers are attracted and repulsed by opposite and similar charges respectively to generate a charge cloud particle called polaron. The self-energy shift when dopant is introduced can be quantified by the following expression: [117]

$$\sum_p^{ion,j} = \frac{N}{\hbar\Omega} \sum_q' \left[\frac{\nu\,(q)}{\varepsilon(o)\varepsilon(q,o)}\right]^2 G_b^j\,(p+q, e_p^j/\hbar) \qquad (21)$$

Where j stands for electron or hole in conduction or valence bands respectively, N is ion density, $\hbar = \frac{h}{2\pi}$ *,*Ω *is total volume of the system,* $\nu\,(q)$ *is the Fouirer transform of the Coulumb*

potential, $\varepsilon(o)$ *and* $\varepsilon(q,o)$*are dielectric constant at low frequency and* G_b^j *is the Green's function as a function of* $p+q$ *and* $e_p^j/\hbar$.

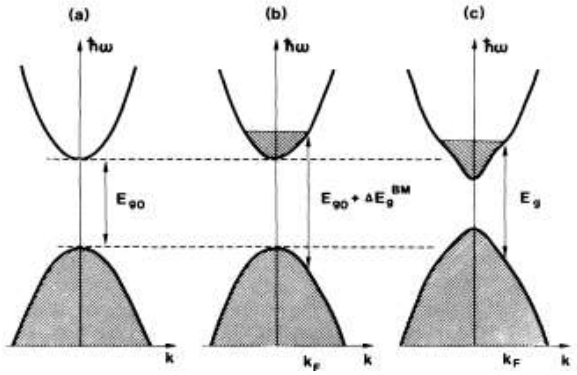

Figure 13. A Schematic band structures of undoped structure, E_{g0} (a), Burstein-Moss effect, $E_{g+}\Delta E_g^{BM}$ (b) and Band-gaps narrowing, E_g (c) [117].

Consequently, the optical band-gaps can be defined by below equation [117];

$$E_g = E_{g0} - E_{pol}^e - E_{pol}^h + \Delta E_g^{BM} + Re(\sum_{K_F}^{int,e} + \sum_{K_F}^{ion,e} + \sum_{K_F}^{int,h} + \sum_{K_F}^{ion,h}) \qquad (22)$$

Where $E_{pol}^{e(h)}$ is polarization energy of electron (e) or hole (h) and K_F is Fermi wave factor.

The three first terms represent the undoped crystal and the four self-energy terms are the interaction effect of dopant toward the virgin lattice without considering the impurity scattering effect. The band-gaps widening called "Burstein-Moss effect" or "band filling effect" [120,121] is explained by the phenomenon of excess electrons blocked at lower (valence) bands in accordance with the Pauli exclusive principle. Therefore, they doubly occupy the effective charge carrier that is prohibited [117]. In contrast, the band-gap narrowing effect can be the result of strain and imperfection in the doping process. The Coulombic repulsion between electron-electron or electron-impurity is generated when the defect is introduced and scattered [122] resulting in the lower energy of electron or hole. In addition, the electron density tends to relax

around impurity. Both mechanisms distort band structure and move a conduction band shift downward [117].

B. Electrical properties

Conductive materials have unbound charge carriers that can freely move when an electric field is applied. Charge carriers move in the opposite polarity to create the electric current. In solid material, defects and lattice vibration can also facilitate the carrier drift. The electrical conductivity (σ) is defined by the type and number of charge carriers as well as mobility according to the following expression [37]:

$$\sigma = \rho e \mu_h - n(-e)\mu_e = \rho e \mu_h + n e \mu_e \qquad (23)$$

Where ρ is the number density of holes in m^{-3} , n is the number density of electrons in m^{-3}, $e=1.602\times10^{-19}C$ is the magnitude of the charge of the electron, μ_h is the hole mobility in $m^2s^{-1}V^{-1}$ and μ_e is the electron mobility in $m^2s^{-1}V^{-1}$

Hall effect is the phenomenon that moving charge by Lorentz force inducing voltage called Hall voltage (V_H) in perpendicular direction of magnetic field and Current shown in Fig. 14 [123]. The dominant carriers (electron or hole) in semiconductor can be defined by sign of Hall voltage (V_H), the magnitude of (V_H) and carrier concentration [37].

Figure 14. Hall effect schematic figure.

The resistivity and conductivity are related with respect to following equation: [124]

$$\rho = \frac{V}{I} = \frac{1}{qn\mu_H} \qquad (24)$$

Where ρ is resistivity (Ω-cm), σ is conductivity (S), V is the measured voltage, I is current source (A), q is effective charge, n is number of charge carrier and μ_H is Hall mobility.

Hall mobility of charge carrier also plays a key role on conductivity which is affected by three factors expressed in equation below: [124]

$$\frac{1}{\mu_H} = \frac{1}{\mu_i} + \frac{1}{\mu_l} + \frac{1}{\mu_g} \qquad (25)$$

Where μ_i is mobility of ionized impurity scattering, μ_l is lattice vibration scattering and μ_g is grain boundary scattering.

STATISTICAL STUDIES OF PROCESS PARAMETERS OF ELECTROSPRAY DEPOSITION FOR THIN FILM PREPARATION

A. Abstract

Electrospray deposition (ESD) has been known as an economically-versatile thin film fabrication process in ambient. ESD shows a potential to synthesize various materials in the form of porous and dense thin films as well as nanofibers, which is highly favorable for functional oxides. There are many crucial process parameters which play crucial roles in determining the quality of as-prepared thin film and morphology namely, chemical/physical properties of precursor, applied voltage, deposition temperature, flow rate, deposit distance, and time. To begin with, a content of deionized water in ZnO-precursor was varied in order to optimize the water content to a workable range of the electric field. Secondly, a regression plot revealed three levels of each ESD process parameter towards the quality of the as-prepared film in terms of the % film coverage area. Lastly, a statistical approach called factorial design of experiment was adopted to determine the significance (p-value <0.05) of ESD process parameters towards % film coverage area at R^2 of 87.61%.

B. Introduction

Electrospray deposition (ESD) has been known as an economically-versatile thin film fabrication process in ambient. This process is related to the interaction between liquid and electrical field, and has been discovered for over one hundred years. In addition, ESD shows potential to be applied in large-scaled applications and to synthesize various materials in the form of porous/dense thin films, nanofibers [18]. Owing to a simple set-up without a sophisticated apparatus and the versatility of ESD, one would say that this method possess a high potential to be implemented in myriad industries for with low cost of production [18]. The basic concept lies in the fact that a high voltage is applied to generate an electric field between nozzle and heated substrate in order to disintegrate liquid precursor and form conical shape of droplet mist (Taylor cone) by overcoming a surface tension and then splitting into the droplet [18,113]. All finely-charged

droplets are collected onto the heated substrate layer-by-layer accommodating the electric field [86,87,89]. The morphology and microstructure of as-deposited film can be tailored by the chemical reaction of liquid precursor [89] and process parameters [92]. In addition, the stability of the ESD process is strongly dependent on Rayleigh Limit, which is directly proportional to dielectric properties and surface tension of liquid precursor. Typically, ethanol-based precursor has been used in electrospray deposition. The low viscosity and electrical conductivity allowed one to deposit at low applied voltage. However, a low surface tension of ethanol leads a charge per unit volume or Rayleigh limit (q_R) gets smaller. In addition, ethanol has low molecular weight and a boiling point, which is easy to evaporate, and induces a grain-like droplet to be deposited. Consequently, the ESD process becomes less flexible, unstable and the low quality of as-prepared film [95101]. In the thin film fabrication process, the cone-jet mode of spray can be produce a high film quality due to the highly-uniform droplet size with narrow size distribution that can be achieved [101]. In addition, a cone-jet mode of spray can produce crack-free surfaces in favorable to transparent conductive applications. Therefore, stable ESD processes with a larger Rayleigh limit are preferable in order to increase process stability. In this work, diethylene glycol was chosen to study due to a high surface tension that is twice ethanol, but the electrical conductivity is very low. Therefore, the Rayleigh limit (q_R) will increase with gradual increases of low critical applied voltage [104-106]. Moreover, the higher molecular weight and boiling point lead to deposit the film at high temperatures without degrading film quality. However, the viscosity is high and dielectric constant is very low which raises difficulties in obtaining a cone-jet mode of spray and requires higher energy to form droplets [88,112]. Therefore, deionized water, which has a high dielectric constant and surface tension, can be added to increase the Rayleigh limit by increasing dielectric constant of precursor with respect to rule of mixture. Consequently, the ESD process will become more stable and flexible. However, an increase of dielectric constant will increase higher electric fields to carry charged droplet. Therefore, the deionized water content should be optimized.

Additionally, other process parameters of electrospray deposition namely, applied voltage, deposition temperature, flow rate, deposit distance, and deposit time also play a crucial role in determining quality of as-deposited film which can be obtained by observing % film coverage area on substrate. The effect of each process parameter needs to be described comprehensively in term of evaporation-decomposition and kinetic aspects. For example, an

increase of applied voltage accelerated the charge droplet which allows droplet to deposit without complete organics decomposition. Moreover, there are so many process parameters or factors which are strongly influenced the quality of the film. Therefore, statistical methodology would benefit to analyze and determine the significance of each process parameter by using a factorial design of experiment. Factorial design of the experiment provides comprehensive results in both main and interaction effects of each process parameter. It is suitable for a multi-factor system and can reduce a number of experiment [125].

C. Experimental procedures

Experimental procedures in this chapter were divided into two parts as following:

1. Maximize water content to form stable taylor's cone jet

Diethylene glycol (BioUltra$\geq$ 99.0% $C_4H_{10}O_3$, Sigma-Aldrich) was mixed with deionized water to determine the maximum water content that stable Taylor's cone was formed. Deionized water content of 10%, 25% and 40% v/v were mixed with DEG solvent and used to prepare solution-based precursor for 0.10 M of Zinc acetate dehydrate ($Zn(CH_3COO)_2.2H_2O$, Fisher Scientific). All prepared precursor were deposited by using the same process parameters on as-cleaned glass substrate which were 0.08 mL/hr of flow rate, 17.50 kV of applied voltage, deposit distance at 15.0 cm and deposition temperature at 368$\pm$5 K for 120 minutes. As-deposited samples were assigned to anneal at 773 K [43,126] for 5 hr of dwelling time at 10 K/min of the heating rate in order to decompose organic matter, to form ZnO Wurtzite structure, to reduce tensile stress and to eliminate defect without dissipation [126-128] .

Microstructure was examined by using ESEM (FEI Quanta 200F, Hillsboro, OR). D2 Phaser (Bruker-AXS, Madison, WI) by equipped Cu radiation (CuK_α, λ = 1.545 Å) was performed to examine the crystal structure. Scan pattern data were collected between 2θ ranging from 20^o to 70^o and with step lengths of 0.05 and a counting time of 1 sec/step in order to identify phase.

2. Optimize process parameters and determine the significant factors

The most stable DEG: DI water was conducted to vary other process parameters namely, deposition temperature, applied voltage, deposition distance, deposition time and flow rate at three consecutive different levels. D2 Phaser (Bruker-AXS, Madison, WI) by equipped Cu

radiation (CuK_{α}, λ = 1.545 Å) was performed to examine the crystal structure. Scan pattern data were collected between 2θ ranging from 20° to 70° and with step lengths of 0.05 and a counting time of 1 sec/step in order to identify phase. Microstructure was examined by using ESEM (FEI Quanta 200F, Hillsboro, OR).

First, SEM micrographs were converted to a binary-mode figure by maintaining the image similarity as close as the original SEM. Subsequently, *ImageJ*® software package was performed to quantify the % film coverage area from the contrasted film area. Next, the statistic package called *Minitab*® was carried out to determine significant factors of aforementioned process parameters to the film's quality by factorial design of experiment function. Lastly, effects of individual process parameter on % film coverage area were reported by regression plots.

D. Result and discussion

1. Maximize water content to form stable taylor's cone jet

Table III. Properties of Precursor at Three Different Deionized Water Content [129]

Diethylene glycol: deionized water (DEG:DI)	**6 : 4**	**7.5 : 2.5**	**9 : 1**
Surface tension (milliN/m)	54.00	52.50	50.00
Electrical conductivity (μS/cm) at 20-25°C	4.00	1.75	0.50
Viscosity (cP) at 10°C	10.50	25.00	40.00
Boiling point (°C)	110.00	115.00	135.00

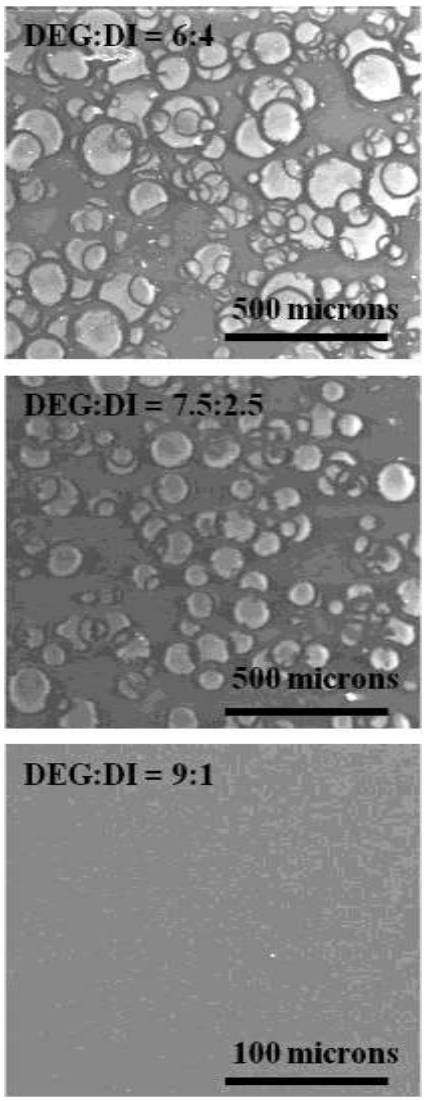

Figure 15. SEM images of as-annealed 3% Li-doped ZnO at 773 K for 5 hr with different ratio of Diethylene Glycol to deionized water of 0.10 M Zinc acetate dihydrate on glass substrate. Other process parameters were fixed namely, applied voltage of 17.5 kV, deposition temperature of 130±5 ºC, flow rate of 0.08 mL/hr, deposit distance of 15 cm and 2 hr deposit time.

SEM micrographs in Fig.15 indicate that fine droplets were not formed at DEG:DI water ratios of 6:4 and 7.5:2.5 by employing assigned process parameters shown in Fig 15. The droplet size and diameter of droplet in cone-jet mode could not show correlation with respect to

Equation 7. due to applied voltage had not yet been reached and droplets were not formed in all precursors. However, it can be implied that at this assigned deposition condition, the maximum deionized water content to generate a stable cone- jet mode to deposit fine droplets was 10%. No island-mode droplet was observed in SEM micrographs on film which was prepared by using DEG:DI water ratio of 9:1. This finding indicated that an assigned electric field had overcame a tangenial stress to form a stable cone-jet mode of spray [112]. Consequently, a well-distributed and high quality film can be obtained.

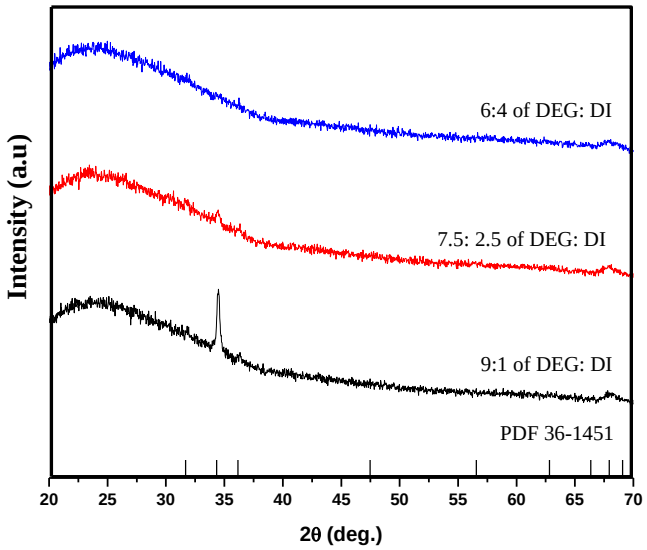

Figure 16. XRD patterns of as-annealed 3% Li-doped ZnO at 773 K for 5hr. with different ratio of Diethylene glycol to deionized water on glass substrate.

X-ray diffraction patterns shown in Fig.16 suggests that most pronounced peak was found in 9:1 v/v of Diethylene glycol (DEG) to deionized water (DI) precursor. This film belonged to $P6_3mc$ space group of Hexagonal Wurtzite structure which agreed with PDF# 36-1451. This finding indicated that film was successfully deposited on glass substrate. On the other hand, the other two DEG:deionized water ratios showed less pronounced peaks: the more water content, the less pronounced peak intensity. These suggested that films were not successfully deposited on glass substrates as DI water content was higher than 10%. Regarding to SEM images in Fig.15., these films showed island-mode distribution which indicated that droplets were not formed due to the applied voltage was not reach the threshold yet. As DI water content increased, a surface tension as well as an electrical conductivity of precursor increased as shown

in Table III. Therefore, higher electric field was required in order to overcome the tangenial stress and form the droplet in accordance with Equation 8. Therefore, droplet was rarely deposited on substrate. Consequently, these films which were deposited by using high DI water content caused difficulties in detecting the phase by using XRD [100].

2. Optimize process parameters and determine significant factors.

Table IV. Designated Conditions for Studying Effects of ESD Process Parameters on %Film Coverage Area

Process parameter	**Level 1**	**Level 2**	**Level 3**
Deposition temperature (˚C)	90±5	110±5	130±5
Applied voltage (kV)	15.0	17.5	20.0
Flow rate (mL/hr)	0.04	0.06	0.12
Deposit distance (cm)	10.0	12.5	15.0
Deposit time (hr)	0.5	1.0	1.5

Table IV exhibits designated conditions to study effects of each process parameters on % film coverage area of as-annealed film namely; deposition temperature, applied voltage, flow rate and deposit distance by using 0.10 M of ZnO with 9:1 v/v of Diethylene glycol (DEG) to deionized water (DI) precursor. Three consecutive different levels of each process parameter were performed to deposit films by electrospray deposition. Subsequently, SEM images were converted into a binary mode by *ImageJ*® software package. Subsequently, % film coverage area of the film was quantified to determine degree of covering by film. Consequently, effects of each ESD process parameter on % film coverage area were demonstrated by regression plot and described as following;

Effect of applied voltage

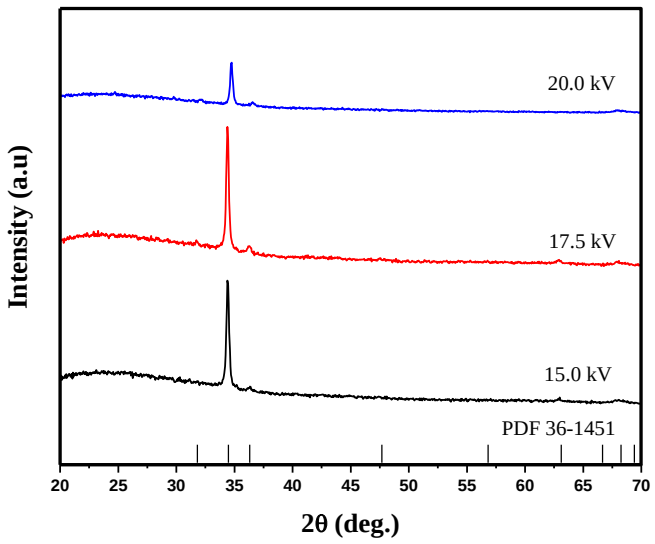

Figure 17. XRD pattern of as-annealed ZnO at 773 K for 5 hr with different applied voltage. Other process parameters were fixed namely, deposition temperature of 105±5 ºC, flow rate of 0.12 mL/hr, deposit distance of 10 cm and 1 hr deposit time.

X-ray diffraction pattern of as-annealed ZnO films with different applied voltage as shown in Fig. 17. All films showed that their structures belonged to hexagonal Wurtzite structure in $P6_3mc$ space group (PDF# 36-1451) with preferred orientation at (0 0 2). These results indicated that workable applied voltage range for 9:1 v/v of DEG to DI water of precursor fell into this range. All films were homogeneous and uniform as seen in Fig.18 which indicated that the threshold applied voltage was reached in this study range.

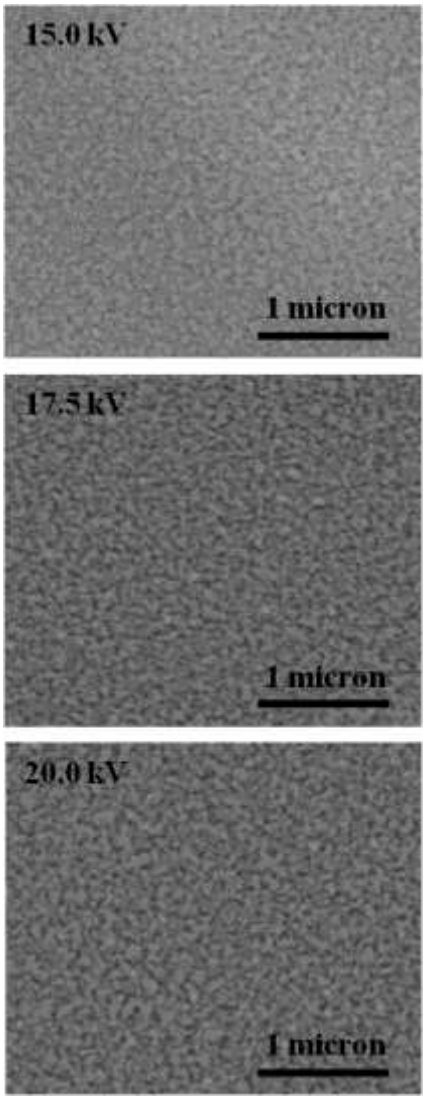

Figure 18. SEM images of as-annealed ZnO with different applied voltage.

SEMs images in Fig.18 suggested that as applied voltage increased, a higher quality with denser surface was found as shown. When applied electric field increased, precursors have a higher energy to disintegrate and form smaller droplets compared to low applied voltage condition with respect to Equation 9 [98]. Consequently, denser and more consolidated microstructure was likely to form in high voltage condition when film was annealed.

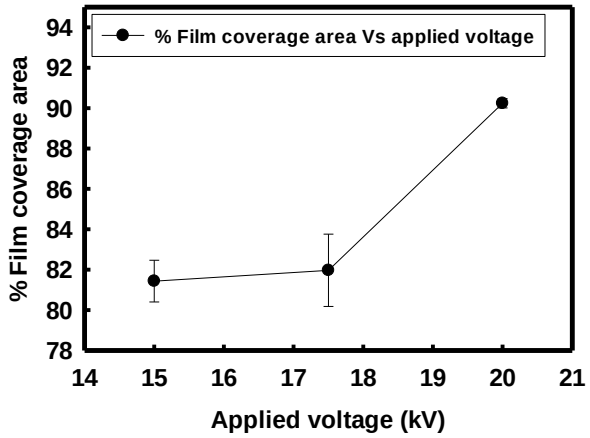

Figure 19. A regression plot of an applied voltage effect on % film coverage area.

This regression plot between applied voltage (kV) and % film coverage area suggests that film area slightly increased when applied voltage increased from 15 to 17.5 kV. Moreover, % film coverage area drastically increased at 20 kV of applied voltage because of two reasons. Firstly, small droplets had been collected and formed consolidated surface as previously described. Another one was that applied voltage accelerated charge droplet velocity so, organic matter in precursor was incompletely decomposed and facilitated droplet to stay connected to each other. As a result, denser microstructure with high % film coverage area was achieved at high voltage.

Effect of deposition temperature

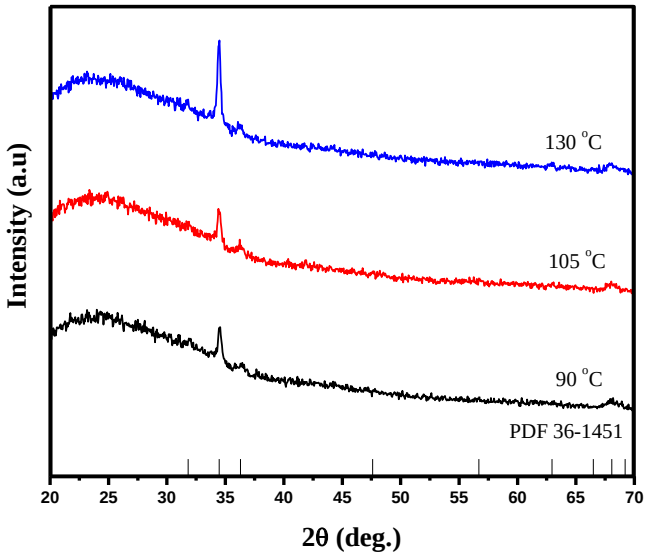

Figure 20. XRD pattern of as-annealed ZnO at 773 K for 5 hr with different deposition temperature. Other process parameters were fixed namely, applied voltage of 20 kV, flow rate of 0.06 mL/hr, deposit distance of 15 cm and 1 hr deposit time.

X-ray diffraction pattern of as-annealed ZnO films with different substrate temperature as shown in Fig.20. All films showed that their structures belonged to Hexagonal Wurtzite structure in $P6_3mc$ space group (PDF# 36-1451). As deposition temperature was higher than 100 °C, preferred orientation was observed at (0 0 2) which is the lowest surface energy and is diffracted at 2theta of 34.34°**.** Consequently, the film's crystallinity was improved which showed agreement with previously reported by *Jing Du et.al* [96].

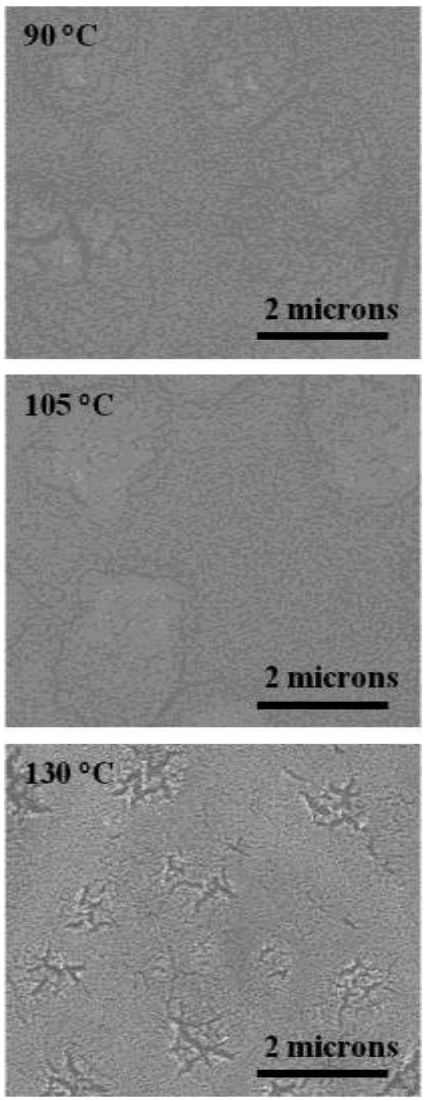

Figure 21. SEM images of as-annealed ZnO with different deposition temperature.

However, SEM images in Fig.21 suggests that the high quality films can be obtained at low temperature (90 °C and 105 °C) which were below the evaporation temperature of precursor about 30-50°C (A 9:1 DEG to deionized water solution has a boiling point of 135 °C as shown in table III [129]). At low temperature, organic matters in precursor evaporated slowly compared to a high temperature. This residual of organic matter kept the liquid phase connected after deposition resulting in high quality films was achieved [102,104]. In contrast, at 130 °C of deposition temperature, small grains with noticeable cracks were observed due to the longer time of flight which allowed the solvent to evaporate and decompose. As a result, small-dried and

grain-like droplets were collected on glass substrate [93]. In addition, organics was burnt out and boiled during process that led loose film was formed after annealing. Consequently, the inhomogeneous surface with lower film quality was observed at high deposition temperature.

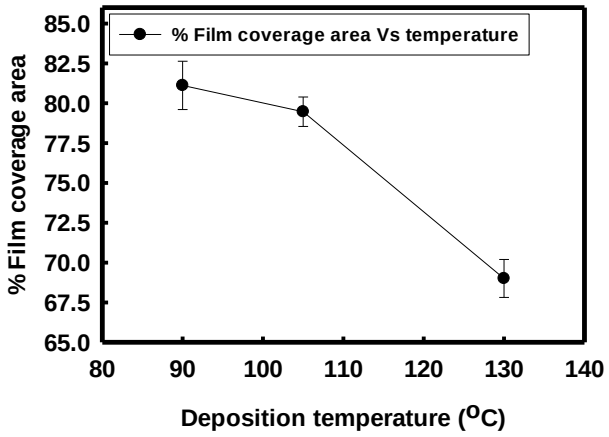

Figure 22. A regression plot of effect of deposition temperature on % film coverage area.

A regression plot in Fig.22 indicated that the % film coverage area slightly decreased when deposition temperature increased from 90 to 105 °C at below boiling point of precursor. However, a considerable amount of organic matter in precursor was burnt out when deposit temperature was close to boiling point of precursor. Consequently, % film coverage area abruptly decreased at deposit temperature of 130 °C.

Effect of flow rate

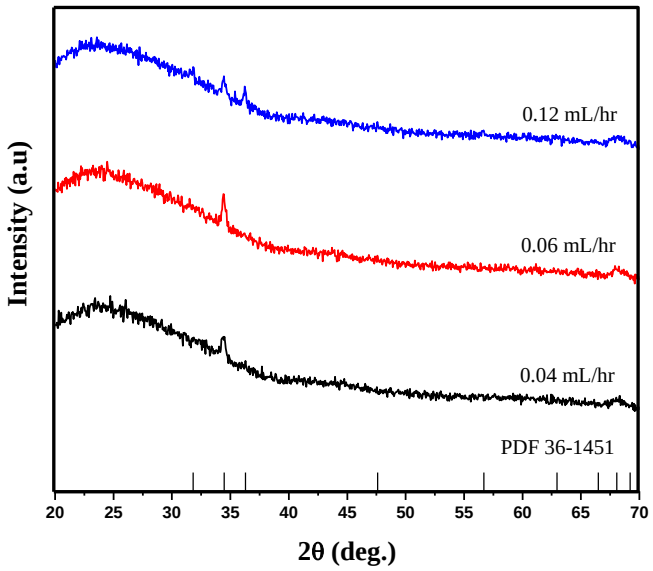

Figure 23. XRD pattern of as-annealed ZnO at 773 K for 5hr with different flow rate. Other process parameters were fixed namely, deposition temperature of 105±5 ºC, applied voltage of 20 kV, deposit distance of 10 cm and 1 hr deposit time.

X-ray diffraction patterns of as-annealed ZnO film with different flow rate of deposition are shown in Fig. 23. All films showed that their structures belonged to Wurtzite structure in $P6_3mc$ space group (PDF# 36-1451). The better crystallinity without preferred orientation was observed as deposition flow rate increased up to 0.12 mL/hr. This was because the greater amount of liquid precursor that is ZnO source was deposited. As a result, thicker film layer can be obtained at high flow rate so, three pronounced diffraction of prominent peaks at which ~ 31-36 ° of 2theta were found flow rate of 0.12 mL/hr.

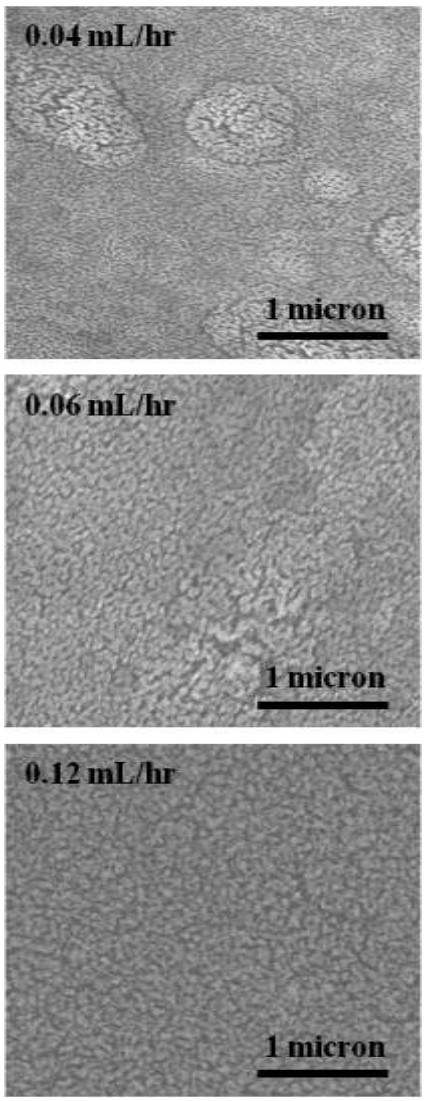

Figure 24. SEM images of as-annealed ZnO with different flow rate.

In addition, SEM images in Fig.24 shows that denser as-annealed films were obtained at the highest flow rate. Due to a larger amount of the organic matter increased with flow rate of precursor, high organics matter was deposited in deposition process. This organic matter led as-deposit droplets to stay connected which enhanced film density. As a result, denser and higher quality films can be observed as deposit flow rate increased. In contrast, grain-like and dried droplets were found in flow rate of 0.04-0.06mL/hr. Due to large portion of organic matter in precursor was evaporated during deposition process, looser films and noticeably micro cracks

were observed at 0.04-0.06 mL/hr of flow rat. As a result, low quality of surface with low degree of film coverage was observed.

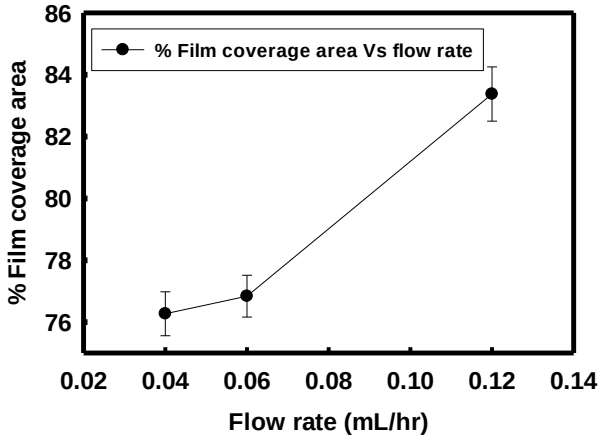

Figure 25. A regression plot of effect of flow rate on % film coverage area.

The monotonous tendency of % film coverage area as a function of flow rate is demonstrated in Fig.25. According to Equation 11, droplet diameter and grain size are directly proportional to flow rate increased [88] . Moreover, the relationship between droplet diameter, grain size and flow rate were observed by other research groups and described in Equation 14-19 [101,114]. Therefore, denser with higher % film coverage area were likely to be found when flow rate increased due to large size of droplets with high organics matter of precursor were deposited.

Effect of deposit distance

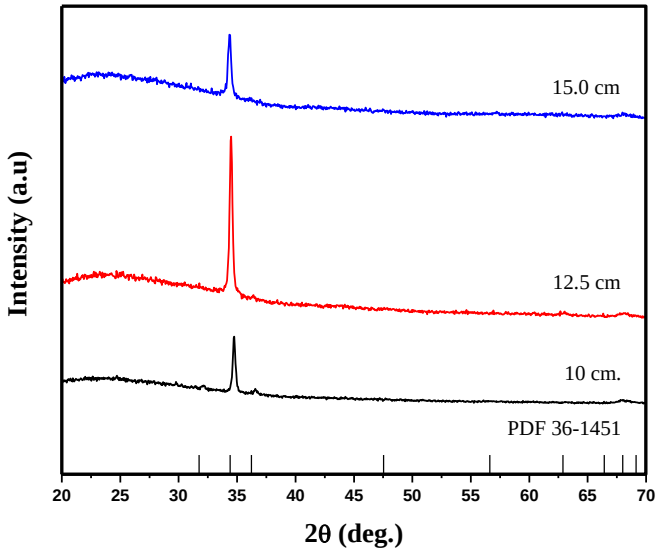

Figure 26. XRD pattern of as-annealed ZnO at 773 K for 5 hr. with different deposit distance. Other process parameters were fixed namely, deposition temperature of 105±5 ºC, applied voltage of 20 kV, flow rate of 0.12 mL/hr, and 1 hr of deposit time.

X-ray diffraction patterns of as-annealed ZnO film with different flow rate of deposition are shown in Fig. 26. All films showed that their structures belonged to Wurtzite structure in $P6_3mc$ space group (PDF# 36-1451) with preferred orientation of c-axis (0 0 2) at 2 theta of ~34.34 °.

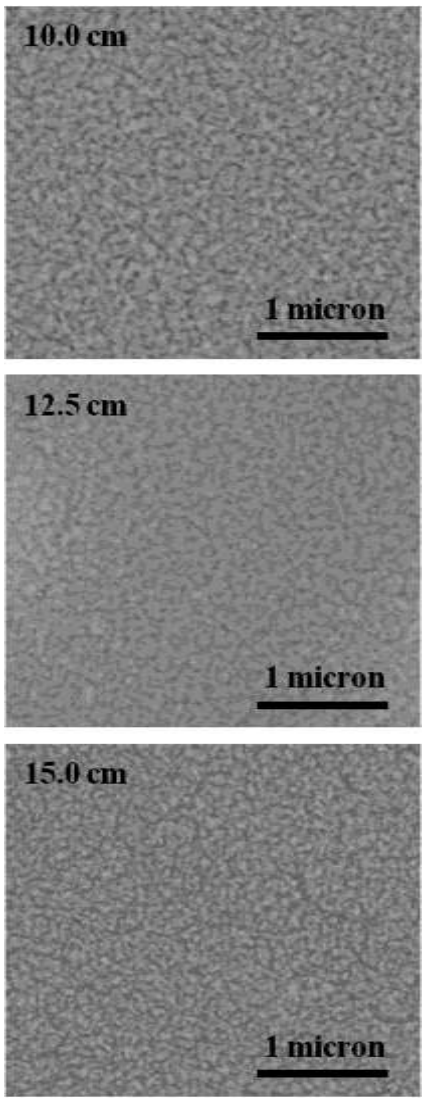

Figure 27. SEM images of as-annealed ZnO with different deposit distance.

SEM images in Fig.27 suggest that a closer distance and lower time of flight led to a higher organic matter of droplets remaining on the substrate due to incomplete evaporation and decomposition processes. Consequently, a denser microstructure was observed at 10 cm of deposition distance. In contrast, a further distance showed less amount of ZnO source precursor to deposit [98], and greater organic materials decomposed and evaporated during deposition process. Therefore, small, dry and particle-like droplets were deposited and observed as deposition distance increased [93]. Effects of deposit distance can be also represented in term of a time of flight of charged droplets which is proportional to distance and inversely related to

electric field in accordance with Equation 10. Therefore, effects to deposit distance on % film coverage area should be considered as an interaction effect with other process parameters in term of decomposition-evaporation process. Moreover, a charge-discharge mechanism of droplets during deposition should be taken into account. As distance increased, a charge-per-volume droplet decreased, [101] so the charged droplet was unlikely to disperse uniformly resulting in % film coverage ratio decreased. Consequently, inhomogeneous surface of a film deposited at the longest distance can be formed as shown in Fig. 27.

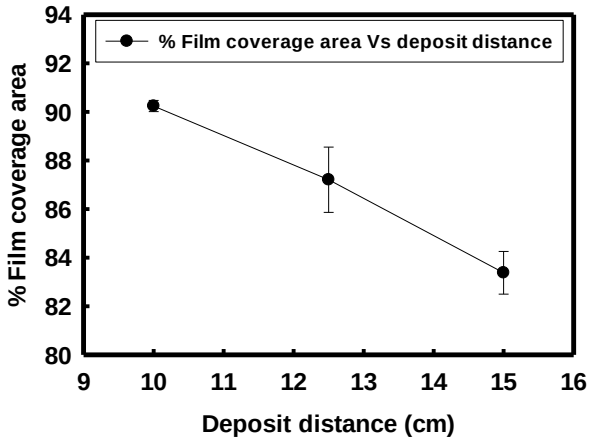

Figure 28. A regression plot of effect of deposit distance on % film coverage area.

A regression plot in Fig. 28 shows that %film coverage decreased as deposit distance increased as describe immediately. As longer time of flight by increasing deposit distance, large amount of organic matter decomposed before deposit on heated substrate. Subsequently, smaller and drier droplet was deposited and contributed to a reduction of % film coverage area as shown in Fig. 27-28.

Effect of deposit time

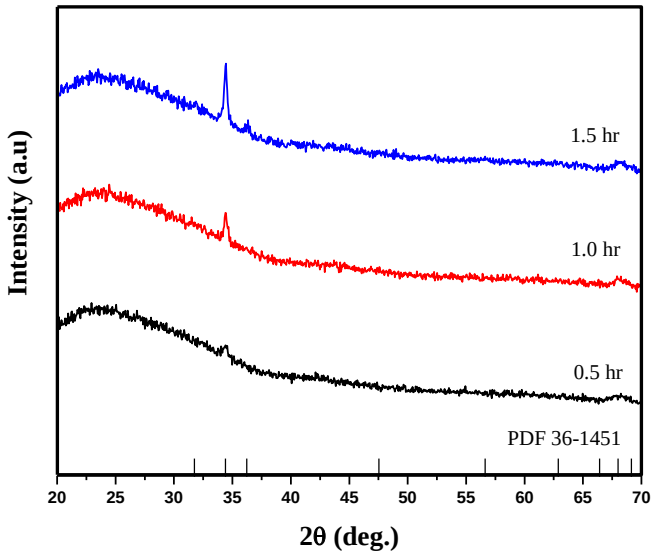

Figure 29. XRD pattern of as-annealed ZnO at 773 K for 5 hr with different deposit time. Other process parameters were fixed namely, deposition temperature of 105±5 ºC, applied voltage of 20 kV, flow rate of 0.06 mL/hr, deposit and distance of 15 cm.

X-ray diffraction patterns of as-annealed ZnO film with different deposit distance are shown in Fig. 29. All films showed that their structures belonged to Wurtzite structure in $P6_3mc$ space group (PDF# 36-1451) with preferred orientation of c-axis (0 0 2) at 2 theta of ~34.34 °.

A longer time straightforwardly showed the denser and thicker deposit layer which contributed to observed prominent peaks of Wurtzite structure as deposit time increased.

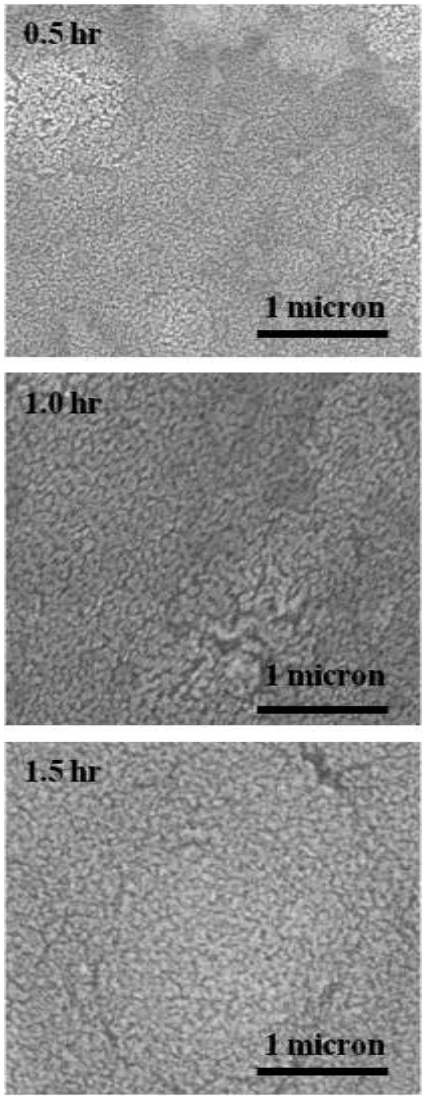

Figure 30. SEM images of as-annealed ZnO with different deposit time.

SEM micrographs in Fig.30 shows that as deposit time increased, denser microstructure was found. As deposit time increased, amount of precursor was deposited and collected on substrate directly increased. Consequently, the film coverage portion increased resulting in % film coverage increased as seen in below regression plot (Fig. 31).

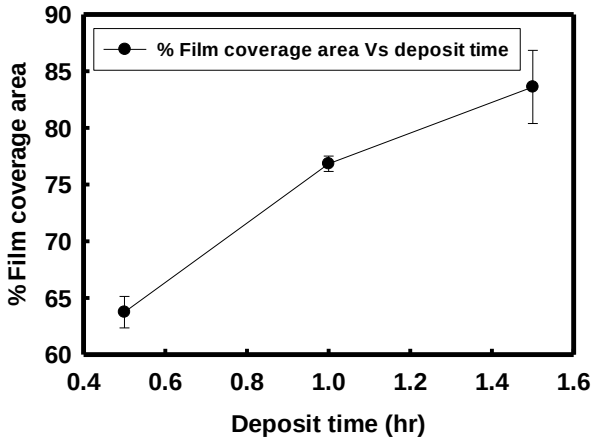

Figure 31. A regression plot of effect of deposit time on % film coverage area.

A regression plot in Fig. 31 indicated that % film coverage area increased as deposit time increased due to greater amount of precursor was collected. Consequently, the denser and higher degree of coverage on surface increased straightforwardly.

Statistical analysis

Table V. Effects of ESD Process Parameters on % Film Coverage Area of ZnO-Based TCO Analyzed by Factorial Design of Experiment

Term	**Effect**	**Coef**	**SE Coef**	**T**	**P**	**Significant [f]**
Constant		75.184	2.103	35.76	0.000	-
Flow rate	9.057	4.529	2.432	1.86	0.105	No
Deposit distance	-7.037	-3.519	2.672	-1.32	0.229	No
Deposit time	18.800	9.400	2.854	3.29	0.013	Yes
Applied voltage	8.384	4.192	2.727	1.54	0.168	No
Deposition temperature	-15.333	-7.677	2.227	-3.44	0.011	Yes

[f] *Statistical significant at P-value < 0.05*

R^2 = 87.61% and Adjusted R^2 = 78.76%

E. Conclusion

The stable cone jet mode can be obtained when DI water was 10% at an applied voltage of 17.5 kV. A higher DI water content required a higher applied voltage to carry the charge droplet and disperse because DI water has a high surface tension and a high electrical conductivity. As a result, the minimum required electric field increased and reached the limitation of this experiment setting parameter. Consequently, isolated droplets and the island-mode of spray were found when DI water content was higher than 10%. The quality of the film was indicated by the % Film coverage area form SEM image. All ESD process parameters were varied at three different levels in order to describe effects of each process parameter on the quality of the film or % Film coverage areas. Regression plots were prepared to reveal effects of each ESD process parameters on % film coverage area. Moreover, the factorial design of experiment suggested that two factors that contributed a significant effect on film quality or % coverage area of the film, namely deposition time and deposition temperature at R^2 of 87.61%.

CO-DOPED P-TYPE ZNO BASED TRANSPARENT CONDUCTIVE FILMS

A. Abstract

Electrospray deposition was equipped to synthesize transparent conductive films in an ambient environment. A co-doping approach by different types of dopants was employed to fabricate a p-type transparent conductive ZnO film for short wavelength applications. Lithium (acceptor, A) provides hole and improves dopant solubility by substitutional mechanism. In addition, Aluminum (donor, D) delocalizes deep-level acceptors and stabilizes ionic charge distribution. Film's crystallinity and microstructure were improved in co-doped samples due to the stress relaxation and better crystallization process were observed in Li co-doped sample. Consequently, optoelectronic properties of as-annealed films were enhanced by a co-doping mechanism. Interestingly, at the optimal Acceptor-to-Donor (A/D) ratio of 2:1 proposed by *Yamamoto*, the defect cluster (A-D-A) tailored the electronic structure of ZnO and increased hole mobility. Consequently, a low resistivity of p-type ZnO was achieved.

B. Introduction

ZnO-based TCO has been investigated to replace Indium Tin Oxide (ITO) due to high thermal and chemical stabilities in a hydrogen atmosphere and availability [4]. Thanks to wide band-gaps and an intrinsic n-type semiconductor, ZnO can find applications in optoelectronic fields. Due to a self-compensation by native defect and a preference to form a deep-level defect, ZnO is challenging to produce p-type ZnO for short wavelength applications such as, blue LEDs, lasers, and solar cells [4,14,130]. *Yamamoto et al.* [10] proposed the optimal Acceptor-to-Donor (A/D) ratio and successfully prepared p-type ZnO by employing a co-doping process in Gallium (Ga) and Nitrogen (N). This report suggested that N-doped ZnO formed a deep-level acceptor, and Ga^{3+} trivalent donor delocalized the deep-level acceptor. Consequently, hole carrier dominated electrical conductivity and exhibited p-type ZnO. At A/D ratio of 2:1, defect cluster (acceptor-donor-acceptor or A-D-A) is formed by electrostatic force and tailor electronic structures. By shifting an acceptor- and donor-level energy towards valence and conduction bands, high conductive p-type ZnO film was achieved. Typically, dopant solubility is the most common issue

in the co-doping process, which degrades as-doped material properties. The compatibility of size and electronegativity between a host and dopants is the key factor to determine doping solubility [5]. Dopants with similar ionic radii compared to host ($\pm$15%) are favorable to improve dopant solubility by inducing substitutional diffusion. Therefore, a small variation of lattice parameters and distortion can be found [11]. Moreover, this diffusion mechanism generates a stress-free growth condition with higher diffusibility and more favorable than that of interstitial and interstitialcy mechanisms [12,70,131,132]. Consequently, crystallinity, microstructure and materials properties can be improved. In this study, Lithium (Li^+, acceptor) which has similar ionic radius to Zn^{2+} was chosen to provide hole carrier and co-doped with an active Aluminum (donor) in order to synthesize p-type ZnO. Unless Li^+ is highly soluble, a deep-level acceptor defect of Li could be formed by residing in interstitial site (Li_i or hole killer) which is more stable than $Li_{Zn}^{'}$. As a result, a hole density and p-type characteristic would be decreased [12,14]. Interestingly, Al^{3+} which is a trivalent donor has been reported to delocalize a deep-level defect as Ga^{3+} in (N,Ga) co-doped ZnO [10,130]. Therefore, it would be feasible to synthesize p-type ZnO by both dopants. Noting that, Al^{3+} would replace Zn^{2+} by an interstitialcy mechanism and bound with O^{2-} which leads to large lattice distortion and oxygen vacancies ($V_O^{\cdot\cdot}$) reduction. Consequently, electrical conductivity decreases [16,133]. In addition, an electrospray deposition was equipped to prepare ZnO film on heated substrates. This economically-versatile method was performed in an ambient condition without a sophisticated apparatuses compared to chemical vapor deposition (CVD), molecular beam epitaxial (MBE). By utilizing a strong electric field, well-dispersed and uniformly-size droplets were formed to fabricate high quality film [18].

C. Experimental procedure

A 0.1 mole of ZnO precursor was prepared by dissolving $Zn(CH_3COO)_2{\cdot}2H_2O$ (Fisher Scientific) in 9:1 v/v of Diethylene Glycol ($\geq$99%BioUltra $C_4H_{10}O_3$, Sigma-Aldrich) and deionized water solution. $AlN_3O_9{\cdot}9H_2O$ ($\geq$98%, Sigma-Aldrich) and CLi_2O_3 ($\geq$99%, Sigma-Aldrich) were doped into ZnO-based precursor to prepare 0, 1.5 and 3.0% of Al-doped ZnO precursors without and with 3% Li co-doped configurations. A KDS100 pump (KD Scientific, Holliston, MA) fed precursors through an electrical field to form droplets which were collected on heated substrate. A flow rate of 0.06 mL/hr with applied voltage of 20.0 kV and 15 cm of deposit distance were used to deposit nano-sized droplets onto glass and <1 0 0> Si wafer at

368± 5 K of for 60 minutes. All samples were annealed at 773 K for 5 hr at 10 K/min. D2 Phaser (Bruker-AXS, Madison, WI) by equipped Cu radiation (CuKα, λ = 1.545 Å) was performed the phase identification on glass substrate ranging from 20-70° of 2theta. Subsequently, the sample was scanned 3 times at the higher scanning rate of X-ray and shorter range (30-38° of 2theta) for structural refinement analyses of XRD data by using *Topaz*® software package. In addition, ESEM (FEI Quanta 200F, Hillsboro, OR) was equipped to examine film's microstructure. A Lamda 950 UV/Vis spectrometer (PerkinElmer, Inc. Waltham, MA) and MMR Hall system (MMR Technologies, Inc. Mountain view, CA) were performed to evaluate optoelectronic properties of as-annealed films.

D. Result and discussion

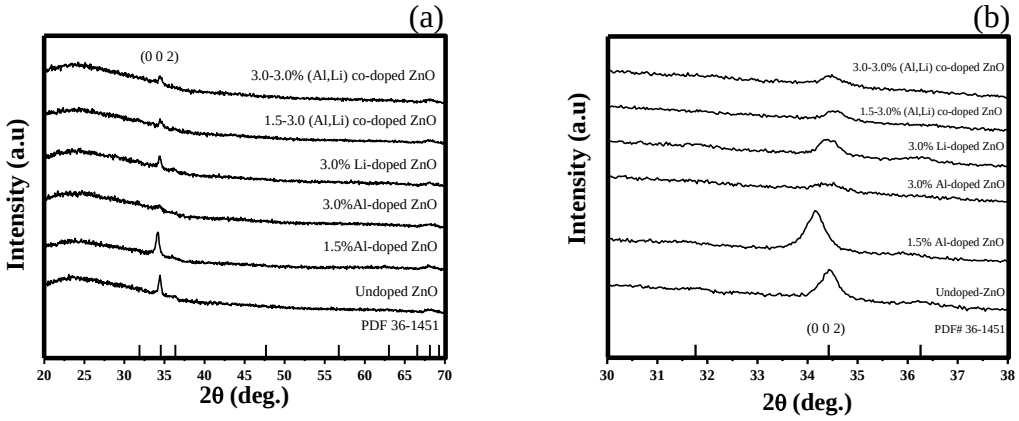

Figure 32. X-ray diffraction patterns of ZnO-based TCOs on glass substrate with different doping configurations ranging from 20-70° (a) and 30-38° (b)

All as-annealed films showed that their structures were Wurtzite in P 6_3mc space group corresponding to PDF# 36-1451. Peak intensities and shapes changed in accordance with doping configurations which were dependent of doing concentration and dopant type. All XRD patterns showed preferred orientation at (0 0 2) which has the lowest surface energy [132]. Comparing to undoped ZnO, all peaks showed broadening effect as a result of disturbance effect inducing by dopants [134]. This effect on film's crystallinity and crystal structure will be discussed in detail as following:

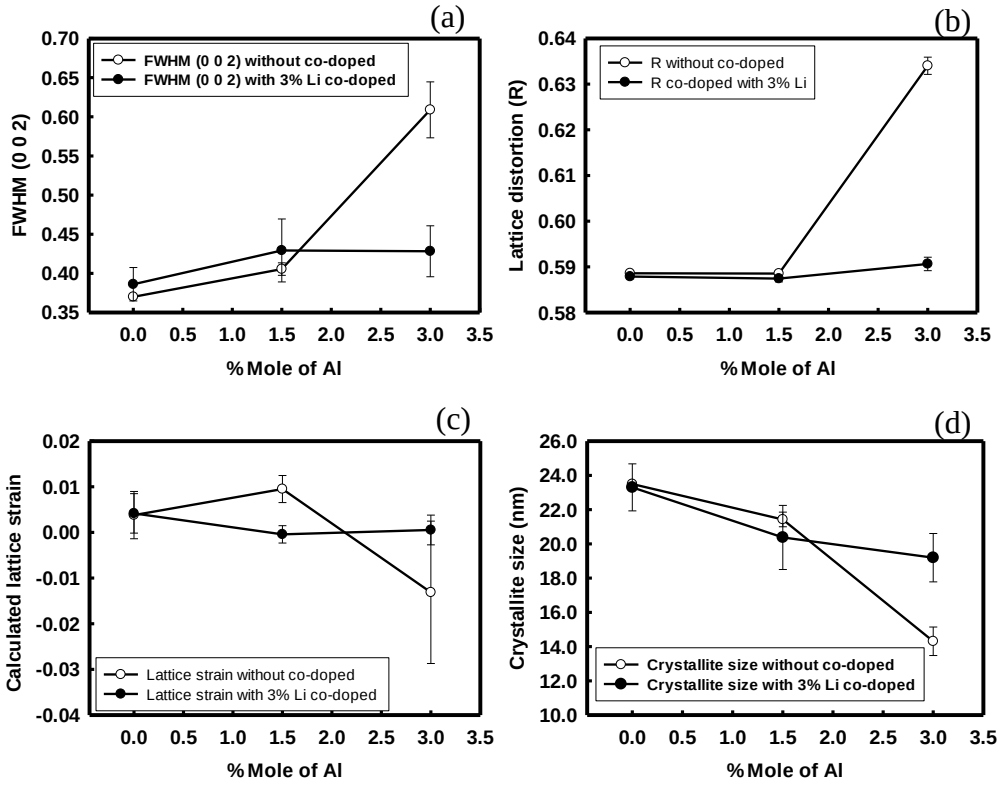

Figure 33. Effects of %Al-doped and co-doped with 3%Li on FWHM (0 0 2) (a), lattice distortion (b), calculated lattice strain (c), and crystallite size (d) of ZnO-based films on glass substrates.

PsudoVoigt refinement methodology in *Topaz*® software package was performed to investigate effects of dopant on as-annealed film's crystallinity on glass substrate by observing FWHM (0 0 2) and plotted in Fig. 33 (a). Lattice parameters of Hexagonal Wurtzite were refined at minimum lattice Lorentzian strain (strain L). Subsequently, lattice distortion (R) were calculated by using equation 26 and plotted in Fig. 33 (b). Biaxial model of lattice strain and crystallite size were calculated by equation 27 and 28, respectively. Consequently, both variables were displayed in Fig.33 (c) and (d) [21,135].

$$R = \frac{2a(\sqrt{2}/3)}{c} \qquad (26)$$

Where R is Lattice distortion degree, a and c are lattice parameters.

$$\varepsilon = \frac{C_{film} - C_{bulk}}{C_{bulk}} \qquad (27)$$

Where ε is biaxial model of lattice strain, C_{film} and C_{bulk} are lattice parameter c from XRD and 5.200 Å, respectively.

$$\tau = \frac{K\lambda}{\beta_\tau \cos\theta} \qquad (28)$$

Where τ is crystallite size (nm), K is shape factor (0.94), λ is wavelength of Cu radiation (1.545 nm), β_τ is line broadening effect, FWHM (Radius.), and θ is diffraction angle (Radius).

According to structural refinement analysis, FWHM (0 0 2) slightly increased in 1.5% Al-doped ZnO as demonstrated in Fig. 33 (a). It suggested that the disturbance which was induced by interstitial ($Al_i^{\cdot\cdot\cdot}$) showed an insignificant effect on the crystallization process at below doping limit (<1.6%) [16]. As a result, a slight change in lattice distortion and lattice strain compared to other doping configurations were observed, as seen in Fig. 33 (b) and (c), respectively. In this regard, crystallite size slight decreased suggesting that the crystallization process allowed grain to growth under tensile condition. As a result, the most pronounced peak was observed in this sample as shown in Fig.32.

In contrast, peak became broader and rarely to be observed at 3% Al-doped ZnO indicating disturbing effect by dopant showed noticeable effect on the crystallization process. FWHM (0 0 2) abruptly increased when Al concentration was higher than 1.6% wt, which agreed with the previous report. As the doping limit of Al was reached, large calculated lattice distortion (R) was found in Fig. 33 (b) by compressive lattice strain as shown in Fig.33 (c). These observations indicated that interstitialcy diffusion of small Al^{3+} ion (0.52 Å) dominated which induced Al^{3+} to replace Zn^{2+} (0.72 Å) at high Al concentration [16,132]. This mechanism increased the migration energy of vacancy-dopant (impurity) exchange process [70]. It implied that diffusibility of defect decreased and restricted the crystallization process [133]. Therefore, diffraction peak was rarely observed as Al concentration increased due to crystal was grown in compressive condition [136]. As a result, film's crystallinity and crystallite decreased which was

reflected by abrupt increasing of FWHM shown in Fig. 33 (a) and by reducing of crystallite size in Fig. 33 (d), respectively.

However, comparing it to Al-doped ZnO, FWHM (0 0 2), a small change in FWHM was found as Al concentration increased when 3% Li was co-doped as seen in Fig. 33 (a). This finding suggested that a disturbing effect by dopant did not affect to crystallization process. Therefore, diffraction peaks in Fig. 32 were still observed in all 3% Li co-doped ZnO samples. Lattice distortion and lattice strain plots showed comparable tendencies in Fig. 33 (b) and (c). These finding suggested that Li^+ substitutional defects (Li'_{Zn}) that were formed by replacing Zn^{2+}. Owing to similar ionic radii between Li^+ (0.60 Å) and Zn^{2+}, and extremely low of ionization energy of substitutional defect [12,133], stress-free condition with high diffusibility was created by substitutional diffusion of Li^+. As a result, crystallization process and film's crystallinity were improved [131,132]. Moreover, lattice strain remained constant in 3-3% (Al, Li) co-doped ZnO. It was implied that interstialcy diffusion of Al^{3+} at a high doping concentration was not found. As a result, dopant solubility and diffusibility would be increased which allowed crystal growth in stress-free condition [11]. Consequently, small decrease of crystallite size was observed in 3% Li co-doped samples.

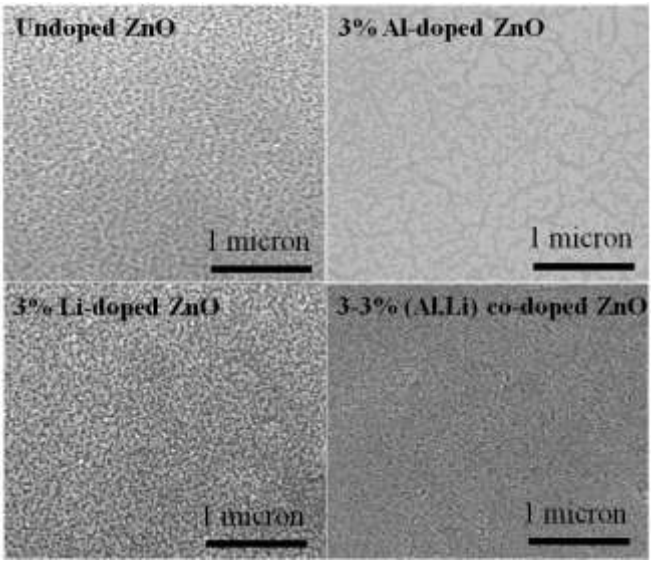

Figure 34. SEM images of ZnO-based TCOs on glass substrates.

The effect of defect diffusion mechanism induced by dopant on film's microstructure is exhibited in Fig.34. Undoped and 3% Li-doped ZnO samples showed large grains due to stress-free growth condition, low magnitude of lattice strain with high diffusibility of substitutional diffusion. Therefore, a grain-coarsening process in these films was observed on as-annealed samples and showed consistency in crystallite size studies as shown Fig. 33 (d). In contrast, a smallest grain size with crazing defects was found in 3%Al-doped ZnO. These because excess compressive stress which was induced by a large-size difference between Zn^{2+} and Al^{3+} and interstitialcy diffusion of Al^{3+}. As a result, new grain boundaries were created to release stress [21,34]. Consequently, finer grains with crazing defects were observed. Interestingly, a smoother surface and uniform grain sizes without distinctively-crazing defect were found in 3% Li co-doped ZnO sample. It indicated that disturbing stress was minimized and diffusibility enhanced by substitutional diffusion of Li ($Li_{Zn}^{'}$).

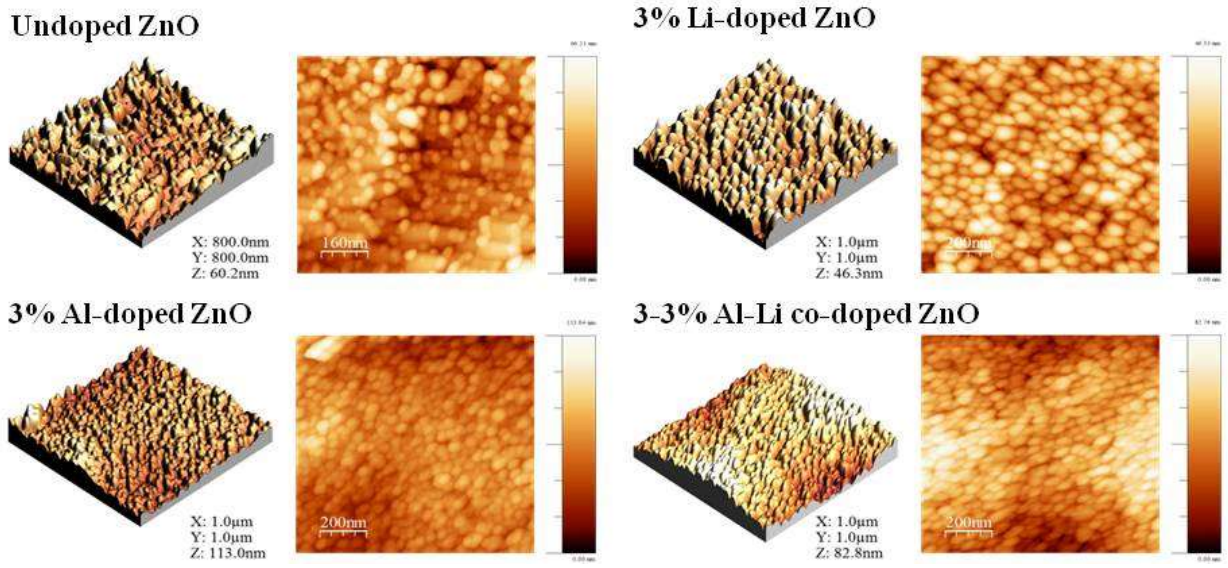

Figure 35. AFM images of as annealed ZnO-based TCOs on glass substrates at 773 K for 5 hr with different doping configurations. 0.05 Mole of ZnO in DEG: DI water of 3:1 precursor. Other process parameters were fixed namely, deposition temperature of 413±5 ºC, flow rate of 0.12 mL/hr, 22.5 kV of applied voltage, deposit distance of 15 cm and 1.5 hr deposit time.

Table VI. Roughness Evolution of As-Annealed ZnO-Based TCO Film Observed by Atomic Force Microscopy

Sample detail	Average roughness (nm)	RMS roughness (nm)	Skewness
Undoped ZnO	9.16	11.53	0.37
3%Li-doped ZnO	5.34	6.55	-0.26
3%Al-doped ZnO	33.64	41.60	-0.19
3-3%Al-Li co-doped ZnO	13.70	16.74	0.05

AFM images in Fig. 35 reveal the topography of samples with different doping configurations. Undoped and 3% Li-doped ZnO samples exhibited larger grain size compared to other doped and co-doped ZnO samples which were consistent with crystallite size and microstructure studies by XRD and SEM, respectively. Both films were grown in a stress-free condition due to no impurity existed or a low magnitude of lattice strain by substitutional diffusion of Li^{+}. These conditions allowed grains to grow with high diffusibility. As a result smooth surfaces were observed in both samples. In contrast, a rougher surface was found in 3.0% Al-doped ZnO indicating that an atomic diffusibility decreased by interstitialcy mechanism which restricted grain-coarsening process. Moreover, a large-size difference between Al^{3+} and Zn^{2+} (host) induced disturbance or stress. As a result, degenerated issues prohibited the growth process and led to small grain size. Interestingly, smoothness and a well-distributed surface was found in 3-3% (Al,Li) co-doped ZnO sample. It implied that incorporation of co-dopant (Li^{+}) mitigated disturbing stress by inducing substitutional diffusion. Consequently, surface roughness significantly dropped in average roughness and RMS valued with the smallest skew seen in Table VI.

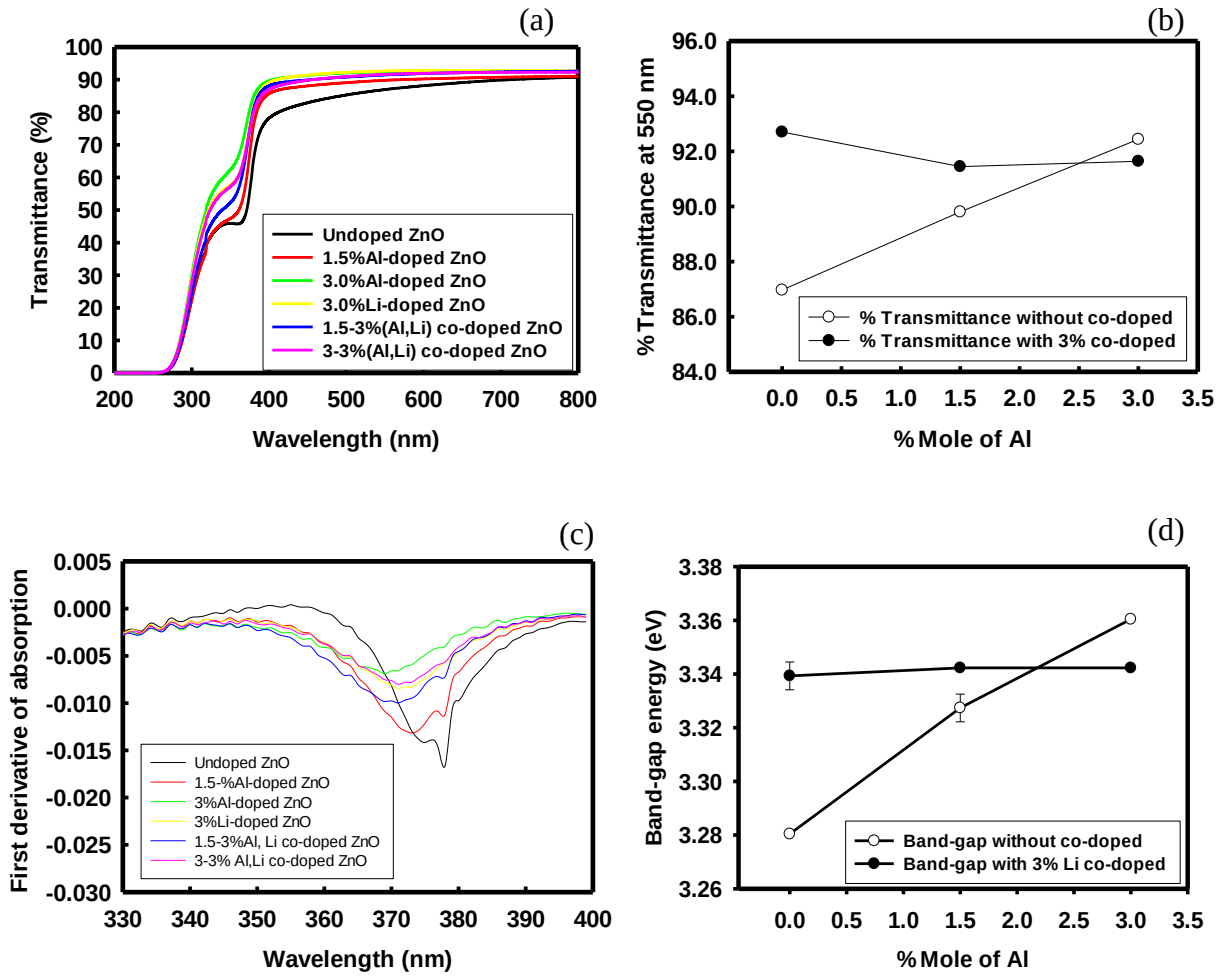

Figure 36. Effects of %Al-doped and co-doped with 3%Li on transmittance spectra in UV-Visible range (a), % transmittance at 550 nm (b), first derivative plot of absorption (c) and band gap energy (d) of as-annealed ZnO-based films on glass substrates.

The optical transmittance of as-annealed films is revealed in Fig.36 (a) and (b). UV-Visible transmittance spectrum showed that all doped samples had %transmittance higher than 80% in visible range (400-700 nm) which met the minimum requirement of TCO. Due to nano-scaled grains and thickness (~160 nm by crossed-sectional SEM), visible light can pass without scattering in all samples. Moreover, when 3% Li was co-doped, smoother surface were obtained which reduced a diffusive scattering effect resulting in transmittance increased. First a derivative

plot of absorption from 320 to 400 nm was plotted in Fig. 36 (c) in order to determine absorption edge of as-annealed film on glass substrates. All doped samples showed strong absorption at wavelengths ranging from 360-380 nm, which was consistent with that of bulk ZnO. Subsequently, the de Broglie wave expression was employed to calculate band-gaps energy of all films. Regarding to undoped ZnO, all doped samples showed Burstein-Moss effect or band-gap widening seen in Fig. 36 (d). As donor-type dopant increased, electron density increased and was blocked at the lowest part of a conduction band according to the Pauli's Exclusion principle. Consequently, band-gaps energy increased as Al concentration increased [21,117]. However, band-gaps energy of (Al,Li) co-doped samples remained constant indicating that excess electrons from Al^{3+} was normalized by holes which were created by Li'_{Zn}. Consequently, electron density and band-gaps energy were kept constant as Al concentration increased.

Table VII. Electrical Properties of Co-Doped ZnO-Based TCO on Si Wafer

Sample detail	**Type of carriers**	**Carrier density (cm^{-3})**	**Mobility (cm^2/V-s)**	**Resistivity (Ohm·cm)**
3% Li-doped ZnO	holes	3.91E+16	1.29E+03	1.24E-01
1.5-3% (Al-Li) co-doped ZnO	holes	9.14E+16	2.72E+04	2.51E-03
3-3% (Al-Li) co-doped ZnO	holes	2.13E+17	1.88E+02	1.56E-01

Hall effect measurement was performed to evaluate electrical properties and carrier type of films on <1 0 0> Si wafer as shown in Table VII. All Li co-doped films showed that holes were dominated carriers. Therefore, conductive p-type ZnO films can be achieved by doping Li^+. As Li incorporation, substitutional defects were ionized in accordance with following defect formation equations;

$$Li_2O \rightarrow 2Li'_{Zn} + V_{\ddot{O}} + O_O^x \quad (29)$$

Then the partial pressure effect was introduced to get electronic defects in order to maintain a charge neutrality condition as following;

$$1/2\ O_{2\,(g)} + V_{\ddot{O}} \rightarrow O_O^x + 2\acute{h} \qquad (30)$$

According to both defect equations, every single mole of Li^+ created two holes to dominate electrical conductivity and exhibit p-type behavior.

As Al concentration increased, the carrier density increased due to a greater amount of defect and was ionized by increasing doping concentration. Moreover, Al^{3+} can delocalize deep-level acceptors when co-doped with p-type dopant resulting in acceptor defects and hole population increased [15]. In addition a low magnitude of strain when Li was co-doped in Fig. 33(c) decreased formation energy of extrinsic defect decreased and increased that of intrinsic defect i.e. vacancies As a result, compensating effects by this intrinsic defect does not neutralize holes carriers [14].

However, an ambiguous tendency was found in carrier mobility as seen in Table VII. As Al increased, the highest hole mobility was found 1.5-3% (Al-Li) co-doped ZnO film which was the optimal acceptor-to-donor (A/D) ratio proposed by *Yamamoto.* At this A/D ratio, defect clusters (A-D-A) were formed, and tailored electronic structures of ZnO. Moreover, these defect clusters exhibited short-range dipole-like scattering behavior which reduced ionized scattering effect. As a result, hole mobility drastically increased to 2.72E+04 $cm^2/V\text{-}s$ [130]. Exceeding the optimal A/D ratio, hole mobility abruptly decreased by magnitude of two to $1.88x10^{-2}$ $cm^2/V{\cdot}s$. It implied that the ionized scattering effect increased as carrier density increased.

According to hole mobility increased at the optimal A/D ratio, one would conclude that as diffusibiltiy improved by subsitutional diffusion mechanism, ionic conductivity increased with respect to Einstein relation as shown below [134]:

$$\mu kT = eD \qquad (31)$$

Where μ is carrier mobility, k is Boltzman constant, T is temperature, e is constant of electric field and D is diffusion coefficient.

Consequently, the lowest resistivity of 2.51×10^{-3} Ohm·cm was obtained by employing the optimal A/D ratio.

E. Conclusion

A dopant solubility of (Al,Li) co-doped ZnO-based TCO improved and showed small lattice distortion and strain as Al concentration increased by a substitutional mechanism of Li. Subsequently, disturbing stress was minimized, and diffusibility was enhanced resulting in film's crystallinity and the surface quality improved by co-doping mechanism. A-D-A defect cluster tailored electronic structures of undoped ZnO, which improved hole mobility and reduced the ionized defect scattering effect. Consequently, the lowest resistivity of p-type ZnO-based TCO was achieved without the optical properties degradation.

COMPARATIVE STUDIES OF CO-DOPED ZNO-BASED TRANSPARENT CONDUCTIVE FILMS

A. Abstract

Aluminum (Al)-doped ZnO or AZO with two different types of co-dopant were deposited by using electrospray deposition. The aim was to compare the effect of co-dopant types on dopant solubility, film's crystallinity, microstructure, and optoelectronic properties of ZnO-based transparent conductive oxide (TCO). A substitutional diffusion enhanced dopant solubility in Li co-doped samples that showed small variation of lattice parameters and distortion. As a result, film's crystallinity and microstructure were improved due to stress relaxation and better crystallization process were observed. Consequently, the lowest resistance without optical properties degradation was found in 1.5-3% (Al,Li) co-doped ZnO. However, when 3% Ga was co-doped (n-type, Donor), excess tensile stress caused severe cracks and optical properties degradation. In addition, the strain-induced absorption edge was made and showed a high correlation at R^2 of 87.91% by linear fitting plot.

B. Introduction

The development of ZnO-based TCO aims to enhance optoelectronic properties and replace Indium Tin Oxide (ITO) for functional display panel applications. A scarcity of materials and sensitivity to hydrogen atmosphere of ITO attract many researches on ZnO which is non-toxic, abundant and able to withstand in plasma condition [2]. Although, ZnO belongs to II-VI n-type semiconductor and large band-gaps, these intrinsic properties are still inferior to ITO [16]. Therefore, several research groups make attempts on improving ZnO by the doping approach. Aluminum (Al) has been investigated to improve electrical conductivity by providing free electron to undoped ZnO. Interestingly, it can delocalize a deep-level acceptor and stabilize charge distribution which can be beneficial for the synthesis of p-type ZnO when co-doped with acceptor-type dopant and improve electronic properties [10]. However, the small ionic radius of Al^{3+} (r_{Al3+} = 0.52 Å) is likely to reside at an interstitial site, which disturbs the crystallization process and increases ionized defect scattering to degrade optoelectronic properties. Moreover, large lattice distortion induced by interstitialcy diffusion leads Al^{3+} to replace Zn^{2+} at high doping concentration. As a result, electron density and electrical conductivity decrease [16,71,133].

To overcome this issue, co-dopants with similar ionic radii compared to host ions (± 15%) are favorable to prevent interstitialcy of Al by the co-doping approach. Co-dopants induce substitutional diffusion and generate a stress-free growth condition with high diffusibility compared to interstitial and interstitialcy diffusions [12,131,132]. Therefore, solubility of Al can be improved by co-doping which is reflected by small variation of lattice parameters and distortion [11]. Consequently, crystallinity, microstructure and materials properties can be improved. In this report, two different types of co-dopant, Lithium (Li^+, Acceptor) and Gallium (Ga^{3+}, Donor) which have larger ionic radii compared to Al^{3+} were chosen to improve the dopant solubility (r_{Li+} = 0.60 Å, r_{Ga3+} = 0.69 Å). Both co-dopants preferably form substitutional defects by replacing Zn^{2+} due to comparable size to Zn^{2+} (r_{Zn2+} = 0.72 Å) [12]. However, they have been reported to form interstitial defects are unfavorable which would increase migration energy of vacancy-dopant exchange process, decreases diffusibility, increase tensile stress and neutralize charge carriers [70,76,131,137]. As a result, optoelectronic properties decrease. Therefore, it is challenging to report comparative effects of these co-dopants with AZO in order to maximize optoelectronic properties of ZnO-based TCO. In addition, the economically-versatile thin film fabrication, ESD, was carried out to deposit films in an ambient environment. By utilizing a strong electric field, well-dispersed and uniformly-sized droplets were deposited and high quality films were obtained [18].

C. Experimental procedure

A 0.1 mole of ZnO precursor was prepared by dissolving $Zn(CH_3COO)_2 \cdot 2H_2O$ (Fisher Scientific) in 9:1 v/v of Diethylene Glycol (≥99%BioUltra $C_4H_{10}O_3$, Sigma-Aldrich) and deionized water solution. $AlN_3O_9 \cdot 9H_2O$ (≥98%, Sigma-Aldrich), CLi_2O_3 (≥99%, Sigma-Aldrich), and GaN_3O_9 (99.9%, Sigma-Aldrich) were doped into ZnO-based precursor to prepare 0, 1.5 and 3.0% of Al-doped ZnO precursors at three different configurations namely, without co-doped, with 3% Li co-doped, and with 3% Ga co-doped. All doping configurations were displayed in Table VIII. A KDS100 pump (KD Scientific, Holliston, MA) fed precursor through an electrical field to form charged droplets that were collected on heated substrates. A flow rate of 0.06 mL/hr with applied voltage of 20.0 kV and 15 cm of deposit distance were used to deposit nano-sized droplets onto heated glass and <1 0 0> Si-wafer at 368± 5 K of for 60 minutes. All samples were annealed at 773 K for 5 hr at 10 K/min. D2 Phaser (Bruker-AXS,

Madison, WI) by equipped Cu radiation (CuKα, λ = 1.545 Å) was performed the phase identification on glass substrate ranging from 20-70° of 2theta. Subsequently, the sample was scanned 3 times at the higher scanning rate of X-ray and shorter range (30-38° of 2theta) for structural refinement analyses of XRD data by using *Topaz*® software package. In addition, ESEM (FEI Quanta 200F, Hillsboro, OR) was carried out to evaluate microstructure of as-annealed films. A Lamda 950 UV/Vis spectrometer (PerkinElmer, Inc. Waltham, MA) and a 4-Point Probe with Keithley2400 sourcemeter® (Keithley Instruments, Inc. Cleveland, OH) were performed to evaluate optoelectronic properties of films.

Table VIII. Doping Configurations

%Al content	**Without co-doped**	**With 3% Li co-doped**	**With 3% Ga co-doped**
0.0	A-1	AL-1	AG-1
1.5	A-2	AL-2	AG-2
3.0	A-3	AL-3	AG-3

D. Result and discussion

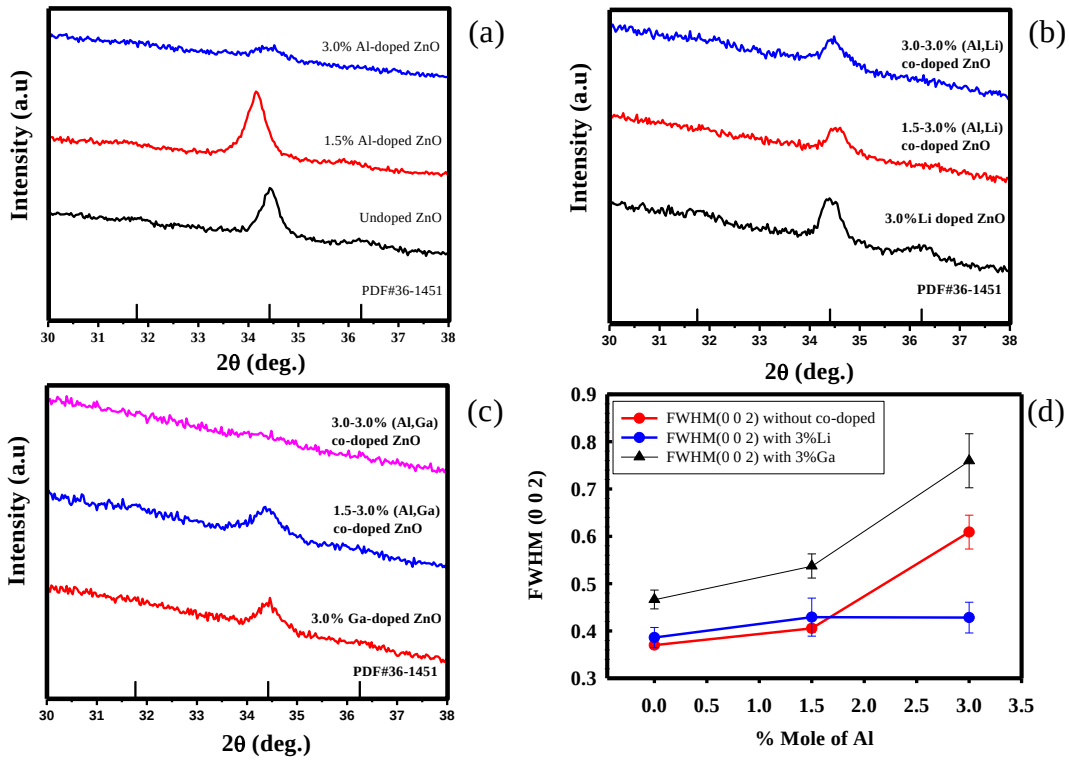

Figure 37. X-ray diffraction patterns of as-annealed Al- based ZnO TCO on glass substrates without co-dopant (a), with 3% Li co-doped (b), with 3% Ga co-doped (c), and FWHM (0 0 2) at different doping configurations (d).

The effect of dopant configurations on film's crystallinity is revealed in Fig.37. All films show a preferred orientation of plane (0 0 2) at 2θ~34.34° with different intensity and shape as shown in Fig. 37 (a) to (c). The most pronounced peak was observed in Fig. 37 (a) which belonged to 1.5% Al-doped ZnO (A-2). At below doping limit (<1.6% wt), small Al^{3+} ions showed insignificant effects of disturbing stress on crystallization process by residing in interstitial sites [16]. However, the peak became broader, and intensity suddenly dropped indicating that crystal structure was not completely formed by interstitialcy mechanism at 3% Al-doped ZnO (A-3) [16,133]. Owing to a large-size difference between Al^{3+} and Zn^{2+}, interstitialcy diffusion of Al^{3+} was induced resulting in the migration energy of vacancy-dopant (impurity) exchange process increased [70]. It implied that diffusibility of defect decreased and restricted the crystallization process [133]. Consequently, film's crystallinity decreased, and contributed to

increase FWHM as shown in Fig. 37 (d) [16]. In contrast, when 3% Li was co-doped with Al-coped ZnO (AL-1 to AL-3), peaks at plane (0 0 2) could still be observed as Al concentration increased seen in Fig. 37 (b). Due to ionic radii of Li^+ and Zn^{2+} are similar, Li^+ is likely to occupy in Zn-site (Li'_{Zn}) by a substitutional mechanism. Therefore, it could prevent interstitialcy diffusion of Al_i''' to localize at Zn-site as a result diffusibility improved. Subsequently, a low magnitude of stress and strain by Li'_{Zn} defect allowed a better crystallization process to carry out [12,133]. Consequently, film's crystallinity remained constant as % Al increased which was reflected by small change of FWHM when Al concentration increased. However, diffraction peaks were rarely observed when 3% Ga was co-doped in AZO (AG-1, AG-2) and eventually disappeared at 3-3% (Al,Ga) co-doped ZnO (AG-3) as shown in Fig. 37 (c). These results suggested that as Ga^{3+} was co-doped, film's crystallinity drastically decreased compared to Al-doped and 3% Li co-doped ZnO samples. Even though Ga^{3+} (0.69 Å) has a similar size compared to Zn^{2+}, excess Ga^{3+} ions preferably formed interstitial defects rather than substitutional ones at high concentration [76]. Therefore, migration energy of vacancy-dopant (impurity) exchange process increased as found in Al-doped ZnO [70]. This due to interstitial defects of large size co-dopant (Ga_i''') which induced highly-stress condition, and limited crystallization process. Consequently, FWHM abruptly increased in 3-3% (Al,Ga) co-doped ZnO (AG-3). In addition, effects of dopant types and concentrations on crystallinity (FWHM) are summarized in Fig. 37 (d). This plot indicated that a dramatic increase of FWHM was observed in high concentration of n-type samples (A-3, AG-3) by interstitial and interstitialcy mechanisms. While FWHM (0 0 2) remained constant in 3% Li co-doped ZnO samples inducing by substitutional mechanism of Li^+.

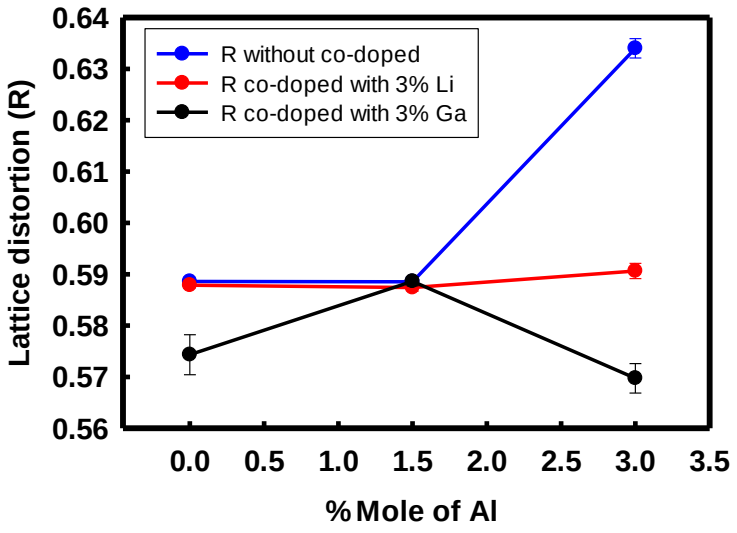

Figure 38. Effects of %Al-doped ZnO without co-dopant and co-doped with 3%Li and 3%Ga on lattice distortion (R).

Structural refinement analysis by PseudoVoigt methodology in *Topaz*® software package was carried out to evaluate lattice parameters. Lattice parameters of Hexagonal Wurtzite were refined at minimum lattice Lorentzian strain (strain L). Subsequently, lattice distortion (R) were calculated by using equation 26 and the variation of hexagonal Wurtzite structure as a function of doping configurations was revealed in Fig. 38. This lattice distortion plot suggests that undoped and 1.5% Al-doped samples (A-1, A-2) showed the same level of lattice distortion indicating that interstitial defects of Al^{3+} showed an insignificant effect on lattice parameters as well as crystallization process at below doping limit (~1.6%wt) [16]. However, lattice distortion suddenly increased at 3% Al-doped ZnO samples (A-3) suggesting that interstitial defect of Al^{3+} (Al_i''') induced interstitialcy mechanism by replacing Zn^{2+} when Al concentrations exceeded the doping limit [131,133]. Owing to a much smaller ionic radius of Al^{3+} than Zn^{2+}, lattice parameter *c* noticeably changed which contributed to a large lattice distortion. In contrast, lattice distortion remained constant as Al concentration increased when 3% Li was co-doped (AL-1 to AL-3). Regarding a similar size and extremely low ionization energy of Li substitute defect (Li_{Zn}'), Li^{+} prefers occupying at Zn-site by substitutional mechanism [12]. As a result, interstitialcy defect of Al^{3+} could not replace and occupy at Zn-site. Therefore, Al^{3+} remained at interstitial site (Al_i''')

which compensated a small contraction of lattice parameter *c* after Li^{+} substituting Zn^{2+}. Consequently, 0-3% AZO with 3% Li co-doped samples exhibited small variation of lattice parameters indicating that dopant solubility was enhanced. However, as 3%Ga was co-doped, the low lattice distortion was found as a result of Ga-substitutional and interstitial defects were formed. Both types of defect were likely to form at 3% of Ga which increased lattice parameter *c* and reduced crystallinity as previously reported [76]. Interestingly, the identical lattice distortion was observed when 3% Ga was co-doped with 1.5%Al-doped ZnO (AG-2). This suggested that Ga^{3+} substituted at Zn-site and induced small Al^{3+} resided in interstitial site. Therefore, no change in lattice parameters and distortion was observed. However, lattice distortion also decreased in 3-3% (Al,Ga) co-doped ZnO (AG-3) due to lattice parameter *c* was enlarged by interstitial defects of Ga (Ga_i'''). Consequently, a large variation of lattice distortion compared to undoped ZnO sample was observed. One would conclude that lattice distortion decreased with the increase of dopant solubility by the substitutional mechanism when ionic radii of dopant and host are comparable. Whereas, low dopant solubility, which were induced by interstitialcy and interstitial mechanisms, showed a large variation of lattice parameters and distortion as seen in Fig.38.

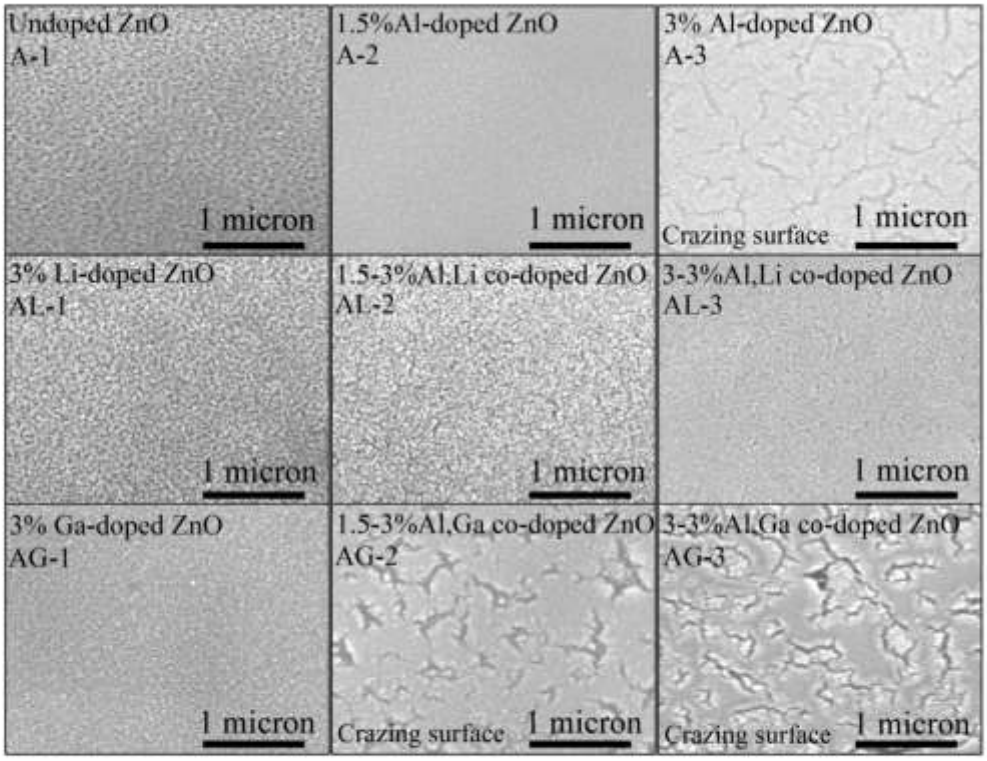

Figure 39. SEM images of ZnO-based TCOs on glass substrates.

Effects of dopant types and concentration on film's microstructure were observed by SEM and shown in Fig.39. Undoped, 3% Li-, and 3% Ga-doped ZnO samples (A-1, AL-1, AG-1) exhibited interconnected-large grain sizes compared to others. These findings indicated that both films were grown in stress-free or low magnitude stress conditions with high diffusibility by substitutional mechanism. Therefore, better growth or crystallization processes were found in both samples. In contrast, a large-size difference between Al^{3+} and Zn^{2+} induced high disturbing stress by either interstitial or interstitialcy mechanisms. As a result, degenerated issues and decreased diffusibility restricted grain growth process as % Al increased (A-2, A-3) [21]. Interestingly, 1.5-3% and 3-3% (Al,Li) co-doped ZnO (AL-2, AL-3) showed smoother and denser surfaces than 3% Al-doped ZnO (A-3). These findings indicated that disturbing stress were pacified and diffusibility was improved by Li substitute defects (Li'_{Zn}) [12]. On the other

hand, when 3% Ga was co-doped, tensile stress was enlarged as Al concentration increased by interstitial defects of Al^{3+} and Ga^{3+} (Al_i''', Ga_i'''). Consequently, surfaces released excess tensile stress by forming new boundaries [34] and showed crazing defects as denoted in Fig. 39 in following doping configurations; 3% Al-doped ZnO, 1.5-3%, and 3-3% (Al,Ga) co-doped ZnO (A-3, AG-2, AG-3).

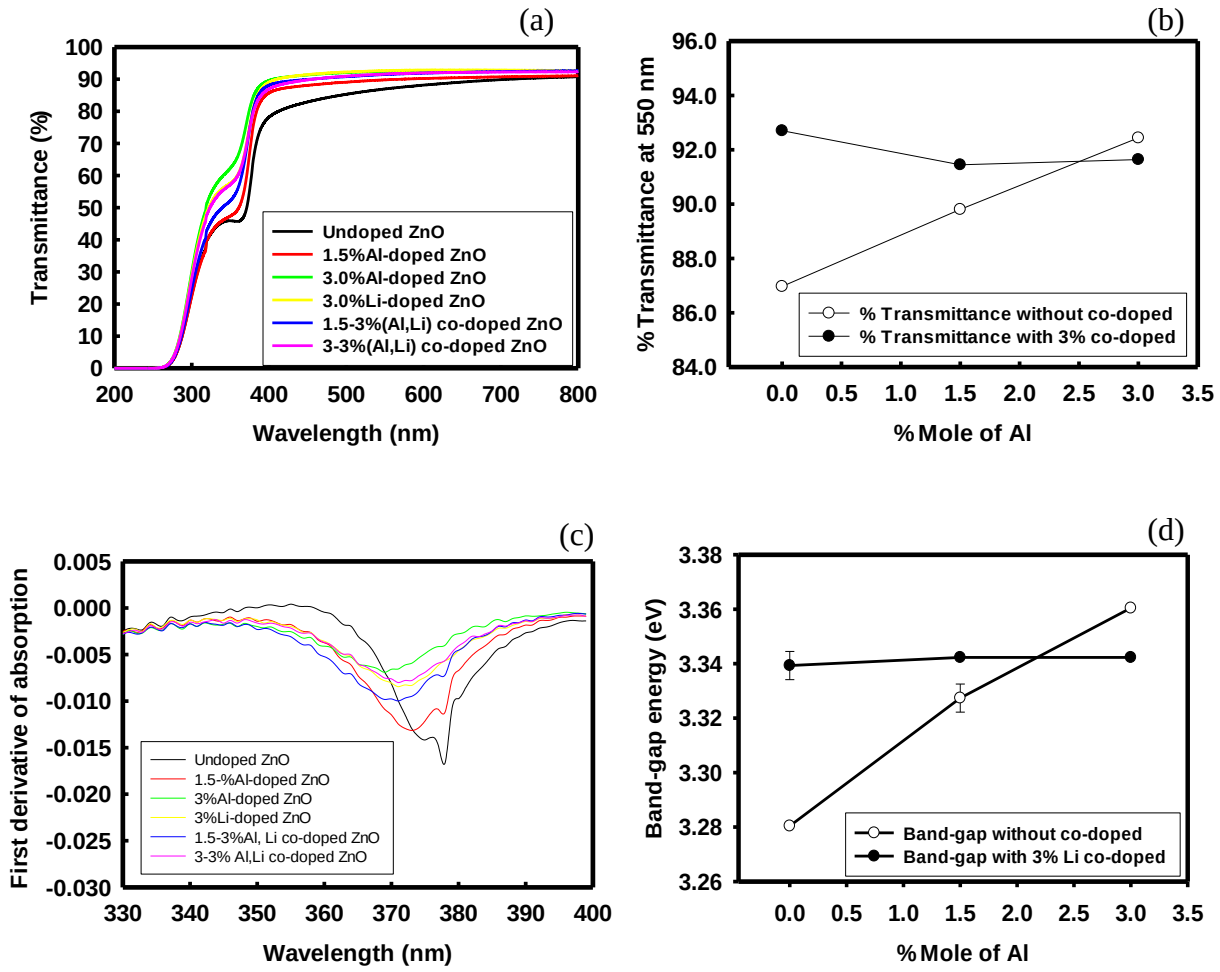

Figure 40. Effects of %Al-doped, 3% Li and 3% Ga co-doped on transmittance spectra in UV-Visible range (a), % transmittance at 550 nm (b), first derivative plot of absorption (c) and band gap energy (d) of as-annealed ZnO-based films on glass substrates.

The optical transmittance of as-annealed films is revealed in Fig.40 (a) and (b). UV-Visible transmittance spectrum showed that all doped samples had % transmittance higher than 80% in visible range (400-700 nm). Therefore, all doped samples were qualified for transparent conductive application. As seen in SEM images in Fig. 39, nano-sized grains with thickness (~160 nm by crossed-sectional SEM), visible light scattering effect can be discarded in all doped samples except for 3% Ga co-doped samples (AG-2, AG-3). Both samples showed crazing defects which acted as scattering centers to decrease % transmittance at 550 nm. However, smoother surfaces were obtained when 3% Li was co-doped which showed transmittance over 90% at 550 nm as seen in Fig. 40 (b).

In addition, a first derivative plot of absorption from 320 to 400 nm of as-annealed film on glass substrates is presented in Fig. 40 (c). All doped samples showed strong absorption at wavelength ranging from 360-380 nm, which was consistent with that of bulk ZnO. Subsequently, band-gaps energy of all films was calculated by employing the de Broglie wave expression. Regarding to undoped ZnO, all doped samples showed Burstein-Moss effect or band-gaps widening seen in Fig. 40 (d). As doping concentration increased, electron density increased and was blocked at the lowest part of a conduction band according to the Pauli's Exclusion principle. As a result, band-gaps energy got wider as % Al increased compared to an undoped sample [21,117]. However, band-gaps energy of (Al,Li) co-doped samples remained constant indicating that excess electrons from Al^{3+} was normalized by an acceptor-type defect (Li'_{Zn}). Consequently, electron density and band-gaps energy were maintained as Al concentration increased.

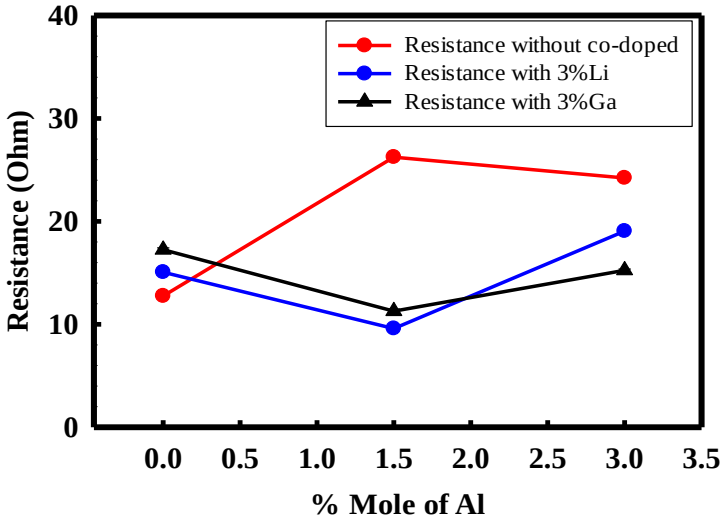

Figure 41. Effects of %Al-doped and co-doped with 3%Li and 3%Ga toward electronic resistance of ZnO-based films on <1 0 0> Si wafer.

Film resistance was measured by a 4-point probe suggests that the scattering of ionized defects increased in all single-doped samples (A-2, A-3). Moreover, the formation energy of extrinsic defects decreased as lattice stain increased [14] contributed to increase ionized defects by doping. Consequently, the electrical resistance increased by scattering effect of ionized defect in heavy-doping concentration (AL-1, AL-3, AG-1, AG-3) as shown in Fig.41. Interestingly, the lowest resistance was found at 1.5-3%Al-Li co-doped ZnO (AL-2) by employing the optimal Acceptor-to-Donor (A/D) ratio of 2:1 proposed by *Yamamoto et al.*. This ratio induced the defect cluster (A-D-A) to form by electrostatic forces between acceptor and donor. Subsequently, this cluster shifted acceptor- and donor-energy levels towards valence and conduction bands, respectively [10]. Moreover, A-D-A cluster exhibited the short-range dipole-like behavior, which reduced the scattering effect from ionized defects. As a result, electrical resistance decreased [130]. Surprisingly, low resistance film was also observed at 1.5-3% (Al,Ga) co-doped ZnO (AG-2) which implies that as diffusibility increased carrier mobility would increase, which was consistent with Einstien relation [134]. As a result, film resistance decreased. However, as %Al increased to 3% and co-doped with 3% Li and 3% Ga (AL-3, AG-3), film resistance increased due to an ionized defect scattering enhanced as ionized defect population increased in heavily-doped condition.

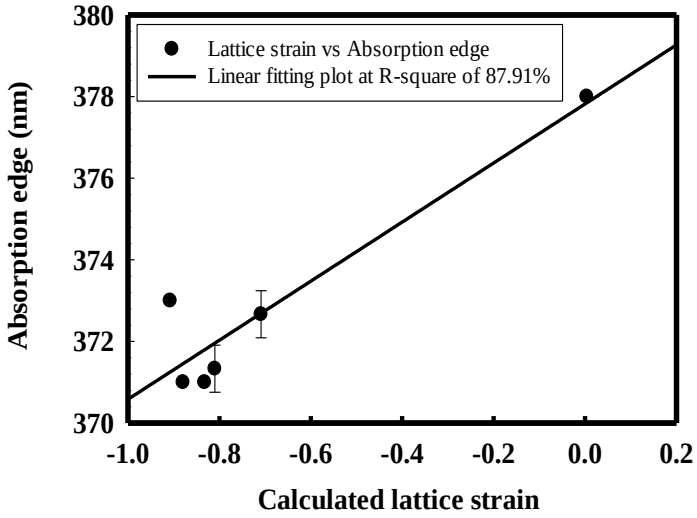

Figure 42. Effects of biaxial strain at c-axis to absorption edge of film on glass substrate.

The correlation plot in Fig. 42 reveals that a blue-shifting of absorption edge was observed when lattice was in compressive due to the repulsion force between Op^2 and Zns^4 increased [32]. This strain-absorption edge of films relationship showed highly correlated at R^2 of 87.91% by linear fitting correlation. Noting that three doped samples were excluded namely, 3% Al-doped ZnO, 1.5-3% (Al,Ga) co-doped and 3-3% (Al,Ga) co-doped ZnO samples (A-3, AG-2, and AG-3) due to the lattice strain in these samples were underestimated from the effect of crazing surfaces shown in Fig.39.

E. Conclusion

Co-doping mechanisms with different types of dopant improved dopant solubility, diffusibility and showed small variations in lattice distortion. This improvement contributed to better crystallinity and microstructure as well as optoelectronic properties. Optical transmittance in the visible range increased and the Burstein-Moss effect was observed in doped samples due to increased electron density. Most importantly, the lowest resistance was obtained without optical properties degradation at optimal A/D ratio of 2:1. In addition, the linear fitting plot showed a high correlation between bi-axial lattice strain and absorption edge at R^2 of 87.91%.

SUMMARY AND CONCLUSIONS

Electrospray deposition (ESD) process parameters were thoroughly investigated and revealed by regression plots in section III. The stable cone jet mode can be obtained when DI water was 10% at an applied voltage of 17.5 kV. Higher DI water content required a higher applied voltage to carry charged droplets and disperse them due to a high surface tension and a high electrical conductivity of DI water. As a result, the minimum required electric field increased and reached the limitation of this experiment setting a parameter. The factorial design of the experiment indicated that deposit time and deposition temperature showed significance towards the film's quality, which reflected by %film coverage area at R^2 of 87.61%.

The effect of a co-doping mechanism between Li (Acceptor) and Al (Donor) towards crystal structure, microstructure, topography, and optoelectronic properties was evaluated in section IV. At the optimal A/D ratio of 2:1, dopant solubility of (Al-Li) co-doped ZnO-based TCO was improved which showed in small lattice distortion and strain by substitutional diffusion mechanism. As a result, an excess stress was minimized in high doping concentrations, which enhanced surface qualities and film's crystallinity by Li^+ incorporation. A-D-A defect clusters were formed and tailored electronic structures of undoped ZnO, which increased hole mobility by decreasing the scattering effect of ionized defects. Consequently, conductive p-type ZnO-based TCO was achieved without the optical properties degradation.

Comparative studies between donor- (Ga) and acceptor-type (Li) on Al-doped ZnO by co-doping approach were revealed in section V. Crystallographic studies showed the improvement of dopant solubility in (Al,Li) co-doped ZnO sample as % Al increased which were reflected by a small lattice distortion. As a result, the crystallinity and microstructure were improved by minimizing disturbing stress and enhancing diffusibility. Consequently, UV-Visible spectrometer and 4-point probe measurement showed that optoelectronic properties of films improved in 3% Li co-doped samples. In contrast, the deleterious effect on film's microstructure was observed in a 3% Ga co-doped sample due to excess tensile stress which degraded the film's crystallinity as well as optical properties. In addition, the linear fitting plot showed a correlation between bi-axial lattice strain and absorption edge at R^2 of 87.91%.

LIST OF PUBLICATION AND MANUSCRIPT

1. Sureeporn Chothirawat and Yiquan Wu, "Synthesis of p-type co-doped ZnO-based transparent conductive oxide films using electrospray deposition", ***Materials Letters*** (pending)

2. Sureeporn Chothirawat and Yiquan Wu, "Comparative studies of Ga, Li co-doped with Al-doped ZnO transparent conductive film prepared by using electrospray deposition", ***Applied Surface Science***. (pending)

3. Yin Liu, Sureeporn Chothirawat, and Yiquan Wu, "Electrohydrodynamic processing of p-type transparent conducting oxides", ***Journal of Nano Materials*** (submitted).

REFERENCE

1. D. S. Ginley and C. Bright, "Transparent Conducting Oxides," *MRS Bull.,* **25** [08] 15-8 (2000).

2. K. Mahmood and S. B. Park, "Conductivity Enhancement by Fluorine Doping in Boron-Doped Zno Thin Films Deposited by the Electrospraying Method," *J. Cryst. Growth,* **361** 30-7 (2012).

3. D. Raoufi, "Synthesis and Microstructural Properties of Zno Nanoparticles Prepared by Precipitation Method," *Renewable Energy,* **50** 932-7 (2013).

4. Y. Kim, W. Lee, D.-R. Jung, J. Kim, S. Nam, H. Kim, and B. Park, "Optical and Electronic Properties of Post-Annealed Zno:Al Thin Films," *Appl. Phys. Lett,* **96** [17] - (2010).

5. H. Çolak and O. Türkoğlu, "Synthesis, Crystal Structural and Electrical Conductivity Properties of Fe-Doped Zinc Oxide Powders at High Temperatures," *J. Mater. Sci. Technol.,* **28** [3] 268-74 (2012).

6. F. Maldonado and A. Stashans, "Al-Doped Zno: Electronic, Electrical and Structural Properties," *J. Phys. Chem. C,* **71** [5] 784-7 (2010).

7. M. Gabás, A. Landa-Cánovas, J. Luis Costa-Krämer, F. Agulló-Rueda, A. R. González-Elipe, P. Díaz-Carrasco, J. Hernández-Moro, I. Lorite, P. Herrero, P. Castillero, A. Barranco, and J. Ramón Ramos-Barrado, "Differences in N-Type Doping Efficiency between Al- and Ga-Zno Films," *J. Appl. Phys.,* **113** [16] - (2013).

8. V. Kumar, *Zinc Oxide Thin Films for Transparent Conducting Oxide Application;* p. 156. LAP LAMBERT Academic Publishing, 2012.

9. Y. Tetsuya and K.-Y. Hiroshi, "Solution Using a Codoping Method to Unipolarity for the Fabrication of P -Type Zno," *Jpn. J. Appl. Phys.,* **38** [2B] L166 (1999).

10. T. Yamamoto, "Codoping for the Fabrication of P-Type Zno," *Thin Solid Films,* **420–421** [0] 100-6 (2002).

11. K. Shirouzu, T. Ohkusa, M. Hotta, N. Enomoto, and J. Hojo, "Distribution and Solubility Limit of Al in Al2o3-Doped Zno Sintered Body," *J. Ceram. Soc. Jpn.,* **115** [1340] 254-8 (2007).

12. S.-Y. Tsai, M.-H. Hon, and Y.-M. Lu, "Local Electronic Structure of Lithium-Doped Zno Films Investigated by X-Ray Absorption near-Edge Spectroscopy," *J. Phys. Chem. C,* **115** [20] 10252-5 (2011).

13. L. Chen, Z. Xiong, Q. Wan, and D. Li, "Suppression of the Formation of Interstitial Li through (F,Li) Codoping Zno"; p. 012158 in Vol. 276. IOP Publishing,

14. C. Park, S. Zhang, and S.-H. Wei, "Origin of P-Type Doping Difficulty in Zno: The Impurity Perspective," *Phys. Rev. B,* **66** [7] 073202 (2002).

15. T. Yamamoto, "Codoping Method for Solutions of Doping Problems in Wide-Band-Gap Semiconductors," *Phys. Status Solidi A,* **193** [3] 423-33 (2002).

16. S.-Y. Kuo, W.-C. Chen, F.-I. Lai, C.-P. Cheng, H.-C. Kuo, S.-C. Wang, and W.-F. Hsieh, "Effects of Doping Concentration and Annealing Temperature on Properties of Highly-Oriented Al-Doped Zno Films," *J. Cryst. Growth,* **287** [1] 78-84 (2006).

17. S.-C. Chang, "Post-Annealed Gallium and Aluminum Co-Doped Zinc Oxide Films Applied in Organic Photovoltaic Devices," *Nanoscale Res. Lett.,* **9** [1] 562- (2014).

18. Y. Wu and R. L. Clark, "Electrohydrodynamic Atomization: A Versatile Process for Preparing Materials for Biomedical Applications," *J. Biomater. Sci., Polym. Ed.,* **19** [5] 573-601 (2008).

19. J. D. Rancourt, *Optical Thin Films: User Handbook.* SPIE Press, 1996.

20. X. Jiang, F. L. Wong, M. K. Fung, and S. T. Lee, "Aluminum-Doped Zinc Oxide Films as Transparent Conductive Electrode for Organic Light-Emitting Devices," *Appl. Phys. Lett,* **83** [9] 1875-7 (2003).

21. M.-C. Jun, S.-U. Park, and J.-H. Koh, "Comparative Studies of Al-Doped Zno and Ga-Doped Zno Transparent Conducting Oxide Thin Films," *Nanoscale Res. Lett.,* **7** [1] 639- (2012).

22. H. Ohta and H. Hosono, "Transparent Oxide Optoelectronics," *Mater. Today,* **7** [6] 42-51 (2004).

23. M.-J. Lee, J. Lim, J. Bang, W. Lee, and J.-M. Myoung, "Effect of the Thickness and Hydrogen Treatment on the Properties of Ga-Doped Zno Transparent Conductive Films," *Appl. Surf. Sci.,* **255** [5, Part 2] 3195-200 (2008).

24. B. Szyszka, W. Dewald, S. K. Gurram, A. Pflug, C. Schulz, M. Siemers, V. Sittinger, and S. Ulrich, "Recent Developments in the Field of Transparent Conductive Oxide Films for Spectral Selective Coatings, Electronics and Photovoltaics," *Curr. Appl Phys.,* **12** S2-S11 (2012).

25. H. Liu, V. Avrutin, N. Izyumskaya, Ü. Özgür, and H. Morkoç, "Transparent Conducting Oxides for Electrode Applications in Light Emitting and Absorbing Devices," *Superlattices Microstruct.,* **48** [5] 458-84 (2010).

26. Y. Liu, Y. Li, and H. Zeng, Vol. 2013, p. 9. Hindawi Publishing Corporation, 2013.

27. H.-R. An, H.-J. Ahn, and J.-W. Park, "High-Quality, Conductive, and Transparent Ga-Doped Zno Films Grown by Atmospheric-Pressure Chemical-Vapor Deposition," *Ceram. Int.*, **41** [2, Part A] 2253-9 (2015).

28. W.-S. Liu, S.-Y. Wu, C.-Y. Hung, C.-H. Tseng, and Y.-L. Chang, "Improving the Optoelectronic Properties of Gallium Zno Transparent Conductive Thin Films through Titanium Doping," *J. Alloys Compd.*, **616** [0] 268-74 (2014).

29. C. P. Liu and G. R. Jeng, "Properties of Aluminum Doped Zinc Oxide Materials and Sputtering Thin Films," *J. Alloys Compd.*, **468** [1–2] 343-9 (2009).

30. W.-J. Chen, W.-L. Liu, S.-H. Hsieh, and Y.-G. Hsu, "Synthesis of Zno:Al Transparent Conductive Thin Films Using Sol-Gel Method," *Procedia Eng.*, **36** [0] 54-61 (2012).

31. R. Martins, E. Fortunato, P. Barquinha, and L. Pereira, *Transparent Oxide Electronics: From Materials to Devices*. John Wiley & Sons, 2012.

32. R. Ghosh, D. Basak, and S. Fujihara, "Effect of Substrate-Induced Strain on the Structural, Electrical, and Optical Properties of Polycrystalline Zno Thin Films," *J. Appl. Phys.*, **96** [5] 2689-92 (2004).

33. A. J. M. a. J.M.Herbert, *Electroceramics* 2ed.*;* p. 557. John Wiley & Sons Ltd, Chicheter, West Sussex, England 448, 2003.

34. M. L. Addonizio and C. Diletto, "Doping Influence on Intrinsic Stress and Carrier Mobility of Lp-Mocvd-Deposited Zno:B Thin Films," *Sol. Energy Mater. Sol. Cells*, **92** [11] 1488-94 (2008).

35. D.-S. Kim, J.-H. Park, S.-J. Lee, K.-J. Ahn, M.-S. Lee, M.-H. Ham, W. Lee, and J.-M. Myoung, "Effects of Oxygen Concentration on the Properties of Al-Doped Zno Transparent Conductive Films Deposited by Pulsed Dc Magnetron Sputtering," *Mater. Sci. Semicond. Process.*, **16** [3] 997-1001 (2013).

36. K.-J. Ahn, J.-H. Park, B.-K. Shin, W. Lee, G. Y. Yeom, and J.-M. Myoung, "Effect of Sputtering Power on the Properties of Zno:Ga Transparent Conductive Oxide Films Deposited by Pulsed Dc Magnetron Sputtering with a Rotating Cylindrical Target," *Appl. Surf. Sci.*, **271** [0] 216-22 (2013).

37. H. Benzarouk, A. Drici, M. Mekhnache, A. Amara, M. Guerioune, J. C. Bernède, and H. Bendjffal, "Effect of Different Dopant Elements (Al, Mg and Ni) on Microstructural, Optical and Electrochemical Properties of Zno Thin Films Deposited by Spray Pyrolysis (Sp)," *Superlattices Microstruct.*, **52** [3] 594-604 (2012).

38. X.-Y. Li, H.-J. Li, Z.-J. Wang, H. Xia, Z.-Y. Xiong, J.-X. Wang, and B.-C. Yang, "Effect of Substrate Temperature on the Structural and Optical Properties of Zno and Al-Doped Zno Thin Films Prepared by Dc Magnetron Sputtering," *Opt. Commun.,* **282** [2] 247-52 (2009).

39. S. W. Shin, I. Y. Kim, K. S. Jeon, J. Y. Heo, G.-S. Heo, P. Patil, J. H. Kim, and J. Y. Lee, "Wide Band Gap Characteristic of Quaternary and Flexible Mg and Ga Co-Doped Zno Transparent Conductive Thin Films," *J. Asian Ceram. Soc.,* **1** [3] 262-6 (2013).

40. C. Faure, J. Clatot, L. Teulé-Gay, G. Campet, C. Labrugère, M. Nistor, and A. Rougier, "Co-Sputtered Zno:Si Thin Films as Transparent Conductive Oxides," *Thin Solid Films,* **524** [0] 151-6 (2012).

41. M. Malek, M. Mamat, M. Musa, Z. Khusaimi, M. Sahdan, A. Suriani, A. Ishak, I. Saurdi, S. Rahman, and M. Rusop, "Thermal Annealing-Induced Formation of Zno Nanoparticles: Minimum Strain and Stress Ameliorate Preferred *C*-Axis Orientation and Crystal-Growth Properties," *J. Alloys Compd.,* **610** 575-88 (2014).

42. C. Gorla, N. Emanetoglu, S. Liang, W. Mayo, Y. Lu, M. Wraback, and H. Shen, "Structural, Optical, and Surface Acoustic Wave Properties of Epitaxial Zno Films Grown on (0112) Sapphire by Metalorganic Chemical Vapor Deposition," *J. Appl. Phys.,* **85** [5] 2595-602 (1999).

43. D. P. Norton, Y. W. Heo, M. P. Ivill, K. Ip, S. J. Pearton, M. F. Chisholm, and T. Steiner, "Zno: Growth, Doping & Processing," *Mater. Today*, **7** [6] 34-40 (2004).

44. M. A. Martínez, J. Herrero, and M. T. Gutiérrez, "Deposition of Transparent and Conductive Al-Doped Zno Thin Films for Photovoltaic Solar Cells," *Sol. Energy Mater. Sol. Cells,* **45** [1] 75-86 (1997).

45. H. Morkoç and Ü. Özgür, *Zinc Oxide: Fundamentals, Materials and Device Technology*. John Wiley & Sons, 2008.

46. L. Schmidt-Mende and J. L. MacManus-Driscoll, "Zno – Nanostructures, Defects, and Devices," *Mater. Today,* **10** [5] 40-8 (2007).

47. C. Jagadish and S. J. Pearton, *Zinc Oxide Bulk, Thin Films and Nanostructures: Processing, Properties, and Applications*. Elsevier, 2011.

48. E. Fortunato, D. Ginley, H. Hosono, and D. C. Paine, "Transparent Conducting Oxides for Photovoltaics," *MRS Bull.,* **32** [03] 242-7 (2007).

49. H. Kim, C. M. Gilmore, J. S. Horwitz, A. Piqué, H. Murata, G. P. Kushto, R. Schlaf, Z. H. Kafafi, and D. B. Chrisey, "Transparent Conducting Aluminum-Doped Zinc Oxide Thin Films for Organic Light-Emitting Devices," *Appl. Phys. Lett,* **76** [3] 259-61 (2000).

50. J. F. Justo, A. Antonelli, T. M. Schmidt, and A. Fazzio, "Effects of Extended Defects on the Properties of Intrinsic and Extrinsic Point Defects in Silicon," *Physica B,* **273–274** [0] 473-5 (1999).

51. A. Janotti and C. G. Van de Walle, "New Insights into the Role of Native Point Defects in Zno," *J. Cryst. Growth,* **287** [1] 58-65 (2006).

52. S. Zhang, S. H. Wei, and A. Zunger, "Intrinsic *N*-Type Versus *P*-Type Doping Asymmetry and the Defect Physics of Zno," *Phys. Rev. B,* **63** [7] 075205 (2001).

53. J. J. W. Morris, "A Survey of Materials Science I.Structure" (2007) Accessed on: Available at <http://www.mse.berkeley.edu/groups/morris/MSE200/I-structure.pdf>

54. A. A. Sokol, S. A. French, S. T. Bromley, C. R. A. Catlow, H. J. J. van Dam, and P. Sherwood, "Point Defects in Zno," *Faraday Discuss.,* **134** [0] 267-82 (2007).

55. F. X. Xiu, Z. Yang, L. J. Mandalapu, J. L. Liu, and W. P. Beyermann, "P-Type Zno Films with Solid-Source Phosphorus Doping by Molecular-Beam Epitaxy," *Appl. Phys. Lett,* **88** [5] 052106-1-3 (2006).

56. F. Oba, S. R. Nishitani, S. Isotani, H. Adachi, and I. Tanaka, "Energetics of Native Defects in Zno," *J. Appl. Phys.,* **90** [2] 824-8 (2001).

57. R. J. Tilley, *Defects in Solids,* Vol. 4. John Wiley & Sons, 2008.

58. F. Gu, D. You, Z. Wang, D. Han, and G. Guo, "Improvement of Gas-Sensing Property by Defect Engineering in Microwave-Assisted Synthesized 3d Zno Nanostructures," *Sens. Actuators, B,* **204** [0] 342-50 (2014).

59. A. Kohan, G. Ceder, D. Morgan, and C. Van de Walle, "First-Principles Study of Native Point Defects in Zno," *Phys. Rev. B,* **61** [22] 15019-27 (2000).

60. C. H. Chen, E. M. Kelder, and J. Schoonman, "Electrostatic Sol-Spray Deposition (Essd) and Characterisation of Nanostructured Tio2 Thin Films," *Thin Solid Films,* **342** [1–2] 35-41 (1999).

61. X. Tian, Z. Pan, H. Zhang, H. Fan, X. Zeng, C. Xiao, G. Hu, and Z. Wei, "Growth and Characterization of the Al-Doped and Al–Sn Co-Doped Zno Nanostructures," *Ceram. Int.,* **39** [6] 6497-502 (2013).

62. K. Ellmer, "Resistivity of Polycrystalline Zinc Oxide Films: Current Status and Physical Limit," *J. Phys. D: Appl. Phys.,* **34** [21] 3097 (2001).

63. V. Dusastre, *Materials for Sustainable Energy: A Collection of Peer-Reviewed Research and Review Articles from Nature Publishing Group*. World Scientific, 2010.

64. E. Fortunato, L. Raniero, L. Silva, A. Gonçalves, A. Pimentel, P. Barquinha, H. Aguas, L. Pereira, G. Gonçalves, and I. Ferreira, "Highly Stable Transparent and Conducting Gallium-Doped Zinc Oxide Thin Films for Photovoltaic Applications," *Sol. Energy Mater. Sol. Cells,* **92** [12] 1605-10 (2008).

65. C.-Y. Tsay, C.-W. Wu, C.-M. Lei, F.-S. Chen, and C.-K. Lin, "Microstructural and Optical Properties of Ga-Doped Zno Semiconductor Thin Films Prepared by Sol–Gel Process," *Thin Solid Films,* **519** [5] 1516-20 (2010).

66. A. Sáaedi, R. Yousefi, F. Jamali-Sheini, M. Cheraghizade, A. Khorsand Zak, and N. M. Huang, "Optical and Electrical Properties of P-Type Li-Doped Zno Nanowires," *Superlattices Microstruct.,* **61** [0] 91-6 (2013).

67. X. Zi-qiang, D. Hong, L. Yan, and C. Hang, "Al-Doping Effects on Structure, Electrical and Optical Properties of C-Axis-Orientated Zno:Al Thin Films," *Mater. Sci. Semicond. Process.,* **9** [1–3] 132-5 (2006).

68. T. Yamamoto, "Codoping for the Fabrication of P-Type Zno," *Thin Solid Films,* **420-421** 100-6 (2002).

69. J. Mass, P. Bhattacharya, and R. S. Katiyar, "Effect of High Substrate Temperature on Al-Doped Zno Thin Films Grown by Pulsed Laser Deposition," *Mater. Sci. Eng., B,* **103** [1] 9-15 (2003).

70. D. Steiauf, J. L. Lyons, A. Janotti, and C. G. Van de Walle, "First-Principles Study of Vacancy-Assisted Impurity Diffusion in Zno," *APL Mater.,* **2** [9] 096101 (2014).

71. J. T-Thienprasert, S. Rujirawat, W. Klysubun, J. Duenow, T. Coutts, S. Zhang, D. Look, and S. Limpijumnong, "Compensation in Al-Doped Zno by Al-Related Acceptor Complexes: Synchrotron X-Ray Absorption Spectroscopy and Theory," *Phys. Rev. Lett.,* **110** [5] 055502-1-5 (2013).

72. S. Cornelius, M. Vinnichenko, N. Shevchenko, A. Rogozin, A. Kolitsch, and W. Möller, "Achieving High Free Electron Mobility in Zno:Al Thin Films Grown by Reactive Pulsed Magnetron Sputtering," *Appl. Phys. Lett,* **94** [4] - (2009).

73. J. Liu, W. Zhang, D. Song, Q. Ma, L. Zhang, H. Zhang, L. Zhang, and R. Wu, "Investigation of Aluminum–Gallium Co-Doped Zinc Oxide Targets for Sputtering Thin Film and Photovoltaic Application," *J. Alloys Compd.,* **575** 174-82 (2013).

74. V. Assuncao, E. Fortunato, A. Marques, H. Aguas, I. Ferreira, M. Costa, and R. Martins, "Influence of the Deposition Pressure on the Properties of Transparent and Conductive Zno: Ga Thin-Film Produced by Rf Sputtering at Room Temperature," *Thin Solid Films,* **427** [1] 401-5 (2003).

75. J. C. Fan, K. Sreekanth, Z. Xie, S. Chang, and K. V. Rao, "P-Type Zno Materials: Theory, Growth, Properties and Devices," *Prog. Mater Sci.*, **58** [6] 874-985 (2013).

76. Q.-B. Ma, Z.-Z. Ye, H.-P. He, S.-H. Hu, J.-R. Wang, L.-P. Zhu, Y.-Z. Zhang, and B.-H. Zhao, "Structural, Electrical, and Optical Properties of Transparent Conductive Zno:Ga Films Prepared by Dc Reactive Magnetron Sputtering," *J. Cryst. Growth,* **304** [1] 64-8 (2007).

77. J. Zhu and S.-H. Wei, "Tuning Doping Site and Type by Strain: Enhanced -Type Doping in Li Doped Zno," *Solid State Commun.,* **151** [20] 1437-9 (2011).

78. C. Rauch, W. Gehlhoff, M. R. Wagner, E. Malguth, G. Callsen, R. Kirste, B. Salameh, A. Hoffmann, S. Polarz, Y. Aksu, and M. Driess, "Lithium Related Deep and Shallow Acceptors in Li-Doped Zno Nanocrystals," *J. Appl. Phys.,* **107** [2] - (2010).

79. Y. Yanfa, M. M. Al-Jassim, and W. Su-Huai, "Doping of Zno by Group-Ib Elements," *Appl. Phys. Lett,* **89** [18] 181912 (2006).

80. M. Wardle, J. Goss, and P. Briddon, "Theory of Li in Zno: A Limitation for Li-Based *P*-Type Doping," *Phys. Rev. B,* **71** [15] 155205 (2005).

81. Y.-J. Lin, M.-S. Wang, C.-J. Liu, and H.-J. Huang, "Defects, Stress and Abnormal Shift of the (002) Diffraction Peak for Li-Doped Zno Films," *Appl. Surf. Sci.,* **256** [24] 7623-7 (2010).

82. J. Lu, Y. Zhang, Z. Ye, Y. Zeng, H. He, L. Zhu, J. Huang, L. Wang, J. Yuan, and B. Zhao, "Control of P-and N-Type Conductivities in Li-Doped Zno Thin Films," *Appl. Phys. Lett,* **89** [11] 112113-1-3 (2006).

83. M. Zaharescu, S. Mihaiu, A. Toader, I. Atkinson, J. Calderon-Moreno, M. Anastasescu, M. Nicolescu, M. Duta, M. Gartner, K. Vojisavljevic, B. Malic, V. A. Ivanov, and E. P. Zaretskaya, "Zno Based Transparent Conductive Oxide Films with Controlled Type of Conduction," *Thin Solid Films*, **571, Part 3** [0] 727-34 (2014).

84. M. Joseph, H. Tabata, H. Saeki, K. Ueda, and T. Kawai, "Fabrication of the Low-Resistive P-Type Zno by Codoping Method," *Physica B,* **302–303** [0] 140-8 (2001).

85. D. S. Ginley and C. Bright, "Transparent Conducting Oxides," *MRS Bulletin,* **25** [08] 15-8 (2000).

86. R. L. Grimm, "Fundamental Studies of the Mechanisms and Applications of Field-Induced Droplet Ionization Mass Spectrometry and Electrospray Mass Spectrometry"; California Institute of Technology, 2005.

87. I. Uematsu, H. Matsumoto, K. Morota, M. Minagawa, A. Tanioka, Y. Yamagata, and K. Inoue, "Surface Morphology and Biological Activity of Protein Thin Films Produced by Electrospray Deposition," *J. Colloid Interface Sci.,* **269** [2] 336-40 (2004).

88. A. Jaworek and A. T. Sobczyk, "Electrospraying Route to Nanotechnology: An Overview," *J. Electrostat.,* **66** [3–4] 197-219 (2008).

89. J. Du, Y. Wu, K.-L. Choy, and P. H. Shipway, "Structure Evolution and Stoichiometry Control of Pb(Zr, Ti)O_3 Thick Films Fabricated by Electrospray Assisted Vapour Deposition," *Appl. Surf. Sci.,* **256** [14] 4606-11 (2010).

90. T. Kien Nguyen, V. D. Nguyen, B. Seong, N. Hoang, J. Park, and D. Byun, "Control and Improvement of Jet Stability by Monitoring Liquid Meniscus in Electrospray and Electrohydrodynamic Jet," *J. Aerosol Sci.,* **71** [0] 29-39 (2014).

91. K. Altmann, R. D. Schulze, and J. Friedrich, "Polymer Deposition Morphology by Electrospray Deposition - Modifications through Distance Variation," *Thin Solid Films,* **564** [0] 269-76 (2014).

92. A. Lintanf, E. Djurado, and P. Vernoux, "Pt/Ysz Electrochemical Catalysts Prepared by Electrostatic Spray Deposition for Selective Catalytic Reduction of No by C_3h_6," *Solid State Ionics,* **178** [39–40] 1998-2008 (2008).

93. O. Wilhelm, S. E. Pratsinis, D. Perednis, and L. J. Gauckler, "Electrospray and Pressurized Spray Deposition of Yttria-Stabilized Zirconia Films," *Thin Solid Films,* **479** [1–2] 121-9 (2005).

94. J. Du and K.-L. Choy, "Electrostatic Spray Assisted Vapour Deposition of Tio_2-Based Films," *Solid State Ionics,* **173** [1–4] 119-24 (2004).

95. A. Rezvanpour and C.-H. Wang, "Computational and Experimental Studies of Electrospray Deposition Process in Pharmaceutical Micro-Pattern Formation," *Chem. Eng. Sci.,* **66** [17] 3836-49 (2011).

96. J. Du, Y. Wu, and K.-L. Choy, "Controlled Synthesis of Gas Sensing $Cr_{2-x}ti_xo_3$ Films by Electrostatic Spray Assisted Vapour Deposition and Their Structural Characterisation," *Thin Solid Films,* **497** [1–2] 42-7 (2006).

97. S. Ali, J. Bae, K. H. Choi, C. H. Lee, Y. H. Doh, S. Shin, and N. P. Kobayashi, "Organic Non-Volatile Memory Cell Based on Resistive Elements through Electro-Hydrodynamic Technique," *Org. Electron.,* **17** [0] 121-8 (2015).

98. C. Ghanshyam, S. Bagchi, and P. Kapur, "Optimization of Spray Parameters in the Fabrication of Sno_2 Layers Using Electrostatic Assisted Deposition Technique," *J. Electrostat.,* **71** [1] 68-76 (2013).

99. M. Ali, M. Abbas, S. K. Shah, R. Tuerhong, A. Generosi, B. Paci, L. Hirsch, and R. Gunnella, "Realization of Solution Processed Multi-Layer Bulk Heterojunction Organic Solar Cells by Electro-Spray Deposition," *Org. Electron.,* **13** [10] 2130-7 (2012).

100. I. Endo, T. Nagamune, and H. Akita, *Nano/Micro Biotechnology*. Springer, 124-125, 2010.

101. T. Fukuda, A. Suzuki, Y. Liao, and K. Suzuki, "Influence of Spray Conditions on Droplet Charge Per Unit Volume for Electrospray Deposition," *J. Aerosol Sci.,* **77** 38-49 (2014).

102. Y. Kim, J. Lee, H. Kang, G. Kim, N. Kim, and K. Lee, "Controlled Electro-Spray Deposition of Highly Conductive Pedot:Pss Films," *Sol. Energy Mater. Sol. Cells,* **98** [0] 39-45 (2012).

103. K. Morota, H. Matsumoto, T. Mizukoshi, Y. Konosu, M. Minagawa, A. Tanioka, Y. Yamagata, and K. Inoue, "Poly(Ethylene Oxide) Thin Films Produced by Electrospray Deposition: Morphology Control and Additive Effects of Alcohols on Nanostructure," *J. Colloid Interface Sci.,* **279** [2] 484-92 (2004).

104. R. D. Smith, J. H. Wahl, D. R. Goodlett, and S. A. Hofstadler, "Capillary Electrophoresis/Mass Spectrometry," *Anal. Chem.,* **65** [13] 574A-84A (1993).

105. B. A. Thomson, "Atmospheric Pressure Ionization and Liquid Chromatography/Mass Spectrometry—Together at Last," *J. Am. Soc. Mass. Spectrom.,* **9** [3] 187-93 (1998).

106. Y. Hirabayashi, A. Hirabayashi, Y. Takada, M. Sakairi, and H. Koizumi, "A Sonic Spray Interface for the Mass Analysis of Highly Charged Ions from Protein Solutions at High Flow Rates," *Anal. Chem.,* **70** [9] 1882-4 (1998).

107. S. C. G. Leeuwenburgh, J. G. C. Wolke, J. Schoonman, and J. A. Jansen, "Influence of Deposition Parameters on Morphological Properties of Biomedical Calcium Phosphate Coatings Prepared Using Electrostatic Spray Deposition," *Thin Solid Films,* **472** [1–2] 105-13 (2005).

108. S. Zargham, S. Bazgir, A. Tavakoli, A. S. Rashidi, and R. Damerchely, "The Effect of Flow Rate on Morphology and Deposition Area of Electrospun Nylon 6 Nanofiber," *J. Eng. Fibers Fabr.,* **7** 42-9 (2012).

109. A. Princivalle, D. Perednis, R. Neagu, and E. Djurado, "Microstructural Investigations of Nanostructured La(Sr)$Mno_{3-\Delta}$ Films Deposited by Electrostatic Spray Deposition," *Chem. Mater.,* **16** [19] 3733-9 (2004).

110. C. H. Chen, E. M. Kelder, M. J. G. Jak, and J. Schoonman, "Electrostatic Spray Deposition of Thin Layers of Cathode Materials for Lithium Battery," *Solid State Ionics,* **86–88, Part 2** [0] 1301-6 (1996).

111. O. Wilhelm, L. Mädler, and S. E. Pratsinis, "Electrospray Evaporation and Deposition," *J. Aerosol Sci.*, **34** [7] 815-36 (2003).

112. A. M. Gañán-Calvo, J. Dávila, and A. Barrero, "Current and Droplet Size in the Electrospraying of Liquids. Scaling Laws," *J. Aerosol Sci.*, **28** [2] 249-75 (1997).

113. A. L. Yarin, S. Koombhongse, and D. H. Reneker, "Taylor Cone and Jetting from Liquid Droplets in Electrospinning of Nanofibers," *J. Appl. Phys.*, **90** [9] 4836-46 (2001).

114. A. Jaworek, "Micro- and Nanoparticle Production by Electrospraying," *Powder Technol.*, **176** [1] 18-35 (2007).

115. C. Chen, E. M. Kelder, and J. Schoonman, "Functional Ceramic Films with Reticular Structures Prepared by Electrostatic Spray Deposition Technique," *J. Electrochem. Soc.*, **144** [11] L289-L91 (1997).

116. T. Nguyen and E. Djurado, "Deposition and Characterization of Nanocrystalline Tetragonal Zirconia Films Using Electrostatic Spray Deposition," *Solid State Ionics*, **138** [3–4] 191-7 (2001).

117. B. E. Sernelius, K.-F. Berggren, Z.-C. Jin, I. Hamberg, and C. Granqvist, "Band-Gap Tailoring of Zno by Means of Heavy Al Doping," *Phys. Rev. B*, **37** [17] 10244 (1988).

118. Y.-E. Jeong and S. Park, "Thermal Stress Induced Band Gap Variation of Zno Thin Films," *Curr. Appl Phys.*, **14** [1] 30-3 (2014).

119. V. Srikant and D. Clarke, "Optical Absorption Edge of Zno Thin Films: The Effect of Substrate," *J. Appl. Phys.*, **81** [9] 6357-64 (1997).

120. J. Xu, S. Shi, X. Zhang, Y. Wang, M. Zhu, and L. Li, "Structural and Optical Properties of (Al, K)-Co-Doped Zno Thin Films Deposited by a Sol–Gel Technique," *Mater. Sci. Semicond. Process.*, **16** [3] 732-7 (2013).

121. R. A. Zoppi, I. V. P. Yoshida, and S. P. Nunes, "Hybrids of Perfluorosulfonic Acid Ionomer and Silicon Oxide by Sol-Gel Reaction from Solution: Morphology and Thermal Analysis," *Polymer*, **39** [6–7] 1309-15 (1998).

122. A. Rahman, R. Jayaganthan, R. Jain, A. Chawla, R. Chandra, and R. Ambardar, "Study of Nanostructured Al Doped Zno Films," *Surf. Eng.*, **29** [6] 440-6 (2013).

123. R. Green, "Hall Effect Measurements in Materials Characterization" (2011) Keithley Instruments, Inc. Accessed on: Available at <www.keithley.com/data?asset=55773>

124. B. He, J. Xu, H. Xing, C. Wang, and X. Zhang, "The Effect of Substrate Temperature on High Quality *C*-Axis Oriented Azo Thin Films Prepared by Dc Reactive Magnetron

Sputtering for Photoelectric Device Applications," *Superlattices Microstruct.*, **64** 319-30 (2013).

125. M. Inc., Minitab 16.1.0, [Computer Program], State College PA US, 2010.

126. H.-S. Chin and L.-S. Chao, "The Effect of Thermal Annealing Processes on Structural and Photoluminescence of Zinc Oxide Thin Film," *J Nanomater*, **2013** 8 (2013).

127. V. Ghafouri, A. Ebrahimzad, and M. Shariati, "The Effect of Annealing Time and Temperature on Morphology and Optical Properties of Zno Nanostructures Grown by a Self-Assembly Method," *Scientia Iranica*, **20** [3] 1039-48 (2013).

128. W. Lee, S. Shin, D.-R. Jung, J. Kim, C. Nahm, T. Moon, and B. Park, "Investigation of Electronic and Optical Properties in Al−Ga Codoped Zno Thin Films," *Curr. Appl Phys.*, **12** [3] 628-31 (2012).

129. T. M. G. o. Companies, "Diethylene Glycal Product Guide" (2005) Accessed on: Available at <http://www.meglobal.biz/media/product_guides/MEGlobal_DEG.pdf>

130. T. Yamamoto and H. Katayama-Yoshida, "Physics and Control of Valence States in Zno by Codoping Method," *Physica B*, **302–303** [0] 155-62 (2001).

131. P. S. V. Kailas, "Chapter 5. Diffusion" Accessed on: Available at <http://nptel.iitk.ac.in/courses/Webcourse-contents/IISc-BANG/Material%20Science/pdf/Module5.pdf>

132. J. Lu, Z. Ye, Y. Zeng, L. Zhu, L. Wang, J. Yuan, B. Zhao, and Q. Liang, "Structural, Optical, and Electrical Properties of (Zn,Al)O Films over a Wide Range of Compositions," *J. Appl. Phys*, **100** [7] 073714-1-11 (2006).

133. T. Norby, "Kjm5120 and Kjm9120 Defects and Reactions" Accessed on: Available at <http://www.uio.no/studier/emner/matnat/kjemi/KJM5120/v09/undervisningsmateriale/KJM5120-9120%20Defects%20and%20Reactions-Intro-Ch1.pdf>

134. C. Kittel, P. McEuen, and P. McEuen, *Introduction to Solid State Physics*, Vol. 8. Wiley New York, 1976.

135. P. Chand, A. Gaur, A. Kumar, and U. K. Gaur, "Structural, Morphological and Optical Study of Li Doped Zno Thin Films on Si (100) Substrate Deposited by Pulsed Laser Deposition," *Ceram. Int.*, **40** [8, Part A] 11915-23 (2014).

136. K. Takemura, "Evaluation of the Hydrostaticity of a Helium-Pressure Medium with Powder X-Ray Diffraction Techniques," *J. Appl. Phys.*, **89** [1] 662-8 (2001).

137. L. Chen, Z. Xiong, Q. Wan, and D. Li, "Suppression of the Formation of Interstitial Li through (F, Li) Codoping Zno"; p. 012158 in Vol. 276. IOP Publishing,